



HAL
open science

Strain and defects in irradiated materials: a study using X-ray diffraction and diffuse scattering

Jayanth Channagiri

► **To cite this version:**

Jayanth Channagiri. Strain and defects in irradiated materials: a study using X-ray diffraction and diffuse scattering. Materials. Université de Limoges, 2015. English. NNT: 2015LIMO0093 . tel-01267054

HAL Id: tel-01267054

<https://theses.hal.science/tel-01267054>

Submitted on 3 Feb 2016

HAL is a multi-disciplinary open access archive for the deposit and dissemination of scientific research documents, whether they are published or not. The documents may come from teaching and research institutions in France or abroad, or from public or private research centers.

L'archive ouverte pluridisciplinaire **HAL**, est destinée au dépôt et à la diffusion de documents scientifiques de niveau recherche, publiés ou non, émanant des établissements d'enseignement et de recherche français ou étrangers, des laboratoires publics ou privés.

Université de Limoges

**École Doctorale Sciences et Ingénierie en Matériaux, Mécanique,
Énergétique et Aéronautique (ED 522)**

Science des Procédés Céramiques et de Traitements de Surface (SPCTS)

Thèse pour obtenir le grade de
Docteur de l'Université de Limoges
Discipline : Sciences des Matériaux Céramiques

Présentée et soutenue par
Jayanth Channagiri

Le 4 décembre 2015

**Strain and defects in irradiated materials – A study using X-ray
diffraction and diffuse scattering**

Thèse dirigée par Alexandre BOULLE et Aurélien DEBELLE

JURY :

Président du jury

M. Lionel Thomé, Directeur de Recherche, CNRS, CSNSM Orsay

Rapporteurs

M. François Rieutord, Directeur de Recherche, CEA INAC, Grenoble

Mme. Isabelle Monnet, Directeur de Recherche, CEA, CIMAP Caen

Examineurs

M. Alain Declémy, Chargé de Recherche, CNRS, Institut Pprime, Poitiers

M. Andrés Redondo Cubero, Assistant Lecturer, Universidad Autónoma de Madrid

M. Aurélien Debelle, Maître de Conférences, CSNSM Orsay

M. Alexandre Boule, Directeur De Recherche, CNRS, SPCTS Limoges





To my beloved family...



There should be no boundaries to human endeavor. We are all different. However bad life may seem, there is always something you can do, and succeed at. While there's life, there is hope.

Stephen Hawking



Droits d'auteurs

Cette création est mise à disposition selon le Contrat :

« **Attribution-Pas d'Utilisation Commerciale-Pas de modification 3.0 France** »

disponible en ligne : <http://creativecommons.org/licenses/by-nc-nd/3.0/fr/>



Acknowledgements

This thesis was performed in the laboratory Science des Procédés Céramiques et de Traitements de Surface (SPCTS UMR CNRS 7315), Limoges. Firstly, I would like to thank the director of the laboratory, Dr. Thierry Chartier and the director of the Group 3, Dr. Phillippe Thomas for having me in the lab. This project would have been impossible without the financial support by the region Limousin, so I would like to sincerely thank them.

I would like to express my deepest gratitude to my supervisors Dr. Alexandre Boule, Directeur de Recherche CNRS, SPCTS, Limoges and Dr. Aurélien Debelle, Maître de Conférences (HDR), Université Paris-Sud for giving me an opportunity to work on this very interesting subject for 3 years. My special thanks to Dr. Alexandre Boule for his patient guidance during all the three years and for being available any-time when needed advice. His constant support and enthusiastic encouragement helped me complete this PhD. He was not just an advisor, but was a friend, who was there to share ideas and humour. I learned not only about X-ray diffraction and programming but also about discipline and punctuality. In short, he showed me how an ideal PhD advisor should be!

I would like to offer my special thanks to Dr. Aurélien Debelle with whom I spent some time during various experiments in different laboratories and who was always supporting, even from far and who was there to help out any time. I feel extremely lucky to have both of them as my PhD supervisors.

I acknowledge the contribution of Dr. Lionel Thome, Directeur de Recherche, CNRS, CSNSM Orsay for helping me perform RBS/C experiments in Orsay. I am also indebted to Dr. Arnaud Alzina, Maître de Conférences - Université de Limoges and Dr. Philippe Michaud, Maître de Conférences - Université de Limoges for their valuable and constructive scientific discussions and support related to Finite Element Modelling.

I would like to thank Mr. Andreas Kloeckner and the whole community of PyCUDA, for building the open-source wrapper for CUDA and for the constant support. I would also like to thank the communities of Python, SciPy, NumPy, Matplotlib and Geany for their striving efforts to build very useful freely available programming tools. This thesis is wholly written using \LaTeX and I would like to thank

the \LaTeX community as well.

My sincere gratitude to all my colleagues from the laboratory, who made my Limoges chapter unforgettable and they were there like a family in a home away from home. I would like to thank especially my officemates Florian Rejasse, Aenor Pons, Jeremy David, Quitterie Monegier du Sorbier and David Siniscalco for the company and the working ambiance during my PhD. I also would like to thank Alberto Cambra, Joanna Krowka, Laura Molina, Pawel Sokolowski, Jess Gambe, Rolando Cadidato Jr., Lydia Muñoz, Claire Bonhomme, Deborah Dompoin, Andrzej Warchał, Karolina Kazak, Olivier Noguera, Abhijeet Dasgupta, Karthik Nakkala, Fabien Bouzat, Vanessa Orozco and Virginie Thery for their incredible love and friendship. I would also like to extend my thanks to Virginie Reytier and Pamela Bathias for always helping me by taking care of all my paper work.

Last but not the least, I am indebted for all the unconditional and emotional support by my beloved family. I would also like to thank Carolin Rost and Stephane Rocher who were like my family in France and for all the good times I spent with them.



Contents

INTRODUCTION	15
1 LITERATURE SURVEY	17
1.1 Introduction	17
1.2 Interaction of ion beams with materials	18
1.3 Defect creation via elastic nuclear interaction	20
1.4 The material - Zirconia	21
1.5 Why Cubic Zirconia?	21
1.6 Literature survey on YSZ under ion irradiation	23
1.7 Introduction to the theory of X-ray Diffraction	27
1.8 Production of X-rays	28
1.9 Kinematical Theory of Diffraction	29
1.10 Effects of microstructure	34
1.11 Diffuse Scattering of X-rays by crystal defects	35
1.12 Dynamical Theory of Diffraction	39
1.12.1 Historical background	39
1.12.2 Takagi-Taupin equations	40
1.12.3 Recursion formulae for the Takagi - Taupin equations	42
1.13 Conclusion	43
References	44
2 EXPERIMENTAL AND COMPUTATIONAL TECHNIQUES	51
2.1 Experimental Techniques	51
2.1.1 Ion beam accelerator	51
2.1.2 Rutherford backscattering spectrometry	52
2.1.3 X-ray Diffraction	57
2.2 Computational Techniques	60
2.2.1 Introduction	60
2.2.2 Evolution of computing	61

2.2.3	GPUs as Parallel Computers	65
2.2.4	CUDA programming	66
2.2.5	Flynn's taxonomy	68
2.2.6	Parallel computing speedup	69
2.2.7	Work station and GPU specifications	71
2.2.8	Python programming language	72
2.2.9	Implementation : Multiprocessing	73
2.2.10	Implementation : GPU Computing	76
2.3	Conclusion	77
	References	78
3	STRAIN AND DAMAGE BUILD-UP IN AU-IRRADIATED ZIRCONIA	83
3.1	Introduction	83
3.2	Simulation procedure	83
3.3	Cubic B-splines	86
3.4	Generalized simulated annealing	88
3.5	Results	91
3.5.1	X-ray diffraction	91
3.5.2	RBS/C	101
3.6	Discussion	105
3.6.1	RBS/C Kinetics	105
3.6.2	Debye-Waller Kinetics	107
3.6.3	Strain Kinetics	108
3.6.4	Damage evolution	109
3.7	Conclusion	110
	References	113
4	MODELLING OF DIFFUSE X-RAY SCATTERING	118
4.1	Introduction	118
4.2	Theoretical background	119
4.3	Simulation procedure	120
4.3.1	The displacement field	121
4.3.2	The scattered intensity	125
4.4	Applications to irradiated single crystals	127
4.4.1	Randomly distributed spherical defects	127
4.4.2	Inhomogeneous defect distribution : Varying defect size	129
4.4.3	Inhomogeneous defect distribution : Varying misfit	131
4.4.4	Inhomogeneous defect distribution : Varying defect concentration	131



4.4.5	Simulation of RSMs of YSZ	134
4.4.6	Spatially correlated defects	136
4.5	Conclusion	139
	References	141
	APPENDIX	143
	GENERAL CONCLUSION	156



Listing of figures

1.1.1	Schematic representation of the variation of electronic energy loss and nuclear energy loss with ion velocity	19
1.4.1	Crystalline structure of cubic Zirconia (ZrO_2)	21
1.6.1	Damage accumulation in FSZ samples irradiated with Xe^{++} ions at 170 K.	23
1.6.2	Bright-field TEM micrograph of a cross-section of YSZ irradiated with 400 keV Cs ions at a fluence of $1 \times 10^{17} cm^{-2}$ in room temperature	24
1.6.3	Damage kinetics of YSZ irradiated at room temperature with various noble-gas ions .	25
1.6.4	Accumulated damage f_D versus fluence in YSZ crystals irradiated with 4 MeV Au^{2+} (squares) and 940 MeV Pb^{53+} (circles) ions. The solid line represents the fit made by using the MSDA model.	27
1.8.1	The brilliance of X-ray sources as a function of time	29
1.9.1	(a) Representation of scattering by one electron where the incident and the diffracted wave vectors and the associated scattering vector are shown. (b) The case of scattering by two electrons where the path difference is given by δ	30
1.9.2	Reciprocal lattice representation which satisfies the Bragg's law for a set of planes hkl	32
1.9.3	Geometrical representation of the Ewald construction	34
1.11.1	Reciprocal space distribution calculated for spherical defects of various strengths . .	39
2.1.1	Schematic representation of the JANNuS facility at Orsay	52
2.1.2	Energy loss by elastic and inelastic collisions of 4 MeV Au ions in YSZ determined using SRIM calculations.	53
2.1.3	Rutherford backscattering geometry	54
2.1.4	The graph of energy $E_1(x)$ plotted against the depth x to show that the energy $E_1(x)$ can be linearly related to the depth x	55
2.1.5	The path of a channelling particle inside a diamond-like crystal lattice	56
2.1.6	Conventional channelling spectrum observed for a random orientation, perfect crystal and the crystal containing defects	57
2.1.7	Different rotations of a four-circle goniometer	58
2.1.8	Four-circle PANalytical diffractometer	59

2.1.9	The schematic representation showing different scans, and the Ewald construction	60
2.1.10	Reciprocal space map recorded in the vicinity of the (004) reflection of Cs-implanted YSZ crystal	61
2.2.1	Feature size of transistors over the past few decades	62
2.2.2	The clock frequency of different processors in the past 25 years	62
2.2.3	The computing speed of different processors over the past few decades	63
2.2.4	The design philosophy of a CPU and a GPU	64
2.2.5	The evolution of the peak performance in terms of GFlops for CPUs and GPUs over time	64
2.2.6	The number of publications on the title "GPU" OR "Graphical Processing Unit" OR "Graphic Processing Unit" obtained from the WebOfScience	65
2.2.7	Visualization of Flynn's taxonomy	67
2.2.8	Speedup behaviour using Amdahl's law and Gustafson's law	70
2.2.9	NVIDIA Quadro K4000 GPU	71
2.2.10	(a) Multiprocessing Speedup plotted for different number of processors <i>vs</i> total array size (b) Speedup obtained by GPU with respect to a single core processor	76
3.2.1	Illustration of the Gerchberg - Saxton algorithm.	84
3.3.1	Illustration of strain profile calculated with six nonzero basis functions	87
3.4.1	Illustration of the problem of finding the global minima.	89
3.5.1	$\theta - 2\theta$ scans recorded in the vicinity of the (400) reflection for virgin and YSZ crystals irradiated at room temperature.	92
3.5.2	$\theta - 2\theta$ scans and corresponding simulated curves recorded in the vicinity of the (400) reflection for virgin and YSZ crystals irradiated at room temperature.	93
3.5.3	Strain (a) and the Debye-Waller profiles (b) obtained after the simulation of the XRD curves for 300 K.	94
3.5.4	Variation of the maximum strain and damage levels as a function of the ion fluence irradiated at 300 K.	95
3.5.5	$\theta - 2\theta$ scans and the corresponding simulated curves recorded in the vicinity of (400) reflection for virgin and YSZ crystals irradiated at 80 K.	96
3.5.6	Strain (a) and Debye-Waller profiles (b) obtained after the simulation of the XRD curves for 80 K	97
3.5.7	$\theta - 2\theta$ scans and corresponding simulated curves recorded in the vicinity of (400) reflection for virgin and YSZ crystals irradiated at 573 K.	98
3.5.8	Strain (a) and Debye-Waller profiles (b) obtained after the simulation of the XRD curves for 573 K.	98
3.5.9	$\theta - 2\theta$ scans and corresponding simulated curves recorded in the vicinity of (400) reflection for virgin and YSZ crystals irradiated at 773 K.	99



3.5.10	Strain (a) and Debye-Waller profiles (b) obtained after the simulation of the XRD curves for 773 K	99
3.5.11	$\theta - 2\theta$ scans and corresponding simulated curves recorded in the vicinity of (400) reflection for virgin and YSZ crystals irradiated at 1073 K.	100
3.5.12	Strain (a) and Debye-Waller profiles (b) obtained after the simulation of the XRD curves for 1073 K	100
3.5.13	RBS spectra recorded in random and $\langle 100 \rangle$ - aligned directions on YSZ crystals irradiated with 4-MeV Au ions at the 80 K temperature and indicated fluences	101
3.5.14	Damage fraction (f_D) as a function of depth extracted from the fits to experimental RBS/C data for YSZ crystals irradiated at 80 K temperature	102
3.5.15	RBS spectra recorded in random and $\langle 100 \rangle$ - aligned directions on YSZ crystals irradiated with 4-MeV Au ions at the 573 K temperature and indicated fluences	103
3.5.16	Damage fraction (f_D) as a function of depth extracted from the fits to experimental RBS/C data for YSZ crystals irradiated at 573 K temperature	104
3.5.17	RBS spectra recorded in random and $\langle 100 \rangle$ - aligned directions on YSZ crystals irradiated with 4-MeV Au ions at the 1073 K temperature and indicated fluences	104
3.5.18	Damage fraction (f_D) as a function of depth extracted from the fits to experimental RBS/C data for YSZ crystals irradiated at 1073 K temperature	105
3.6.1	Disorder kinetics plotted from the data obtained by performing RBS/C for YSZ crystals irradiated with 4 MeV Au^{2+} ions at different temperatures.	106
3.6.2	Variation of maximum damage as a function of ion fluence as determined by XRD	107
3.6.3	Variation of maximum strain as a function of ion fluence for different temperatures	108
3.6.4	TEM bright-field micrographs recorded on YSZ crystals with 4 MeV Au^{2+} ions at 300 K and 1073 K and at different places(fluences) of the damage build-up	109
4.3.1	Schematic view of the diffraction geometry and the representation of the template-slicing approach	122
4.3.2	Speedup gain using the template-slicing approach versus the conventional approach.	123
4.3.3	Speedup obtained with the use of an increased number of CPUs in parallel	124
4.3.4	Speedup obtained with the GPU-based computing <i>versus</i> the conventional CPU approach.	125
4.3.5	Computed h scans with increasing number of lattice planes in the y direction	126
4.4.1	RSM of the 004 reflection of a crystal with $1000 \times 1000 \times 1000$ unit-cells containing randomly distributed spherical defects with radius $R_1 = 5nm$ and a lattice mismatch of $\varepsilon = 5\%$	128
4.4.2	(a) Density function corresponding to the probability of finding a defect at a given depth below the surface (b) 100×500 unit cell section of a computed two-dimensional strain field.	129



4.4.3	Calculated diffuse intensities for a 004 reflection of a crystal with $500 \times 500 \times 500$ unit-cells containing randomly distributed spherical defects with different defect sizes	130
4.4.4	Calculated diffuse intensities for a 004 reflection of a crystal with $500 \times 500 \times 500$ unit-cells containing randomly distributed spherical defects with a lattice mismatch of (a) $\varepsilon = 2.5\%$, (b) $\varepsilon = 5\%$ and (c) $\varepsilon = 7.5\%$	132
4.4.5	Calculated diffuse intensities for a 004 reflection of a crystal containing $500 \times 500 \times 500$ unit-cells with varying defect concentrations such as $\langle c \rangle = 0.01, 0.075$ and 0.005 .	133
4.4.6	Computed 004 RSMs with a non-uniform and bimodal distribution of defects: (a) only small defects ($R_1 = 5\text{\AA}$); (b) small and large ($R_2 = 5\text{nm}$) defects; (c) only large defects ($R_2 = 5\text{nm}$). (d) l - scans extracted at $\Delta h = 0$ evidencing the damage-induced streak. (e) h - scans extracted at $\Delta l = -0.03$ evidencing the DXS intensity.	135
4.4.7	Reciprocal space maps recorded in the vicinity of the (400) Bragg reflection for YSZ crystals irradiated with 4 MeV Au^{2+} ions at the fluence of 10^{15}cm^{-2} and at temperatures (a) 80 K (b) 573 K and (c) 1073 K.	136
4.4.8	Probability density function in the case of low (a) and high (b) positional disorder, for LRO (continuous lines) and SRO (dotted lines).	137
4.4.9	Computed 004 RSMs in the case of spherical defects with LRO spatial correlations: (a) low positional disorder ($\sigma_0 = \Lambda / 12$); (b) high positional disorder ($\sigma_0 = \Lambda / 4$). (d) l - scans extracted at $\Delta h = 0$ evidencing the superstructure peaks. (e) h - scans extracted at $\Delta l = -0.05$ evidencing the DXS intensity and the superstructure peaks.	138
4.4.10	Computed 004 RSMs in the case of spherical defects with SRO spatial correlations: (a) low positional disorder ($\sigma_0 = \Lambda / 12$); (b) high positional disorder ($\sigma_0 = \Lambda / 4$). (d) l - scans extracted at $\Delta h = 0$ evidencing the superstructure peaks. (e) h - scans extracted at $\Delta l = -0.05$ evidencing the DXS intensity and the superstructure peaks.	139



General Introduction

Ion irradiation and ion implantation are powerful techniques which are utilized in many fields of materials science : (i) in the microelectronic industry for the doping of semiconductors; (ii) in nanoscale technology, ion irradiation is used to synthesize nanostructured materials, realize nano-patterning and to shape nanoparticles for various physical properties; (iii) ion irradiation is also employed to simulate the various irradiation conditions encountered in extreme environments, such as in the nuclear industry.

In this latter case, a longer and better management of radioactive waste is one of the major fields of research, given the dangerousness of these wastes. Nuclear waste poses various global, political and economic challenges for many countries. For example, the discontinuation of nuclear weapon programs has led to the yield of several thousands of tons of weapon grade and civilian plutonium. Similarly, the energy production by nuclear fission since a few decades has generated huge volumes of spent nuclear fuel which contains highly radioactive elements. Currently, these nuclear wastes are, in France, vitrified in borosilicate glasses, which is a good barrier protection, stored in lead-sealed, ventilated wells (*e.g.*, in La Hague). Though this technology can serve for short-term storage, a better solution is needed for long term storages. For this reason, the advanced nuclear fuel design concepts have recently focused on the inert-matrix fuels (IMFs). Refractory oxide ceramic materials have an advantage to embed radionuclides in their crystal due to their chemical and physical stability. Among the large amount of ceramic oxides, yttria-stabilized zirconia (YSZ) is one of the promising materials that could be used as an IMF.

In the past few decades, a large number of studies have been devoted to the understanding of the behaviour of materials under electron/ion irradiation. One of the main objectives of all these investigations is to understand the damage formation mechanism in out-of-equilibrium environment. For this purpose, many experimental techniques are utilized, the most common ones being, X-ray diffraction (XRD), Rutherford Backscattering Spectrometry in the channelling mode (RBS/C), Raman spectroscopy and transmission electron microscopy (TEM). XRD is highly sensitive to atomic scale displacements while probing macroscopic volumes, which is advantageous for the study of radiation damage. X-ray diffraction techniques have been used from several decades to obtain various information such as the level of strain and damage in irradiated crystals, especially in semiconductor materials or in metals. In this thesis, we make use of well-established X-ray diffraction techniques combined with

advanced data analysis and simulation procedures to study irradiated ceramic materials, mainly cubic zirconia.

This thesis is branched into four chapters. In the first chapter, ion-solid interaction concepts and the application to the cubic zirconia will be presented. Additionally, the theory of kinematical and dynamical theory of diffraction and diffuse X-ray scattering will be introduced. In the second chapter, all the experimental techniques and the computation tools will be presented. Introduction to parallel computing and its implementation is also presented in this chapter. In the third chapter, a comprehensive study of ion irradiated zirconia will be performed, using X-ray diffraction and complementary RBS/C and TEM characterizations. Useful information such as strain and damage buildups obtained for a broad range of temperatures and fluences will be detailed. In chapter 4, we present a simulation procedure for the evaluation of the diffuse scattering from lattice defects in irradiated crystals of large dimensions. Reciprocal space maps corresponding to irradiated zirconia crystals are computed using a combination of multi-processing and GPU-based parallel computing.

The following thesis has been realized in the SPCTS - UMR CNRS 7315 laboratory of the University of Limoges, France. This work was partly financed by the région Limousin.



1

Literature Survey

1.1 INTRODUCTION

ENERGETIC IONS are charged atoms with kinetic energy and when they penetrate into a solid, they interact with the nuclei and electrons of the material through Coulomb forces. These inter-particle interactions depend on many parameters, the most important being the ion velocity and the impact parameter, but also the ion and atom size, atomic number and mass. Usually, the binary collision approximation (BCA) is assumed, in which the energy from an energetic incoming ion is transferred to a single atom of the target *i.e.*, the primary interaction takes place by excitation or scattering of individual atoms. In this case, interaction cross-sections are well defined. Moreover, it is technically straightforward to control the energy, atomic species, direction and number of ions that impinge on a target surface. This degree of control, together with the well-established interaction probabilities between ions and atoms or electrons, make ion beams uniquely powerful tools for quantitatively and controllably analysing and modifying materials over the field of material science.

Historically, the interaction of energetic ions with materials is often associated with the development of nuclear physics. During the World War II, understanding of the problems of radiation damage in nuclear reactor and weapon materials was of main concern. This called for a study of the atomistic processes involved in defect formation and later on, the development of electron microscopy and other techniques further encouraged the investigation. During 1960s and 70s, isotope separators were developed and it provided a convenient source of energetic ions for these radiation damage studies and this

led to ion implantation. It was quickly realised that this process provided a superior doping technology for the emerging semiconductor industry. Ion implantation is one of the most important processing tools in silicon integrated circuit technology [1] [2]. Although the majority of research and development involving ion implantation has been devoted to semiconductors, the technique has also proven to be successful as a means of altering the physical and chemical properties of the near-surface region of metals and alloys [3][4].

Ion beam technologies have been established as indispensable tools in modern materials research, development, and production, and are being employed for both the modification and the characterization of surfaces and thin films of solids. Some of the examples are investigations for materials optimization and waste disposal in nuclear fission and fusion research, the radiation cancer therapy in the health section [5] [6] [7]. They also play an increasing role in emerging technologies which operate at the nanometer scale, such as for mechanical and chemical sensors and new photovoltaic materials, for nanopatterning, and, in general for the creation and analysis of surfaces and thin films with tailored electrical, optical or magnetic properties [8] [9] [10] [11] [12] [13]. Furthermore, there are evidences that the atomic structure and morphology of carbon nanomaterials such as nanotubes and graphene can be changed in a controlled way by irradiation [14] [15]. The arrays of inter-connected carbon nanotubes with different electronic properties can be manufactured by using spatially localized irradiation, which could be fundamental for carbon-based electronics. Interestingly, all the above applications of ion beam technologies rely on the fundamental knowledge of ion-surface interaction which has been mainly established during the past 50 years.

1.2 INTERACTION OF ION BEAMS WITH MATERIALS

Charged particles have their own effects when interacting with solids and in this study, the focus is on ions. When energetic ions penetrate through a solid, they lose energy due to collisions with the electrons and with the target nuclei. Depending on the energy (or rather, on the velocity) of the incident particle, this interaction is broadly differentiated into inelastic (due to electrons) and elastic (due to screened nucleus) interactions. Inelastic interaction occurs at high energies (roughly > 1 MeV/amu) whereas for lower energies (*i.e.* $< \sim 10$ keV/amu), elastic interaction takes place. Figure (1.1.1) shows the two different types of energy losses as a function of the energy (or velocity) of the particles.

STOPPING POWER

When the ions travel through the solid, they slow down and gradually transfer energy to the orbital electrons and nuclei resulting in their energy losses. This slowing-down process is defined by the energy



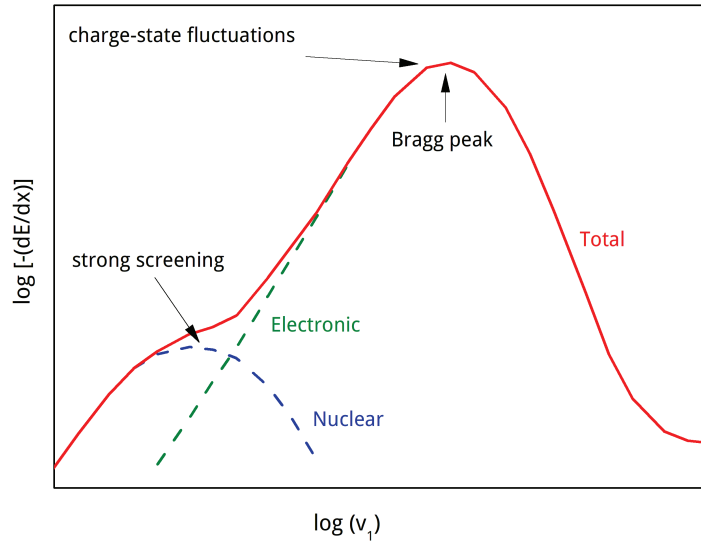


Figure 1.1.1: Schematic representation of the variation of electronic energy loss, S_e and nuclear energy loss, S_n with ion velocity

loss of the particle, which is the amount of energy transferred per unit length (dE/dx). Energy loss is not constant and depends on various factors such as nature and initial energy of the ion, the composition of the target material *etc.* The total energy loss is given by the sum of electronic and nuclear contributions and is written as:

$$\frac{dE}{dx} = \left(\frac{dE}{dx}\right)_n + \left(\frac{dE}{dx}\right)_e \quad (1.1)$$

The former term is called nuclear energy loss and refers to the energy loss per unit length *via* nuclear collisions between ion and nuclei, while the second term is called electronic energy loss and holds for the energy loss per unit length due to electronic interaction.

One frequent unit of measure for dE/dx is $keV.nm^{-1}$. It is also common to define the stopping cross-section S , which is the energy loss per unit length per scattering center: $S = 1/N(dE/dx)$ where N is the atomic density of the solid. For instance, in the case of Ytria-stabilized zirconia (YSZ) irradiated with 4 MeV Au ions (since this material is extensively studied in this thesis), the nuclear energy loss regime is predominant, with a nuclear stopping power of $\sim 5keV/nm^{-1}$. However, electronic energy loss is significant and might also play a role in the defect creation process (See section 1.6).

¹This value was determined with the help of SRIM calculations. SRIM (Stopping and Range of Ions in Matter)[16] is a Monte-Carlo program that allows simulation of ion/matter interactions.

1.3 DEFECT CREATION VIA ELASTIC NUCLEAR INTERACTION

The interaction of ions with matter creates different types of defects depending on the nature of interaction and the amount of energy transferred, and above all, on the target material. Long time irradiation of a material could lead to significant modifications in the properties of the materials such as mechanical resistance, thermal and electrical conductivity *etc.* Hence it is necessary to understand the behaviour of the material under highly irradiating conditions. But prior to that, the knowledge of primary stages are crucial. In this work, the focus is mainly on the low energy irradiation effects on defect generation.

As described previously, the cross-section for elastic nuclear collision is higher for low energy ions. The elastic conservation of momentum holds good for interactions. The collision results in the transfer of energy from the ion to the atomic nucleus. The minimum energy required to permanently displace an atom from its lattice site is called the *displacement threshold energy* E_d . If the transferred energy to the lattice atom is greater than the threshold energy E_d , the atom will be permanently ejected from its position. This displacement of the atom results in an empty lattice site, known as vacancy and in an atom in interstitial position; both vacancy and interstitial form a Frenkel pair. The first displaced atom [also called primary knock-on atom (PKA)] might carry sufficient energy to induce secondary displacement(s). These secondary displaced atoms in turn can create further displacements and this process may continue leading to a series of displacements. In the end, a highly disordered region around the path of the ion is generated which is known as a collision cascades. Collision cascades usually happen at the terminus of ion's trajectory and the set of point defects created is known as a displacement cascade. Kinchin and Pease [17] created a model half a century ago to estimate the number of displacements which is given by

$$\begin{aligned} N_d &= 0 && \text{if } T < E_d \\ N_d &= 1 && \text{if } E_d \leq T < 2E_d \\ N_d &= T/2E_d && \text{if } T \geq 2E_d \end{aligned}$$

where T is the kinetic energy of the primary knock-on atom. In the first case, the target atom will not be displaced whereas in the second case, it is displaced which gives rise to a Frenkel pair. In the third case, target atom is displaced from its site and becomes a projectile which leads to collision cascades. The number of displacements per atom (dpa) represents a way to estimate irradiation-induced disorder in the material. dpa is calculated as a ratio of the number of displaced atoms per unit volume on the atomic density of the material. During the collision cascades, interstitials and vacancies might easily recombine since they are produced very close to each other. This recombination results in the more or less pronounced annihilation of the collision cascades. Hence, depending on the material, only a very low percentage of the initially created point defects may survive. Defect accumulation and agglomeration may take place by increasing the number of projectiles.



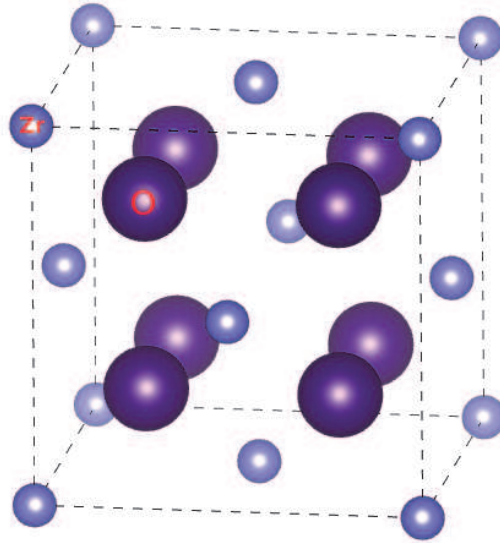


Figure 1.4.1: Crystalline structure of cubic Zirconia (ZrO_2) where the bigger circles represent the O atoms and the smaller circles represent the Zr atoms

1.4 THE MATERIAL - ZIRCONIA

Zirconium dioxide (ZrO_2) or zirconia is a polymorphic ceramic material which exists in three well-known structural phases, namely monoclinic, tetragonal and cubic. The natural form is obtained from the mineral baddeleyite which has a monoclinic crystalline structure. The three crystal structures below the melting point of $2715\text{ }^\circ\text{C}$ are [18]

- (i) monoclinic for temperatures $< 1,170\text{ }^\circ\text{C}$
- (ii) tetragonal between $1,170 - 2,370\text{ }^\circ\text{C}$
- (iii) cubic for temperatures $> 2,370\text{ }^\circ\text{C}$, which is isostructural with fluorite (CaF_2)

The high temperature tetragonal and/or cubic phases are stabilized down to room temperature by blending zirconia with some oxides like MgO , Y_2O_3 , TiO_2 , CaO , Ce_2O_3 . The crystal structure of cubic Zirconia (ZrO_2) is illustrated in figure (1.4.1). The structure of cubic zirconia can be represented by a cubic lattice of oxygen ions where half of the cubes are occupied by zirconium ions.

1.5 WHY CUBIC ZIRCONIA?

Ytria (Y_2O_3) stabilized cubic zirconia (YSZ) is an extensively studied oxide ceramic material, having numerous applications in the fields of bio-ceramics, sensors, nanomaterials, and nuclear waste management. Another major application of YSZ is in Solid Fuel Cell (SOFC) technology [19] and it is also



Formula	$ZrO_2 - Y_2O_3$
Structure	Fluorite CaF_2
Density	5.92 g.cm^{-3}
Bulk lattice parameter	0.5145 nm
Melting point	2715 °C
Thermal conductivity	$2 \text{ W.m}^{-1}\text{K}^{-1}$
Y_2O_3 percentage	$\sim 8 - 20 \%$ mol

Table 1.5.1: Characteristics and properties of YSZ

widely used as Thermal Barrier Coating (TBC) [20]. There is also a growing interest in the electrical properties of YSZ [21] [22]. Some of the properties of YSZ are listed in table (1.5.1).

By the end of the last century, the discontinuation of nuclear weapon programs and increasing production of reprocessed plutonium from the electronuclear programs have led to the yield of thousands of tons of weapon grade and civilian plutonium [23][24]. There are also huge risks because it also contributes to the largest radiotoxicities of conventional spent fuels after some 100 years. So to handle this excessive plutonium, the advanced nuclear fuel design concepts have recently focused attention on the inert-matrix fuels (IMF)² [26]. The reason behind this is mainly because (i) these fuels burn plutonium or other actinides such as americium instead of uranium; (ii) the actinide inventory in the spent fuel is significantly reduced compared to conventional uranium fuels. It is also encouraged to convert excessive plutonium into mixed-oxide (MOX) fuel and to irradiate this fuel in commercial nuclear power reactors. YSZ could also be used as a transmutation matrix or as a matrix for nuclear waste confinement in geological disposal. Of all the non-fertile material candidates for inert matrix fuels, YSZ is one of the most promising material [7]. This high temperature refractory oxide is attractive mainly because it possesses the same crystallographic structure as oxides of actinides (like UO_2), high chemical durability and excellent radiation stability characteristics [27]. It has been proposed that burning plutonium in a non-fertile fuel based on a zirconia matrix may constitute a final waste form [28] [29].

More specifically, the properties which make YSZ suitable for nuclear waste management applications are its (i) high solubility of actinides within it, (ii) insolubility in aqueous and acidic medium, (iii) redox insensitivity and (iv) high melting point. Needless to say, either during Pu-incineration or transuranic transmutation, the host YSZ matrix will get exposed to extreme radioactive environments involving ballistic and ionization processes. Materials properties are likely to undergo changes under such aggressive environment and it is therefore important to carry out experimental studies so as to predict such changes.

²IMF refers to any nuclear fuel containing a low activation matrix as a carrier for the fissile material. At present, the term IMF is mostly associated with plutonium fuel that does not contain uranium to obtain the highest efficiency for destruction of excess plutonium. Besides that, the term IMF is also used in the context of uranium-free fuels for transmutation of minor actinides, although in many cases this is not appropriate as the fissile content is too low for fuel purposes [25].



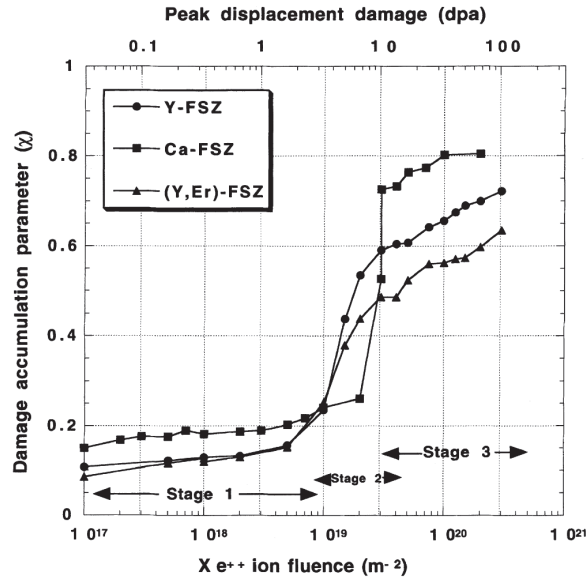


Figure 1.6.1: Damage accumulation in FSZ samples irradiated with Xe^{++} ions at 170 K. Damage accumulation occurs in three stages [27].

1.6 LITERATURE SURVEY ON YSZ UNDER ION IRRADIATION

The investigation of radiation damage effects in zirconia has been done by various researchers in the last two decades with the help of advanced experimental characterization techniques such as X-ray Diffraction (XRD), Transmission Electron Microscopy (TEM) and Rutherford backscattering and ion channelling (RBS/C) [24] [30] [31] [32] [33] [34] [35]. Some of the important results are presented here. Sickafus *et. al.*, in 1998, [27] [36] [37] [38] irradiated the unstabilized monoclinic zirconia and fully-stabilized cubic zirconia (FSZ) with Y, Ca and Er dopants. Irradiations were done with 340-400 keV Xe^{++} ions and at temperatures ranging from 170 to 300 K. They performed experiments using XRD, TEM and RBS/C. By RBS/C, they observed the damage accumulation in Xe-ion irradiated FSZ crystals progress in three stages (See figure 1.6.1). The first stage is the formation of isolated defect clusters and in the second stage, the damage increases significantly and finally in the last stage, the damage level saturates. The formation of a network of tangled dislocations is noticed. They observed no amorphization under any of the performed irradiation conditions. The unstabilized monoclinic zirconia was observed to transform to a higher symmetry, tetragonal or cubic phase, upon 300 - 400 Xe^{2+} ion irradiation and no amorphization was observed up to Xe fluence equivalent to 680 dpa.

They also irradiated cubic stabilized zirconia with 72 MeV I^+ ions to simulate a typical U or Pu fission fragment [36]. Irradiations were performed over the fluence range from 1×10^{14} to $5 \times 10^{15} cm^{-2}$, at temperatures of 300, 700 and 1170 K. At ambient temperature and at the highest I^+ fluence ($5 \times 10^{15} I^+/cm^2$), RBS/C measurements revealed a high degree of lattice disorder. Nano-indentation measurements on the same sample indicated a decrease in elastic modulus, E , and hardness, H (both by about 9 %). These results suggest that an alteration in structure beyond simple defect accumulation occurs

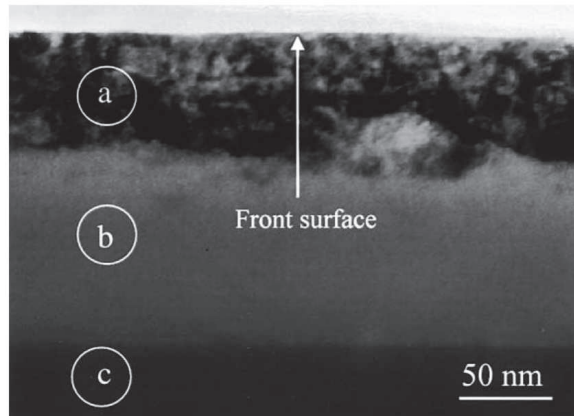


Figure 1.6.2: Bright-field TEM micrograph of a cross-section of YSZ irradiated with 400 keV Cs ions at a fluence of $1 \times 10^{17} \text{ cm}^{-2}$ in room temperature. The damaged surface layer (a), amorphous layer (b) and the virgin layer which is beyond the irradiation zone (c) can be clearly observed from Wang *et. al.* [40]

under these irradiation conditions. However, TEM observations and in particular micro-diffraction measurements failed to reveal any structural transformations in the irradiated material. Using RBS/C analyses, damage accumulation was found to saturate at much higher values ($<770 \text{ K}$) compared to the Xe^{++} ions. They suspected partial amorphization of the sample but however they were unable to confirm using TEM.

Wang *et.al.*, in 2000 [39] were able to observe amorphization of YSZ submitted to the 400-keV Cs-ion implantation to $1 \times 10^{17} \text{ cm}^{-2}$ at room temperature. The Cs concentration at which amorphization of YSZ occurred is about 8 at. % which is well above the typical value that could be reached in an inert fuel matrix. A year later, Wang *et. al.*, [40] confirmed the formation of the amorphous layer in YSZ with the same conditions as above using TEM (see figure 1.6.2). TEM image shows the depth dependent microstructure of YSZ. They speculated that amorphization occurs because monovalent Cs ions, which possess a relatively large ionic radius, disrupt the local atomic configuration in cubic YSZ.

Yasuda *et. al.* [41] investigated the defect clusters induced in FSZ irradiated with ions and/or electrons. Micro-structure evolution of YSZ ($\text{ZrO}_2 - 13 \text{ mol}\% \text{ Y}_2\text{O}_3$), was investigated using TEM. Anomalous formation of large defect clusters was found under electron irradiation subsequent to ion irradiation, such as 300 keV O^+ , 100 keV He^+ and 4 keV Ar^+ ions. Such defect clusters were not formed solely with ion irradiation. The defect clusters were transformed into a dislocation network when they reached a critical diameter of about $1.0 - 1.5 \mu\text{m}$, and processes of nucleation, growth and transformation were repeated under electron irradiation. The defect clusters were assumed to be oxygen platelets induced through selective displacements of oxygen ions in YSZ with electron irradiation. The results suggest an important role of low energy recoils and/or electronic excitation for the radiation damage processes in YSZ, which induce selective radiation damage in the oxygen sublattice of YSZ.

Thomé and colleagues [42] studied the damage production in yttria-stabilized cubic zirconia single



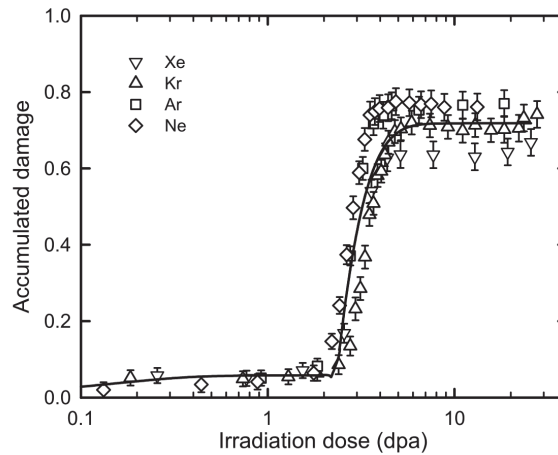


Figure 1.6.3: Damage kinetics of YSZ irradiated at room temperature with various noble-gas ions [43]

crystals irradiated with low-energy (from 30 to 450 keV) ions (from He to Cs). The disorder created in the two sub-lattices (Zr^{4+} and O^{2-}) of the crystals and the lattice sites of ions were determined by *in situ* Rutherford backscattering and channelling experiments. Damage was created at a depth close to the ion projected range estimated with SRIM at low fluences which later proceed towards greater depths with increasing fluences once the saturation of the radiation damage was reached. The kinetics of the damage accumulation process revealed three stages, which (except for He) essentially depended on the number of displacements per atom (dpa) induced by irradiating ions (ballistic contribution). Channelling results show that the lattice location of the heaviest atoms (Xe, Cs and I) varied with the nature of implanted species (chemical contribution). The position of Xe and I ions is almost random over the whole fluence range investigated, meanwhile a large fraction of Cs ions is located in substitutional lattice sites at low ion fluences. At high fluences, Cs loses its substitutionality and this could be due to the precipitation of implanted species or the formation of compounds (such as Cs_2ZrO_3), which may explain the eventual amorphization. Formation of precipitates was further confirmed by Wang *et al.* [39].

Similarly, Jagielski *et al.*, [43] showed that, even after a huge irradiation dose of 100 displacements per atom (dpa), the disorder level saturates at a moderate value ($\sim 70\%$) (See figure 1.6.3). There was no indication on any phase change or amorphization in the sample. This result has been obtained under various irradiation conditions, namely Xe (450 keV), I (200 keV), Kr (300 keV), Ar (160 keV), Ne (80 keV) and Cs (300 keV).

Costantini *et al.*, [44] investigated YSZ using electron irradiation. $\langle 100 \rangle$ - or $\langle 110 \rangle$ - oriented YSZ single crystals were irradiated with 2.5 MeV electrons and also with different swift ion irradiation. Investigation was performed using X-band electron paramagnetic resonance (EPR) and UV - visible optical absorption measurements to monitor the point defect formation. They noticed the electron and ion

beams produce the same two paramagnetic centres : (i) the A-centre, identified as an F^+ -type centre with an axial $\langle 100 \rangle$ symmetry, which is induced by the elastic collisions, (ii) and the B-centre similar to the well-known T-centre with an axial $\langle 111 \rangle$ symmetry. They suspected that the latter defect was probably produced by the electronic excitations deposited in the material by the charged particles.

Recently, a comprehensive work was proposed by Moll *et. al.*, [34] regarding the behaviour of YSZ under low and medium energy irradiation. The comprehensive study was performed by using RBS/C, XRD and TEM, and the information was gained on the disorder buildup, the nature of the defects and the mechanisms involved in the structural transformations. XRD results showed the presence of a dilatation gradient along the direction normal to the sample surface and a positive strain induced by defects. The damage buildup determined by RBS/C and the variation in the maximum normal elastic strain as a function of the ion fluence measured by XRD were presented in the framework of MSDA model. Multi-step damage accumulation model (MSDA) was developed by Jagielski and Thomé [43] [45] [46] to account for a theoretical description of the damage accumulation kinetics. This model is based on the assumption that the damage accumulation process occurs *via* a series of structural transformations, each step being described by a direct impact mechanism. The transformation of the irradiated material into a new structure is triggered by the destabilization of the current structural organization of the crystal leading to the next step of damage accumulation.

According to the MSDA model, the variation of the level of damage accumulation f_D with the ion fluence Φ is represented by the equation [45] :

$$f_D = \sum_{i=1}^{m-1} \{f_{D,i}^{sat} G[1 - \exp(-\sigma_i(\Phi - \Phi_i))] \times \prod_{k=1}^{i-1} [\exp(-\sigma_{k+1}(\Phi - \Phi_{k+1}))]\} + f_{D,m}^{sat} G[1 - \exp(-\sigma_m(\Phi - \Phi_m))] \quad (1.2)$$

where n is the number of steps required to describe the disordering process, $f_{D,i}^{sat}$ is the level of damage at saturation in the i th step, σ_i is the cross-section for damage formation in the i th step, G is a *ad-hoc* function which transforms negative values into 0 and leaves positive values unchanged. Moll *et. al.*, [34] evidenced a three step variation (using MSDA) of the YSZ by RBS/C in the fluence range up to $2 \times 10^{16} \text{cm}^{-2}$. At low fluences (up to 10^{15}cm^{-2}), the first step corresponds to a regular increase in the damage yield and the strain by the formation of small defect clusters. A sharp increase in the damage yield, together with a dramatic drop of the strain, is observed in the second step (from 10^{15} to $5 \times 10^{15} \text{cm}^{-2}$) due to the formation of dislocation loops which collapse in a network of tangled dislocations. Finally, in the third step at high fluences (above $5 \times 10^{15} \text{cm}^{-2}$), where a decrease in the channelling yield is observed, which is ascribed to the reorganization of the dislocation network in weakly damaged regions. The results were compared with the damage formation in low-energy ions [42] and they concluded that several factors such as the effects due to the modification of the composition of materials during irradiation must be taken into account to untangle damage accumulation processes and infer damage buildups. They also compared the results with high energy (940 MeV Pb ions) and the damage buildup with the help of MSDA model [figure (1.6.4)] showed a direct transformation into a



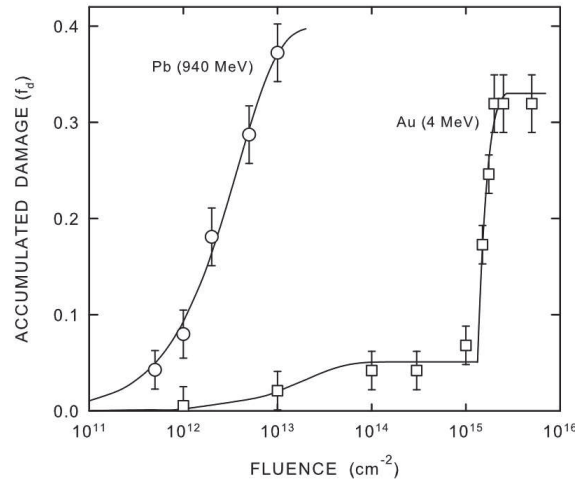


Figure 1.6.4: Accumulated damage f_D versus fluence in YSZ crystals. The solid line represents the fit made by using the MSDA model [47].

new structure *via* a single-step process in the case of high energy ions [47].

In summary, zirconia presents a very high resistance to ion irradiation with no amorphization discovered up to hundreds of dpa. All these above studies show a high chemical stability and radiation resistance of YSZ. Nonetheless, the complete understanding of its behaviour under irradiation is an ongoing process. Indeed, detailed studies still need to be conducted in particular regarding the effect of the irradiation temperature. This will be the motivation of part of the work presented in this manuscript.

1.7 INTRODUCTION TO THE THEORY OF X-RAY DIFFRACTION

In the previous section, we saw in detail, the interaction of ion beams with materials and how the irradiation with ions induce defects in the target material and consequently, changes the properties of the material. A rather broad panoply of experimental characterization techniques such as X-ray Diffraction (XRD), Transmission Electron Microscopy (TEM) and Rutherford backscattering and ion channelling (RBS/C) are typically used to investigate materials at various spatial scales and with different sensitivities. When using interferometric techniques, wavelengths similar to the atomic distances of $\sim 1 \text{ \AA}$ are required. When radiation of such short wavelength is scattered, the resulting interference pattern is related to the details of the arrangement of atoms in the crystal. Therefore, analysis of the pattern allows us to study the violations of the crystal perfection on this scale and precisely determine atomic displacements. For example, lattice parameters can be measured with a precision down to 10^{-4} \AA .

Both TEM and XRD rely on the constructive interference of scattered waves, and the same fundamental laws (*e.g.* Bragg's law, extinction rules) can be applied for the interpretation of the resulting diffraction patterns. TEM is a very efficient and widespread technique used to analyse defects in irradiated materials. It has an advantage of being able to obtain the direct imaging and the latest developments allow

to access displacements as low as 0.43\AA [48]. In contrast, conventional XRD does not rely on imaging, but it is a non-destructive technique. It doesn't require sample preparation and since large volumes are probed, it is a statistically relevant technique. X-rays can easily be monochromatized and allow the precise determination of the lattice constants as well as the strain state of the materials. The coherence length, the penetration depth as well as the dynamic range for detection are higher for X-rays than for electron diffraction. The counterpart to that is that the information is not straightforward to obtain, *i.e.* we have to build models to obtain the relevant information. The reason for that is, in a typical XRD experiment we measure the scattered intensity (the squared modulus of the amplitude) where the phase information is lost, so that the electron density distribution can not be obtained by a simple inverse Fourier transform.

X-ray analysis is considerably used for the analysis of thin films and multilayers [49]. The diffraction techniques also make a significant contribution to the studies of defects in crystals, particularly those defects that are produced by irradiation and plastic deformation. For example, it yields information on the types of the point defects (vacancies, interstitials, impurity atoms), their positions in the crystal lattice, their concentrations, and the static displacement fields around them.

1.8 PRODUCTION OF X-RAYS

X-rays produced in the laboratory diffractometers have wavelengths varying in the range approximately $0.1 - 5\text{\AA}$. A typical diffractometer consists of a source of radiation, a monochromator, slits to adjust the shape of the beam and a detector. X-rays are produced by classical sealed tubes or rotating anode generators. In the recent decades, the use of synchrotron to produce X-rays have become increasingly popular. The synchrotron takes its name from a specific type of particle accelerator. Synchrotron radiation has become a generic term to describe radiation from charged particles travelling at relativistic speeds in applied magnetic fields which force them to travel along curved paths. In a storage ring, the synchrotron radiation is produced either in the bending magnets needed to keep the electrons in a closed orbit, or in insertion devices such as wigglers or undulators situated in the straight sections of the storage ring. Several aspects of an X-ray source determine the quality of the X-ray beam it produces. These aspects can be combined into a single quantity, called the brilliance, which allows one to compare the quality of X-ray beams from different sources. Brilliance can be written as

$$\text{Brilliance} = \frac{\text{Photons/second}}{(\text{mrad})^2 (\text{mm}^2 \text{source_area}) (0.1\% \text{BW})} \quad (1.3)$$

The intensity in photons per second is the product of the brilliance, angular divergences set by the horizontal and vertical apertures (in milli-radian), the source area (in mm^2), and the relative bandwidth of the monochromator crystal relative to 0.1% . The brilliance is a function of the photon energy. The maximum brilliance from third generation undulators (see figure 1.8.1) is approximately 10 orders of



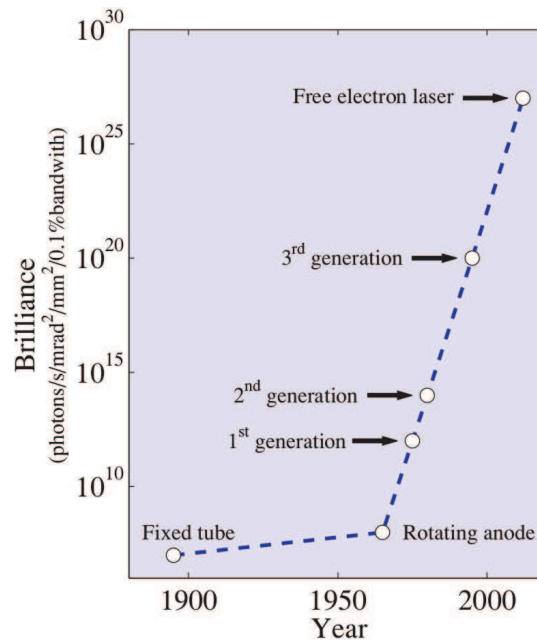


Figure 1.8.1: The brilliance of X-ray sources as a function of time.

magnitude higher than that from a rotating anode at the $\text{Cu } K_{\alpha}$ line. This dramatic improvement has in many ways led to a paradigm shift in experimental X-ray science. Experiments inconceivable only a few decades ago are now performed on almost a routine basis.

Up until now, three generations of synchrotron radiation sources emitting radiation have been developed. The fourth generation, based on free-electron lasers, produces high power and ultrafast pulses of highly coherent radiation and is the topic of intense research.

1.9 KINEMATICAL THEORY OF DIFFRACTION

Since the discovery of X-ray diffraction in crystals in 1912, it has been a powerful tool in the study of crystal structures. There are two general diffraction theories that are employed to explain the observed X-ray diffraction phenomena in crystals, the kinematical and the dynamical theory. The dynamical theory will be shortly presented in section (1.12). In the kinematical theory, the diffracted wave is constructed by the addition of the coherently scattered waves from all crystal atoms, with the assumption that the transmitted X-rays only suffer normal linear absorption and the waves only undergo single scattering (*i.e.*, multiple scattering is neglected). If these scattered waves are all in phase, they constructively interfere and a maximum (*i.e.*, Bragg peak) is observed in the spatial distribution of the scattered waves. If they are out of phase, the resultant diffracted wave amplitude will be cancelled to zero. The validity of the kinematical approximation depends on various factors like the crystals dimensions, strength of the scattering, crystalline perfection, scattering geometry *etc.*

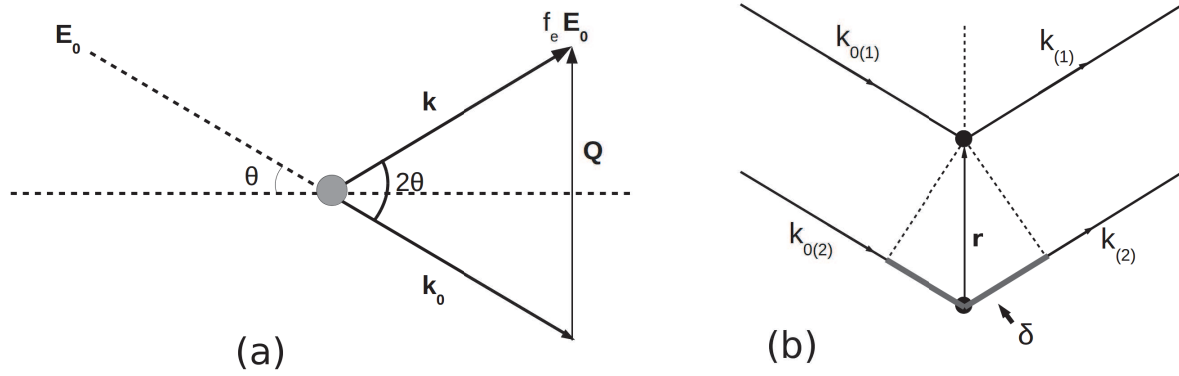


Figure 1.9.1: (a) Representation of scattering by one electron where the incident and the diffracted wave vectors and the associated scattering vector are shown. (b) The case of scattering by two electrons where the path difference is given by δ

The fundamental scattering process is the interaction of the incident photons with the electric field of the electron. The details of this scattering process, especially the separation of the elastic and inelastic scattering contribution at large scattering vectors, must be calculated by quantum mechanics. However, the elastic scattering cross section can be quantitatively understood by a classical calculation of the induced dipole radiation of the electron, that yields the Thomson scattering cross section:

$$\frac{d\sigma}{d\Omega_{Th}} = \left| \frac{e^2}{mc^2} \right|^2 \frac{1 + \cos^2 2\theta}{2} \quad (1.4)$$

e^2/mc^2 is the classical radius of the electron and its square is generally used as a reference unit for X-ray scattering cross sections. The second factor of equation (1.4) is the polarization factor of the incoming wave and here it is given for the case of a non-polarized incoming wave.

This is the Thomson equation for the scattering of an X-ray beam by a single electron. If the values of the constants e, r, m and c are inserted into this equation, it will be found that the intensity of the scattered beam is only a minute fraction of the intensity of the incident beam.

In the case of elastic scattering of X-rays, the wave vectors of the primary and scattered waves have the same length in vacuum:

$$|\mathbf{k}_0| = |\mathbf{k}| = \frac{2\pi}{\lambda} \quad (1.5)$$

where λ is the X-ray wavelength.

When a crystal is irradiated with a monochromatic plane wave (figure 1.9.1 a), the incident wave amplitude is given by

$$\mathbf{E}_0(\mathbf{R}, t) = \mathbf{E}_0 \exp[i(\mathbf{k}_0 \cdot \mathbf{R} - \omega t)] \quad (1.6)$$

and the scattered amplitude is given by

$$\mathbf{E}_0(\mathbf{R}, t) = f_e \mathbf{E}_0 \exp[i(\mathbf{k} \cdot \mathbf{R} - \omega t)] \quad (1.7)$$



where f_e is the scattering length of the electron. Typical measurement times are of the order of 1 second, which corresponds to 10^{18} time periods of the X-ray radiation. The intensity of the wavefield is therefore given by the time-averaged multiplication of the amplitudes and is given by

$$I(\mathbf{R}, \mathbf{R}') = \langle E(\mathbf{R})E^*(\mathbf{R}') \rangle \quad (1.8)$$

For simplicity, the ωt term will hence be omitted in the following. If there are several scattering centers, there is a phase shift between the different scattered waves that has to be considered in the calculation of the total scattering amplitudes. The resulting amplitude E' , for instance, from the two scattering centers (figure 1.9.1 b) is

$$E' = f_e E_0 [\exp(i\mathbf{k} \cdot \mathbf{R}) + \exp(i\mathbf{k} \cdot \mathbf{R} + \varphi)] \quad (1.9)$$

where $\varphi = 2\pi/\lambda \times \delta$ is the phase lag of the wave from electron 1 behind that of electron 2 and

$$\varphi = \mathbf{k} \cdot \mathbf{r} - \mathbf{k}_0 \cdot \mathbf{r} = (\mathbf{k} - \mathbf{k}_0) \cdot \mathbf{r} = \mathbf{Q} \cdot \mathbf{r} \quad (1.10)$$

where \mathbf{r} is the distance separating the electrons and \mathbf{Q} is the diffraction vector length for X-rays and is given by

$$\mathbf{Q} = \frac{4\pi}{\lambda} \sin \theta \quad (1.11)$$

So the amplitude becomes

$$E' = f_e E_0 \exp(i\mathbf{k} \cdot \mathbf{R}) [1 + \exp(i\mathbf{Q} \cdot \mathbf{r})] \quad (1.12)$$

Generalizing to an arbitrary number of electrons

$$E' = f_e E_0 \exp(i\mathbf{k} \cdot \mathbf{R}) \sum_l \exp(i\mathbf{Q} \cdot \mathbf{r}_l) \quad (1.13)$$

where \mathbf{r}_l is the position of the l th electrons. The scattering length of the system as a whole is therefore given by

$$f = f_e \sum_l \exp(i\mathbf{Q} \cdot \mathbf{r}_l) \quad (1.14)$$

When an X-ray beam encounters an atom, each electron in it scatters part of the radiation coherently in accordance with the Thomson equation. One might also expect the nucleus to take part in the coherent scattering, since it also bears a charge and should be capable of oscillating under the influence of the incident beam. However, the nucleus has an extremely large mass relative to that of the electron and cannot be made to oscillate to any appreciable extent; in fact, the Thomson equation shows that the intensity of coherent scattering is inversely proportional to the square of the mass of the scattering particle. For the scattering from an atom, considering that electrons are spread as a continuous charge



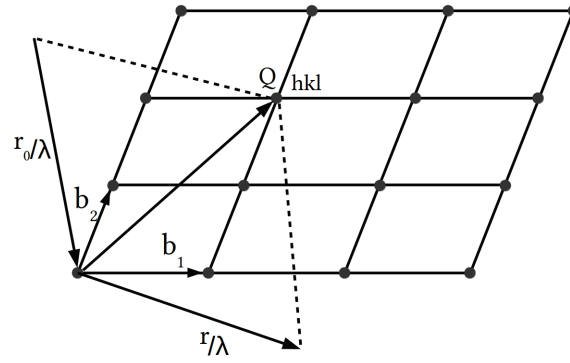


Figure 1.9.2: Reciprocal lattice representation which satisfies the Bragg's law for a set of planes hkl

cloud over the volume of the atom

$$f(\mathbf{Q}) = f_e \sum_l \exp(i\mathbf{Q} \cdot \mathbf{r}_l) \longrightarrow f_e \int \exp(i\mathbf{Q} \cdot \mathbf{r}) \rho(\mathbf{r}) d^3 \mathbf{r} \quad (1.15)$$

where $f(\mathbf{Q})$ is the atomic scattering vector or atomic form factor.

The crystallographic unit cell is the smallest unit by which the periodic order is repeated. The scattering length of a unit-cell is the structure factor \mathbf{F} and using the same approach to derive equation (1.14), the structure factor is defined as the amplitude scattered by one unit cell and is given by

$$F = \sum_m f_m(\mathbf{Q}) \exp(i\mathbf{Q} \cdot \mathbf{r}_m) \quad (1.16)$$

Hence, the overall diffracted amplitude from a crystal (*i.e.*, a periodic distribution of unit-cells) is just the sum of the amplitudes scattered by each unit cell within the sample

$$E(\mathbf{Q}) = \sum_n F_n(\mathbf{Q}) \exp(i\mathbf{Q} \cdot \mathbf{r}_n) \quad (1.17)$$

Equation (1.17) is a Fourier series and therefore exhibit maxima when its argument ($\mathbf{Q} \cdot \mathbf{r}_n$) equals multiple of 2π . Finding the conditions for which $\mathbf{Q} \cdot \mathbf{r}_n = n \times 2\pi$ correspond to establishing the diffraction condition.

RECIPROCAL SPACE

In order to find the vectors of the above Fourier series, we construct the axis vectors $\mathbf{b}_1, \mathbf{b}_2, \mathbf{b}_3$ of the *reciprocal lattice* (Figure 1.9.2)

$$\mathbf{b}_1 = \frac{\mathbf{a}_2 \times \mathbf{a}_3}{\mathbf{a}_1 \cdot (\mathbf{a}_2 \times \mathbf{a}_3)}; \mathbf{b}_2 = \frac{\mathbf{a}_3 \times \mathbf{a}_1}{\mathbf{a}_1 \cdot (\mathbf{a}_2 \times \mathbf{a}_3)}; \mathbf{b}_3 = \frac{\mathbf{a}_1 \times \mathbf{a}_2}{\mathbf{a}_1 \cdot (\mathbf{a}_2 \times \mathbf{a}_3)} \quad (1.18)$$



If $\mathbf{a}_1, \mathbf{a}_2, \mathbf{a}_3$ are primitive vectors of the crystal lattice, then $\mathbf{b}_1, \mathbf{b}_2, \mathbf{b}_3$ are the primitive vectors of the reciprocal lattice. Each vector defined by equation (1.18) is orthogonal to two axis vectors of the crystal lattice. Thus $\mathbf{b}_1, \mathbf{b}_2, \mathbf{b}_3$ have the property

$$\mathbf{b}_i \cdot \mathbf{a}_j = \delta_{ij} \quad (1.19)$$

where $\delta_{ij} = 1$ if $i = j$ and $\delta_{ij} = 0$ if $i \neq j$. Points in the reciprocal lattice are mapped by the set of vectors

$$\mathbf{G} = h\mathbf{b}_1 + k\mathbf{b}_2 + l\mathbf{b}_3 \quad (1.20)$$

where h, k and l are integers. The vectors \mathbf{b}_i and their linear combinations are referred to as *reciprocal lattice vectors* because their dimension is m^{-1} and their length is inversely proportional to the length of the corresponding real lattice vectors. They span the so-called *reciprocal lattice*. Since in equation (1.17), \mathbf{r}_n is a vector of the real space lattice, $\mathbf{r}_n = u\mathbf{a} + v\mathbf{b} + w\mathbf{c}$ (u, v, w integers), the product

$$2\pi\mathbf{G} \cdot \mathbf{r}_n = 2\pi(hu + kv + lw) = n \times 2\pi \quad (1.21)$$

which fulfils the diffraction condition.

In other words, $\mathbf{Q} = 2\pi\mathbf{G}$ is a diffraction condition, *i.e.*, a diffraction peak is observed when the scattering vector is equal to a reciprocal lattice vector. Graphically this corresponds to the Ewald construction (Figure 1.9.3). The Ewald sphere is defined by its center A and radius $R = 1/\lambda = k_0$. Since the wave vectors \mathbf{k} and \mathbf{k}_0 have the same length and lie in the same sphere, the scattering vector must lie on the surface of the sphere. Consider the end of the vector \mathbf{k}_0 as the origin O of the reciprocal lattice, the Ewald sphere defines the locus of points of all possible scattering vectors. When the Ewald sphere intersects a reciprocal lattice point, diffraction is observed for these planes.

From the properties of the reciprocal lattice, $G = 1/d_{hkl}$ where d_{hkl} is the planar spacing of the (h, k, l) planes. The above diffraction condition is therefore equivalent to Bragg's law

$$\frac{2 \sin \theta}{\lambda} = \frac{1}{d_{hkl}} \quad (1.22)$$

Returning to the equation (1.17), using the periodicity of the Fourier series, we finally obtain

$$E(\mathbf{Q}) = \sum_{\mathbf{G}} \int d\mathbf{r} \cdot F(\mathbf{Q}) \exp[i(\mathbf{Q} - \mathbf{G})\mathbf{r}] \quad (1.23)$$

Equation (1.23) shows that the diffracted amplitude is located around points with coordinates given by the reciprocal lattice vectors \mathbf{G} and the shape of the amplitude distribution is given by the integral term.



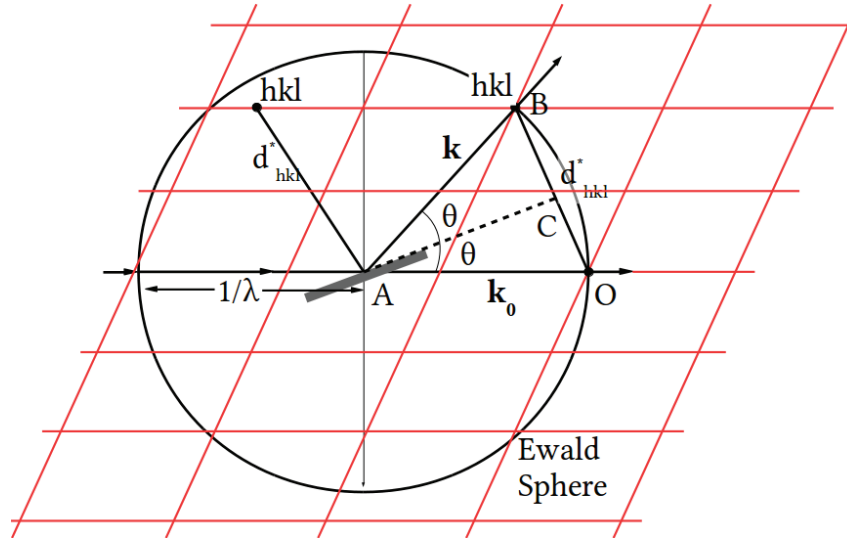


Figure 1.9.3: Geometrical representation of the Ewald construction.

1.10 EFFECTS OF MICROSTRUCTURE

Equation (1.23) assumes infinite extension for the integral and all unit cells located at their theoretical position. Real crystal have finite dimension and exhibit a certain amount of lattice disorder, where the unit-cells are shifted by an amount $\mathbf{u}(\mathbf{r})$. Now we take into account $\mathbf{u}(\mathbf{r})$, the lattice displacement at the point \mathbf{r} and $\Omega(\mathbf{r})$ as the crystallite shape function (equal to 1 inside the crystal, and 0 outside). The phase term becomes $\exp[i\mathbf{Q}(\mathbf{r} + \mathbf{u})]$ and, in the small displacements approximation, we have $(\mathbf{Q} - \mathbf{G}) \cdot \mathbf{u} \ll 1$, so that $\mathbf{Q} \cdot \mathbf{u}_n \approx \mathbf{G} \cdot \mathbf{u}_n$ [50]. Equation (1.23) finally becomes

$$E(\mathbf{Q}) = \sum_{\mathbf{G}} \int d\mathbf{r} \cdot F(\mathbf{Q}) \Omega(\mathbf{r}) \exp[i\mathbf{G}\mathbf{u}(\mathbf{r})] \exp(i\mathbf{q}\mathbf{r}) \quad (1.24)$$

where $\mathbf{q} = \mathbf{Q} - \mathbf{G}$ is the reduced scattering vector.

For the reflection with reciprocal lattice vector $\mathbf{G} = \mathbf{h}$, the diffracted intensity is $I(\mathbf{Q}) = E(\mathbf{Q}) \times E(\mathbf{Q})^*$. From the amplitude equation (1.24), assuming that the structure factor is independent on \mathbf{r} we obtain

$$I(\mathbf{Q}) = |F(\mathbf{Q})|^2 \int d\mathbf{r} \cdot \int d\Delta\mathbf{r} \cdot \Omega(\mathbf{r}) \Omega(\mathbf{r} + \Delta\mathbf{r}) \exp[i\mathbf{h}\{\mathbf{u}(\mathbf{r} + \Delta\mathbf{r}) - \mathbf{u}(\mathbf{r})\}] \exp(i\mathbf{q}\Delta\mathbf{r}) \quad (1.25)$$

Let us assume that at any position in the solid \mathbf{r} , the function $\mathbf{u}(\mathbf{r} + \Delta\mathbf{r}) - \mathbf{u}(\mathbf{r})$ remains statistically unchanged and depends only on the correlation vector $\Delta\mathbf{r}$. In that case, the choice of a particular origin for the position vector \mathbf{r} is unimportant and this term can be averaged over all defect configurations. With this assumption, we can separate the diffraction effects due to crystallite size and shape (Ω) with those due to defects (\mathbf{u}). The diffracted intensity close to the reciprocal lattice point with vector \mathbf{h} will now become

$$I(\mathbf{Q}) = |F(\mathbf{Q})|^2 \int d\Delta\mathbf{r} \cdot V(\Delta\mathbf{r}) G(\Delta\mathbf{r}) \exp(i\mathbf{q}\Delta\mathbf{r}) \quad (1.26)$$



with

$$G(\Delta\mathbf{r}) = \langle \exp\{i\mathbf{h}[\mathbf{u}(\Delta\mathbf{r}) - \mathbf{u}(0)]\} \rangle \quad (1.27)$$

and

$$V(\Delta\mathbf{r}) = \Omega(\Delta\mathbf{r}) * \Omega(-\Delta\mathbf{r}) = \int d\mathbf{r} \cdot \Omega(\Delta\mathbf{r})\Omega(\mathbf{r} + \Delta\mathbf{r}) \quad (1.28)$$

From this equation, we can see that the diffraction intensity is the Fourier transform of the product of two terms: the correlation volume $V(\Delta\mathbf{r})$ and the pair correlation function $G(\Delta\mathbf{r})$. While the former is solely dependent on the size and shape of the crystallites building up the solid, the latter depends only on the lattice displacements induced by the presence of structural defects. The evaluation of $V(\Delta\mathbf{r})$ is easier compared to $G(\Delta\mathbf{r})$ as it only relies on geometrical considerations.

$V(\Delta\mathbf{r})$ gives rise to well-known features such as truncation rods in case of surfaces, interference (Laue) fringes in thin crystals and peak broadening. The effects of $G(\Delta\mathbf{r})$ are more complex and will be detailed in the next section.

1.11 DIFFUSE SCATTERING OF X-RAYS BY CRYSTAL DEFECTS

X-ray diffraction methods allow the investigation of various crystal defects, *i.e.*, defect sizes ranging from the atomic level up to large dislocation loops that are well above the visibility limit of the transmission electron microscope. The diffuse X-ray scattering distribution from a defective crystal is the weak part of the scattering between Bragg peaks which arises from the strain field in the lattice surrounding the defects. In recent times, the analysis of diffuse scattering has become an essential tool for the understanding the structures of many technologically important materials such as alloys [51], shape-memory alloys [52], ferroelectrics [53], superconductors [54] and semiconductors [55] and also protein motions [56]. Many studies and reviews have explored the diffuse scattering from various defects that can be present in crystalline material [57] [58] [59] [60] [61], *e.g.* point defects [62] [63] [64], dislocations [57] [65] [66], stacking faults [67], three-dimensional defects clusters [58] have all been previously studied in detail. A general theory of diffuse scattering in crystals containing randomly distributed defects with elastic fields of atomic displacements has been given by Krivoglaz [68]. We here briefly recall this theory.

The amplitude scattered from a crystal with defects can be written using (1.17) and intensity, the displacement vector \mathbf{u} and the shape function

$$E = \sum_n \Omega_n F_n \exp(i\mathbf{Q} \cdot \mathbf{u}_n) \exp(i\mathbf{Q} \cdot \mathbf{r}_n) \quad (1.29)$$

$$I = \sum_{n,n'} \Omega_n \Omega_{n'} \langle F_n F_{n'}^* \exp[i\mathbf{Q}(\mathbf{u}_n - \mathbf{u}_{n'})] \rangle \exp[i\mathbf{Q}(\mathbf{r}_n - \mathbf{r}_{n'})] \quad (1.30)$$



from which we can write

$$V_{n,n'} = \Omega_n \Omega_{n'}, \quad G_{n,n'} = \langle F_n F_{n'}^* \exp[i\mathbf{Q}(\mathbf{u}_n - \mathbf{u}_{n'})] \rangle \quad (1.31)$$

The averaging, denoted by the angle brackets, is performed over the statistical ensemble mentioned above. $V_{n,n'}$ and $G_{n,n'}$ are the terms similar to equation (1.26) but now includes F . First, we encounter a variation of the structure factor F_n caused by the fact that the sites of the type s are occupied by atoms of different species. A second perturbing factor is due to displacements \mathbf{u} of atoms from the lattice sites. While the variations of F_n are typically localized in space sharply enough, the violations of perfection caused by atom displacements may involve small or large regions in the crystal, depending on the type. For the sake of simplicity we assume that the defect concentration is low, *i.e.*, the number of defects is considerably smaller than the number of sites they can occupy. This restriction clearly does not reduce the generality of the qualitative results obtained in this way. But since the regions of significant distortions produced by individual defects can be large and overlap with each other, even when the defect concentration is small, significant distortions can occur not only in individual regions but throughout the crystal.

Krivoglaz [68] considered the displacement at site n as a result of the linear superposition of the displacement of all the defects in the crystal. Let c_t be the probability of having a defect in the site t , then

$$\mathbf{u}_n = \sum_t c_t \mathbf{u}_{n,t} \quad (1.32)$$

$\mathbf{u}_{n,t}$ is the displacement vector for the center of the n th lattice cell caused by the introduction of a defect to the position t . Here summation is performed over all positions t that can be occupied by a defect, *i.e.*, over all lattice sites in substitutional solutions, over interstices in interstitial solutions, over points in a given plane which can contain the dislocation line in the case of straight-line dislocations, and so on. When the defect concentration is low, the configurations with two or more defects near the given n th cell make a negligibly small contribution and we can use a similar approach and write the structure factor for the n th cell in the form

$$F_n = F + \sum_t c_t \phi_{n,t} \quad (1.33)$$

where F is the structure factor for the crystal without defects and $\phi_{n,t}$ is the change in the structure amplitude with the introduction of the defect. If we substitute (1.32) and (1.33) into the equation (1.30), we obtain the equation for the scattering intensity corresponding to the given defect distribution in the crystal, *i.e.*, the given numbers c_t

$$I = \sum_{n,n'} V_{n,n'} \left(F + \sum_t c_t \phi_{n,t} \right) \left(F^* + \sum_{t'} c_{t'} \phi_{n',t'}^* \right) e^{i\mathbf{Q}(\mathbf{r}_n - \mathbf{r}_{n'})} \prod_{t''} \exp[i\mathbf{Q}(\mathbf{u}_{n,t''} - \mathbf{u}_{n',t''}) c_{t''}] \quad (1.34)$$



The random numbers c_t are statistically independent in the case of a random distribution of defects considered here when the defect positions are not correlated. The numbers c_t can have two values, either the value is 1 with the probability c equal to the defect concentration and have 0 with the probability $1 - c$. Averaging over the random variables c_t , first in the case when defects do not affect the structure amplitudes ($\phi_{st} = 0$), the problem reduces to finding the average for the product of the statistically independent factor $\exp[i\mathbf{Q}(\mathbf{u}_{n,t} - \mathbf{u}_{n',t})c_t]$. When we average each factor over the numbers $c_t = 0, 1$, we obtain,

$$\langle \exp[i\mathbf{Q}(\mathbf{u}_{n,t} - \mathbf{u}_{n',t})c_t] \rangle = c \times \exp[i\mathbf{Q}(\mathbf{u}_{n,t} - \mathbf{u}_{n',t})c_t] + 1 - c \quad (1.35)$$

Then the average for the product in (1.34) can be written as

$$\prod_t [c \exp[i\mathbf{Q}(\mathbf{u}_{n,t} - \mathbf{u}_{n',t})] + 1 - c] = \exp \sum_t \ln[1 + c(\exp[i\mathbf{Q}(\mathbf{u}_{n,t} - \mathbf{u}_{n',t})] - 1)] = e^{-T} \quad (1.36)$$

The Bragg scattering originates from the average structure, which means that the order of long distance for which the correlation length $|\mathbf{r}_n - \mathbf{r}_{n'}|$ tend to infinity. The diffuse scattering is obtained by calculating the total intensity by subtracting the Bragg scattering. If we now include structure factor variations, we obtain

$$I_{diffuse}(\mathbf{Q}) = \sum_{n,n'} V_{n,n'} e^{i\mathbf{Q}(\mathbf{r}_n - \mathbf{r}_{n'})} e^{-2M} \left[\left(|\bar{F}|^2 + c \sum_t \phi_{n,t} \phi_{n',t}^* e^{i\mathbf{Q}(\mathbf{u}_{n,t} - \mathbf{u}_{n',t})} \right) e^{-(T - T_\infty)} - |\bar{F}|^2 \right] \quad (1.37)$$

and the Bragg scattering is

$$I_{Bragg} = \sum_{n,n'} V_{n,n'} \exp[i\mathbf{Q}(\mathbf{r}_n - \mathbf{r}_{n'})] e^{-2M} \quad (1.38)$$

T_∞ is the limiting value of T . $|\bar{F}|^2$ is the mean structure factor squared. The real part of T_∞ ($= 2M$) is responsible for the weakening of the diffracted intensity; *mutatis mutandis* with the thermal scattering, this term is called **static Debye-Waller factor**. The imaginary part of T_∞ gives rise to a displacement and an asymmetry of the peak, but there are no cases of widening of the peak.

The diffuse contribution is a continuous function, but generally concentrated around the Bragg position, such that it is often interpreted as the Bragg peak broadening. We should note that this distribution is equally enlarged by an effect of size since it is present in the form of a truncated Fourier series by the boundaries of the crystal ($V_{n,n'}$ term).

CLASSIFICATION OF DEFECTS

The above results make it possible to find out whether the defects under consideration produce broadening of the lines in the X-ray diffraction patterns. Various defects can be classified into two classes. The



real part of the T_∞ denoted as $2M$, can be written as

$$c \sum_s [1 - \cos(\mathbf{Q} \cdot \mathbf{u}_{ts})] \quad (1.39)$$

For the defects of the first class, M is finite. The introduction of defects leads to shifting of the lines, to changes in their integrated intensity caused by the variation of the averaged structure factor, to the emergence of the intensity weakening factor $\exp(-2M)$. The value of M for defects of the second class tends to infinity. The scattering intensity distribution becomes smooth and no lines and background can be identified even in the limiting case of the infinite crystal. It can be shown that for small defect concentrations these distributions have sharp narrow peaks in the vicinities of the reciprocal lattice points whose widths are proportional to the defect concentration. The resulting sharp peaks can be naturally referred to as the broadened regular reflections implying that the lines in the X-ray diffraction patterns are broadened owing to the introduction of defects into the crystal.

The convergence of the sum over s in the equation (1.39) is entirely determined by the convergence of $\int_{r>R_0} (\mathbf{Q} \cdot \mathbf{u}_{ts}) dV$. A defect will be of first class if $2M$ is finite (*i.e.*, if $\mathbf{u} \propto 1/r^n$, and $n \geq 2$). If $2M$ is infinite (*i.e.*, if $n \leq 3/2$) then it is said to be of second class. Hence, depending on the integral $\int_{r>R_0} (\mathbf{Q} \cdot \mathbf{u}_{ts}) dV$ converges or not, the defects belong to the first or second class, in accordance with the asymptotic behaviour of displacements at large distances from the defects. The displacements produced by point defects decrease asymptotically as the square of the increasing distance $\mathbf{u}_{st} \sim r^{-2}$. According to elasticity theory, the displacements also decrease as r^{-2} for a fairly general type of arbitrary bounded defects with finite dimensions along three axes at distances much larger than these dimensions. Therefore, all defects of such type belong to the first class and do not produce broadening of lines in the X-ray diffraction patterns. When the defect is an infinitely long cylinder of impurity atoms in the crystal, or for a point defect in a two-dimensional lattice, the resulting displacements decrease linearly with increasing distance. The integral clearly exhibits logarithmic divergence, suggesting that such defects belong to the second class. Dislocations with straight dislocation lines passing through the entire crystal can also be regarded as infinitely long defects. The displacements produced by them do not decrease with increasing distance from the dislocation line. Hence, the straight-line dislocations are defects of the second class and produce broadening of the X-ray lines. In a finite crystal, M obviously does not become infinite. But for dislocations or point defects in a linear chain, M is so large that $\exp(-2M)$ practically vanishes.

The above results show that X-ray line broadening is also caused by infinitely extended defects such as stacking faults randomly distributed in the crystal, or by systems of dislocations forming block boundaries in the infinite crystal. On the other hand, when the dislocation line is closed as it is in dislocation loops, the defect size is finite, $\mathbf{u}_{n,t}$ decreases as r^{-2} at large distances and according to the above classification, instead of line broadening, weakening of the line intensity must take place. A similar qualitative analysis can be applied to the diffraction effects caused by any crystal defects. The defects belong to the first or second class if defect dimensions are finite or infinite in one or two directions.



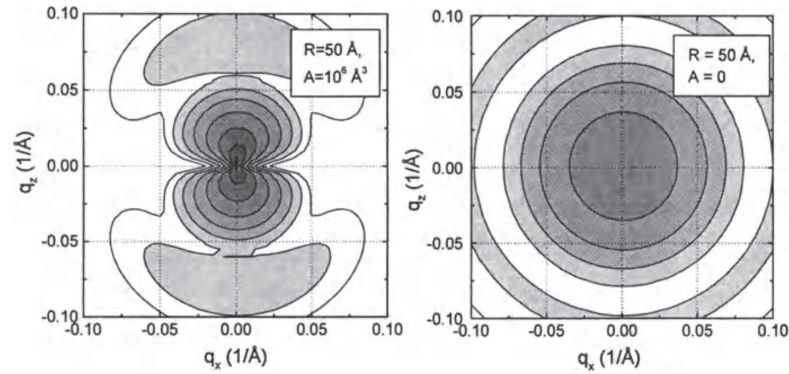


Figure 1.11.1: Reciprocal space distribution calculated for spherical defects of various strengths. (a) Pure Huang scattering shows the double-looped form of the intensity maximum and (b) typical diffuse scattering from a zero defect strength defect [69].

As stated above, defects of finite size in an infinite crystal matrix are weak. If we look into the detail of the reciprocal space map obtained from a crystal with defect, we can typically notice two parts (i) the defect core, in which the structure differs substantially from the crystal structure of the surrounding matrix and (ii) the deformed area of the surrounding crystal matrix. If we investigate the reciprocal space distribution of the diffusely scattered intensity close to the reciprocal lattice point corresponding to the averaged lattice (*i.e.*, for small values of $|\mathbf{q}|$), the influence of the defect core can be neglected and the diffuse scattering is caused mainly by the elastic deformation of the surrounding crystal. This is called Huang scattering. The pure Huang scattering shows the double-looped form of the intensity maximum as given in figure (1.11.1) which is typical of defects with r^{-2} displacement fields.

1.12 DYNAMICAL THEORY OF DIFFRACTION

1.12.1 HISTORICAL BACKGROUND

The early development of dynamical theory originated back to Darwin's work [70][71] in which he introduced the scheme of multiple reflections over parallel planes. He obtained the correct form for the total reflected intensity from perfect crystals and predicted the phenomena of primary extinction. An improved dynamical theory was proposed by Ewald, later reformulated by von Laue [72] [73]. Ewald's theory [74] [75] [76] formed the backbone to the classical dynamical diffraction theory. Different from the geometrical (kinematical) theory, the classical dynamical theory is based on the wave equation derived from Maxwell's electromagnetic equations. Due to the periodicity of the crystal, the susceptibility of the crystal is periodic too, resulting in a Bloch wave solution to the wave equation. In general, the Bloch wave involves an infinite number of plane waves and their amplitudes cannot be solved exactly [77].

Fortunately, in most cases for an incident plane wave, only the directly transmitted wave (o-wave) and diffracted wave(h-wave) with right Bragg condition have significant amplitudes. As a result the wave equation can be reduced to two coupled algebraic equations and the exact solution can be found. This is widely used as a two-beam approximation. The classical theory succeeds in prediction and explanation of many dynamical diffraction phenomena, such as the Bragg intensities from perfect single crystals, extinction effect, total reflection, anomalous transmission (Borrmann effect), pendellosung fringes, double-refraction and double-reflection, which cannot be understood by application of kinematical theory.

1.12.2 TAKAGI-TAUPIN EQUATIONS

Though the classical Ewald-von Laue theory describes a clear picture of the physics of X-ray dynamical diffraction in perfect crystals, the integral form of its fundamental equations imposes a limitation hard to overcome when dealing with imperfect crystals. A lot of efforts have been devoted to solving the problem of dynamical diffraction in imperfect crystals and many theories have been developed. Although initially not restricted to layered materials, a theory developed by Takagi and Taupin[78] [79] [80] found huge success in the analyses of strained layered materials. The Takagi-Taupin equations are also based on the wave equation derived from Maxwell's equations. In this theory, the wave propagating within a crystal is assumed to be a modulated wave with slowly varying amplitude, instead of plane waves with constant wave amplitudes as in the classical theory. In the following we give a short overview of the theory underlying the Takagi-Taupin equations.

The polarizability of a deformed crystal is previously given in the form of equation (1.16). Assuming Takagi approximation, the polarizability now becomes

$$\chi(\mathbf{r}) = \sum_g \chi_g \exp[i\mathbf{g} \cdot \{\mathbf{r} - \mathbf{u}(\mathbf{r})\}] = -\frac{r_e \lambda^2}{\pi V} F(\mathbf{r}) \quad (1.40)$$

where $F(\mathbf{r})$ is the structure factor, r_e is the classical electron radius, V is the volume of the unit cell. Since the deformation field $\mathbf{u}(\mathbf{r})$ violates the exact periodicity of the polarizability, the solution of the wave equation cannot be found in the form of a Bloch wave. But since the first derivatives of $\mathbf{u}(\mathbf{r})$ are small within the Takagi approximation, the solution of the wave equation for a slightly deformed crystal will not be very different from a Bloch wave. The modified Bloch wave form in the two beam case for the wavefield $\mathbf{D}(\mathbf{r})$ inside the crystal is

$$\mathbf{D}(\mathbf{r}) = \mathbf{D}'_0(\mathbf{r})e^{i\mathbf{K}_0 \cdot \mathbf{r}} + \mathbf{D}'_H(\mathbf{r})e^{i\mathbf{K}'_H \cdot \mathbf{r}} \quad (1.41)$$



In the modified Bloch wave, the coefficients $\mathbf{D}'_{0,H}$ are unknown functions of the position \mathbf{r} . The wave vectors of the components of the modified Bloch wave is equal to the sum of the wave vector of the incident vacuum wave \mathbf{K}_0 and of the wave vector

$$\mathbf{K}'_H = \mathbf{K}_0 + \mathbf{H}', \quad \mathbf{H}' = \mathbf{H} - \nabla\psi_H \quad (1.42)$$

which is affected by the deformation field in the crystal included in the term $\psi_H = \mathbf{H} \cdot \mathbf{u}(\mathbf{r})$. Here the choice of the wave vectors of these components is arbitrary and the sole requirement is that the functions $\mathbf{D}'_0(\mathbf{r})$ and $\mathbf{D}'_H(\mathbf{r})$ must be nearly constant within the elementary unit cell. In this case, we assume that $\psi_H(\mathbf{r})$ is a function of the coordinate z perpendicular to the sample surface. Therefore, the amplitudes \mathbf{D}'_0 and \mathbf{D}'_H are functions of z only. Introducing the complex diffractivity of the crystal at depth z is

$$R(z) = \frac{D_H}{D_0} \quad (1.43)$$

Now, equipped with these equations and assumptions, the Takagi-Taupin equation for the complex diffractivity gives

$$\frac{\partial R}{\partial z} = -\frac{iK P\psi_H}{2 \gamma_0} R^2 + i\kappa'(z)R + \frac{iK P\psi_H}{2 \gamma_H} \quad (1.44)$$

where

$$\kappa'(z) = \kappa + \frac{K\psi_0}{2\gamma_H} \left(1 - \frac{\gamma_H}{\gamma_0}\right) + \frac{d\psi_H(z)}{dz}, \quad \kappa = K_{Hz} - K'_{Hz} \quad (1.45)$$

Here K'_{Hz} is the modified Bloch wave vector component which is the sum of wave vector of incident vacuum wave K_0 and of the wave vector H , and,

$$\gamma_H = \mathbf{n} \cdot \mathbf{k} = -\sin(\theta_B + \phi) \quad (1.46)$$

$$\gamma_0 = \mathbf{n} \cdot \mathbf{k} = \sin(\theta_B - \phi) \quad (1.47)$$

are the direction cosines of the reflected and the incident beams with respect to the crystal surface normal, \mathbf{n} is the vector normal to surface, \mathbf{k} is the wave vector.

The boundary condition for $R(z)$ for the Bragg geometry and for a crystal with parallel surfaces, with thickness t is given by

$$R(-t) = 0 \quad (1.48)$$

since there is no diffracted wave at the rear surface of the crystal. In the Laue geometry, $R(0) = 0$ is valid instead. In the case of a layer or layered system of thickness t deposited on a substrate, the boundary condition at the layer-substrate interface is simply

$$R(-t) = R_{sub} \quad (1.49)$$



1.12.3 RECURSION FORMULAE FOR THE TAKAGI - TAUPIN EQUATIONS

The Takagi-Taupin equation defined in (1.44) can be rewritten as a function of

$$X = \left(\frac{F_{\bar{H}}}{F_H} \right)^{1/2} \left| \frac{\gamma_H}{\gamma_0} \right|^{1/2} R(z) \quad (1.50)$$

to become

$$-idX/dT = X^2 - 2\eta X + 1 \quad (1.51)$$

where η and T are complex quantities given by

$$\eta = \frac{-b(\theta - \theta_B) \sin 2\theta_B - \frac{1}{2}\Gamma F_0(1 - b)}{|b|^{1/2} P\Gamma(F_H F_{\bar{H}})^{1/2}} \quad (1.52)$$

$$T = \frac{\pi P\Gamma(F_H F_{\bar{H}})^{1/2} t}{\lambda |\gamma_0 \gamma_H|^{1/2}} \quad (1.53)$$

where

$$\Gamma = r_e \lambda^2 / \pi V, r_e = e^2 / 4\pi \epsilon_0 m c^2, b = \gamma_0 / \gamma_H \quad (1.54)$$

T is determined by the crystal thickness t and the structure factor ($F_H = F'_H + iF''_H$) of the reflection. The departure from the Bragg angle θ_B determines the deviation parameter η . The second part of the numerator of η corresponds to the refraction and absorption of X-rays. In the Bragg case, the direction cosines γ_0 and γ_H of the incident and the diffracted beam with respect to the surface normal are opposite in sign so that the asymmetry factor b is negative. The classical electron radius r_e is equal to $2.818 \times 10^{-5} \text{ \AA}$, λ is the X-ray wavelength and V is the volume of the unit cell. The differential equation can be solved for layers of constant η and arbitrary thickness. This solution can also be used for sections for which η can be considered to be constant. The following recursion equation [81] gives the relation between the amplitude ratio X_0 at the bottom of the layer and X_t at its top:

$$X_t = \eta + \sqrt{\eta^2 - 1} \frac{S_1 + S_2}{S_1 - S_2} \quad (1.55)$$

where

$$S_1 = [X_0 - \eta + \sqrt{\eta^2 - 1}] \exp[-iT\sqrt{\eta^2 - 1}] \quad (1.56)$$

$$S_2 = [X_0 - \eta - \sqrt{\eta^2 - 1}] \exp[iT\sqrt{\eta^2 - 1}] \quad (1.57)$$

and

$$X_0 = X_{t \rightarrow \infty} = \eta \pm \sqrt{\eta^2 - 1} \quad (1.58)$$



The reflectivity of a strained layer is calculated starting from the Darwin formulae (1.58) for the substrate and adding strained layer by strained layer, using the recursion formulae (1.55) until the last layer is achieved. Finally, the reflectivity is given by :

$$R_H = \left(\frac{\gamma_H}{\gamma_0} \right) \left| \frac{D_H}{D_0} \right|^2 = \left(\frac{\psi_H}{\psi_{\bar{H}}} \right) |X|^2 \quad (1.59)$$

1.13 CONCLUSION

The first part of this chapter presented the literature survey on the ion/solid interaction concepts and application to the cubic zirconia. Ion beams, having numerous applications in various fields of materials science, is a very useful technique to study the properties of a material. The interaction of the ion beams with matter leads to the creation of defects in the target material. Depending on the energy of the incident particle, the interaction can be divided into elastic and inelastic interactions. YSZ is a promising material to be used as an inert matrix for the transmutation of radiotoxic actinides. Previous studies on the YSZ has proven that the material has high chemical stability and radiation resistance. The complete understanding of its behaviour requires a detailed analysis of the evolution of its microstructure under various irradiation, a task which can be conducted, partly, using XRD. The second part of the chapter dealt with the theory of X-ray diffraction. XRD is an attractive technique to study irradiated materials since it is a non-destructive technique, requires no sample preparation and a statistically relevant method. In order to explain the X-ray diffraction phenomena in crystals, two general diffraction theories were proposed: kinematical and dynamical theory. In the kinematical theory, the transmitted X-rays suffer only normal linear absorption and the waves undergo a single scattering. In the dynamical theory of diffraction, multiple scattering processes are taken into account. Takagi-Taupin equations, based on the wave equation derived from Maxwell's equations are used to describe the dynamical theory of diffraction. X-ray diffraction technique allows the investigation of various crystal defects such as point defects, dislocation loops, stacking faults *etc.* The diffuse X-ray scattering investigation can give valuable information regarding the type of defects, their positions in the crystal lattice, their concentrations and the static displacement fields around them. In the next chapter, all the experimental techniques and computational tools required to conduct a comprehensive study on the effect of the irradiation temperature and fluence on the behaviour of cubic zirconia is presented.



REFERENCES

- [1] J. Mayer and S. Lau, “Electronic materials science: For integrated circuits in Si and GaAs,” 1990.
- [2] L. Rubin and W. Morris, “High-energy ion implanters and applications take off,” *Semiconductor international*, vol. 20, no. 4, pp. 77–88, 1997.
- [3] J. F. Ziegler, *Ion Implantation Science and Technology 2e*. Elsevier, 2012.
- [4] G. Dearnaley, *Ion implantation*, vol. 8. North-Holland Publishing Company, 1973.
- [5] R. Baskar, K. A. Lee, R. Yeo, and K.-W. Yeoh, “Cancer and radiation therapy: current advances and future directions,” *International journal of medical sciences*, vol. 9, no. 3, p. 193, 2012.
- [6] T. Haberer, M. Kraemer, G. Kraft, W. Kraft-Weyrather, D. Schardt, M. Scholz, U. Weber, A. Dolinski, H. Eickhoff, B. Franczak, *et al.*, “Ion beam therapy system and a method for operating the system,” Jan. 27 2004. US Patent 6,683,318.
- [7] W. J. Weber, R. C. Ewing, C. Catlow, T. D. De La Rubia, L. Hobbs, C. Kinoshita, H. Matzke, A. Motta, M. Nastasi, E. Salje, *et al.*, “Radiation effects in crystalline ceramics for the immobilization of high-level nuclear waste and plutonium,” *Journal of Materials Research*, vol. 13, no. 06, pp. 1434–1484, 1998.
- [8] T. Shimizu-Iwayama, N. Kurumado, D. E. Hole, and P. D. Townsend, “Optical properties of silicon nanoclusters fabricated by ion implantation,” *Journal of applied physics*, vol. 83, no. 11, pp. 6018–6022, 1998.
- [9] W. Mickelson, S. Aloni, W.-Q. Han, J. Cumings, and A. Zettl, “Packing C60 in boron nitride nanotubes,” *Science*, vol. 300, no. 5618, pp. 467–469, 2003.
- [10] A. Krashennnikov and K. Nordlund, “Ion and electron irradiation-induced effects in nanostructured materials,” *Journal of applied physics*, vol. 107, no. 7, p. 071301, 2010.
- [11] B. Peng, M. Locascio, P. Zapol, S. Li, S. L. Mielke, G. C. Schatz, and H. D. Espinosa, “Measurements of near-ultimate strength for multiwalled carbon nanotubes and irradiation-induced crosslinking improvements,” *Nature nanotechnology*, vol. 3, no. 10, pp. 626–631, 2008.
- [12] M. Raghuveer, P. Ganesan, J. D’Arcy-Gall, G. Ramanath, M. Marshall, and I. Petrov, “Nanomachining carbon nanotubes with ion beams,” *Applied physics letters*, vol. 84, no. 22, pp. 4484–4486, 2004.



- [13] R. Caudillo, H. Troiani, M. Miki-Yoshida, M. Marques, A. Rubio, and M. Yacaman, "A viable way to tailor carbon nanomaterials by irradiation-induced transformations," *Radiation Physics and Chemistry*, vol. 73, no. 6, pp. 334–339, 2005.
- [14] C. Gómez-Navarro, P. De Pablo, J. Gómez-Herrero, B. Biel, F. Garcia-Vidal, A. Rubio, and F. Flores, "Tuning the conductance of single-walled carbon nanotubes by ion irradiation in the anderson localization regime," *Nature Materials*, vol. 4, no. 7, pp. 534–539, 2005.
- [15] A. Hashimoto, K. Suenaga, A. Gloter, K. Urita, and S. Iijima, "Direct evidence for atomic defects in graphene layers," *Nature*, vol. 430, no. 7002, pp. 870–873, 2004.
- [16] J. F. Ziegler and J. P. Biersack, "The stopping and range of ions in matter," in *Treatise on Heavy-Ion Science*, pp. 93–129, Springer, 1985.
- [17] G. Kinchin and R. Pease, "The displacement of atoms in solids by radiation," *Reports on progress in physics*, vol. 18, no. 1, p. 1, 1955.
- [18] E. H. Kisi and C. Howard, "Crystal structures of zirconia phases and their inter-relation," *Key Engineering Materials*, vol. 153, pp. 1–36, 1998.
- [19] J. B. Goodenough and Y.-H. Huang, "Alternative anode materials for solid oxide fuel cells," *Journal of Power Sources*, vol. 173, no. 1, pp. 1–10, 2007.
- [20] N. P. Padture, M. Gell, and E. H. Jordan, "Thermal barrier coatings for gas-turbine engine applications," *Science*, vol. 296, no. 5566, pp. 280–284, 2002.
- [21] T. Thome, D. Braga, and G. Blaise, "Effect of current density on electron beam induced charging in sapphire and yttria-stabilized zirconia," *Journal of applied physics*, vol. 95, no. 5, pp. 2619–2624, 2004.
- [22] A. Boughariou, A. Kallel, and G. Blaise, "Experimental study of charging kinetics in yttria stabilized zirconia," *Physica B: Condensed Matter*, vol. 442, pp. 90–94, 2014.
- [23] R. C. Ewing, W. J. Weber, and J. Lian, "Nuclear waste disposal—pyrochlore (a2b2o7): Nuclear waste form for the immobilization of plutonium and "minor" actinides," *Journal of Applied Physics*, vol. 95, no. 11, pp. 5949–5971, 2004.
- [24] C. Degueldre, "Zirconia inert matrix for plutonium utilisation and minor actinides disposition in reactors," *Journal of Alloys and Compounds*, vol. 444, pp. 36–41, 2007.
- [25] Y.-W. Lee, C. Y. Joung, S. H. Kim, and S.-C. Lee, "Inert matrix fuel—a new challenge for material technology in the nuclear fuel cycle," *Metals and Materials International*, vol. 7, no. 2, pp. 159–164, 2001.



- [26] C. Degueudre and J. Paratte, "Concepts for an inert matrix fuel, an overview," *Journal of Nuclear Materials*, vol. 274, no. 1, pp. 1–6, 1999.
- [27] K. E. Sickafus, H. Matzke, T. Hartmann, K. Yasuda, J. A. Valdez, P. Chodak III, M. Nastasi, and R. A. Verrall, "Radiation damage effects in zirconia," *Journal of Nuclear Materials*, vol. 274, no. 1, pp. 66–77, 1999.
- [28] V. Oversby, C. McPheeters, C. Degueudre, and J. Paratte, "Control of civilian plutonium inventories using burning in a non-fertile fuel," *Journal of nuclear materials*, vol. 245, no. 1, pp. 17–26, 1997.
- [29] W. Gong, W. Lutze, and R. Ewing, "Zirconia ceramics for excess weapons plutonium waste," *Journal of Nuclear Materials*, vol. 277, no. 2, pp. 239–249, 2000.
- [30] R. B. Heimann and T. Vandergraaf, "Cubic zirconia as a candidate waste form for actinides: dissolution studies," *Journal of materials science letters*, vol. 7, no. 6, pp. 583–586, 1988.
- [31] T. Hojo, H. Yamamoto, J. Aihara, S. Furuno, K. Sawa, T. Sakuma, and K. Hojou, "Loop formation by ion irradiation in yttria stabilized zirconia," *Nuclear Instruments and Methods in Physics Research Section B: Beam Interactions with Materials and Atoms*, vol. 250, no. 1, pp. 101–105, 2006.
- [32] F. Garrido, L. Vincent, L. Nowicki, G. Sattonnay, and L. Thomé, "Radiation stability of fluorite-type nuclear oxides," *Nuclear Instruments and Methods in Physics Research Section B: Beam Interactions with Materials and Atoms*, vol. 266, no. 12, pp. 2842–2847, 2008.
- [33] G. Velisa, A. Debelle, L. Vincent, L. Thomé, D. Pantelica, and A. Declémy, "Study of the structural modifications induced by the implantation in cubic zirconia," *Nuclear Instruments and Methods in Physics Research Section B: Beam Interactions with Materials and Atoms*, vol. 268, no. 19, pp. 2984–2986, 2010.
- [34] S. Moll, L. Thomé, G. Sattonnay, A. Debelle, F. Garrido, L. Vincent, and J. Jagielski, "Multistep damage evolution process in cubic zirconia irradiated with MeV ions," *Journal of Applied Physics*, vol. 106, no. 7, p. 073509, 2009.
- [35] S. Moll, L. Thome, G. Sattonnay, F. Garrido, L. Vincent, J. Jagielski, and T. Thome, "Microstructural evolution of cubic zirconia irradiated with swift heavy ions," *Vacuum*, vol. 83, pp. S61–S64, 2009.
- [36] K. E. Sickafus, H. Matzke, K. Yasuda, P. Chodak III, R. A. Verrall, P. G. Lucuta, H. R. Andrews, A. Turos, R. Fromknecht, and N. P. Baker, "Radiation damage effects in cubic-stabilized zirconia irradiated with 72 mev I+ ions," *Nuclear Instruments and Methods in Physics Research Section B: Beam Interactions with Materials and Atoms*, vol. 141, no. 1, pp. 358–365, 1998.



- [37] I. Afanasyev-Charkin and K. Sickafus, "Effect of sputtering in Xe ion irradiated yttria-stabilized zirconia," *Journal of nuclear materials*, vol. 306, no. 2, pp. 112–120, 2002.
- [38] N. Yu, K. E. Sickafus, P. Kodali, and M. Nastasi, "In situ observation of defect growth beyond the irradiated region in yttria-stabilized zirconia induced by 400 keV xenon ion-beam at 90 and 30° C," *Journal of nuclear materials*, vol. 244, no. 3, pp. 266–272, 1997.
- [39] L. Wang, S. Wang, and R. Ewing, "Amorphization of cubic zirconia by caesium-ion implantation," *Philosophical Magazine Letters*, vol. 80, no. 5, pp. 341–347, 2000.
- [40] L. Wang, S. Wang, S. Zhu, and R. Ewing, "Effects of fission product incorporation on the microstructure of cubic zirconia," *Journal of nuclear materials*, vol. 289, no. 1, pp. 122–127, 2001.
- [41] K. Yasuda, C. Kinoshita, S. Matsumura, and A. Ryazanov, "Radiation-induced defect clusters in fully stabilized zirconia irradiated with ions and/or electrons," *Journal of nuclear materials*, vol. 319, pp. 74–80, 2003.
- [42] L. Thomé, J. Fradin, J. Jagielski, A. Gentils, S. Enescu, and F. Garrido, "Radiation damage in ion-irradiated yttria-stabilized cubic zirconia single crystals," *The European Physical Journal Applied Physics*, vol. 24, no. 01, pp. 37–48, 2003.
- [43] J. Jagielski and L. Thomé, "Multi-step damage accumulation in irradiated crystals," *Applied Physics A*, vol. 97, no. 1, pp. 147–155, 2009.
- [44] J.-M. Costantini, F. Beuneu, D. Gourier, C. Trautmann, G. Calas, and M. Toulemonde, "Colour centre production in yttria-stabilized zirconia by swift charged particle irradiations," *Journal of Physics: Condensed Matter*, vol. 16, no. 23, p. 3957, 2004.
- [45] J. Jagielski and L. Thomé, "Damage accumulation in ion-irradiated ceramics," *Vacuum*, vol. 81, no. 10, pp. 1352–1356, 2007.
- [46] J. Jagielski and L. Thomé, "Discontinuous character of the damage build-up in the elastic collision regime," *Radiation Effects & Defects in Solids*, vol. 166, no. 5, pp. 367–372, 2011.
- [47] S. Moll, L. Thomé, F. Garrido, L. Vincent, G. Sattonnay, J. Costantini, J. Jagielski, A. Benyagoub, and M. Behar, "Radiation effects in yttria-stabilized zirconia: Comparison between nuclear and electronic processes," *Nuclear Instruments and Methods in Physics Research Section B: Beam Interactions with Materials and Atoms*, vol. 266, no. 12, pp. 3048–3051, 2008.
- [48] T. Akashi, Y. Takahashi, T. Tanigaki, T. Shimakura, T. Kawasaki, T. Furutsu, H. Shinada, H. Muller, M. Haider, N. Osakabe, and A. Tonomura, "Aberration corrected 1.2-MV cold field-emission transmission electron microscope with a sub-50-pm resolution," *Applied Physics Letters*, vol. 106, no. 7, 2015.



- [49] P. F. Fewster, "X-ray analysis of thin films and multilayers," *Reports on Progress in Physics*, vol. 59, no. 11, p. 1339, 1996.
- [50] E. J. Mittemeijer and U. Welzel, *Modern diffraction methods*. John Wiley & Sons, 2013.
- [51] W. Schweika, *Disordered alloys: diffuse scattering and Monte Carlo simulations*. No. 141, Springer Science & Business Media, 1998.
- [52] T. Yamamoto, M.-S. Choi, S. Majima, T. Fukuda, and T. Kakeshita, "Origin of diffuse scattering appearing in iron-doped ti-ni shape memory alloys," *The European Physical Journal Special Topics*, vol. 158, no. 1, pp. 1–5, 2008.
- [53] M. Paściak, T. Welberry, J. Kulda, M. Kempa, and J. Hlinka, "Polar nanoregions and diffuse scattering in the relaxor ferroelectric $\text{PbMg}_{1/3}\text{Nb}_{2/3}\text{O}_3$," *Physical Review B*, vol. 85, no. 22, p. 224109, 2012.
- [54] M. Izquierdo, S. Megtert, J. Albouy, J. Avila, M. Valbuena, G. Gu, J. Abell, G. Yang, M. Asensio, and R. Comes, "X-ray diffuse scattering experiments from bismuth-based high- T_c superconductors," *Physical Review B*, vol. 74, no. 5, p. 054512, 2006.
- [55] M. Barchuk, V. Holý, B. Miljević, B. Krause, T. Baumbach, J. Hertkorn, and F. Scholz, "X-ray diffuse scattering from threading dislocations in epitaxial GaN layers," *Journal of Applied Physics*, vol. 108, no. 4, p. 043521, 2010.
- [56] M. E. Wall, P. D. Adams, J. S. Fraser, and N. K. Sauter, "Diffuse x-ray scattering to model protein motions," *Structure*, vol. 22, no. 2, pp. 182 – 184, 2014.
- [57] B. C. Larson and W. Schmatz, "Huang diffuse scattering from dislocation loops and cobalt precipitates in copper," *Physical Review B*, vol. 10, no. 6, p. 2307, 1974.
- [58] P. Dederichs, "Diffuse scattering from defect clusters near bragg reflections," *Physical Review B*, vol. 4, no. 4, p. 1041, 1971.
- [59] V. Punegov, "X-ray diffuse scattering from spherically symmetric clusters: The effect of defect size fluctuations," *Crystallography Reports*, vol. 54, no. 3, pp. 391–398, 2009.
- [60] W. A. Wooster, *Diffuse X-ray reflections from crystals*. Courier Corporation, 1997.
- [61] M. Schmidbauer, M. Hanke, and R. Köhler, "X-ray diffuse scattering on self-organized mesoscopic structures," *Crystal Research and Technology*, vol. 37, no. 1, pp. 3–34, 2002.
- [62] P. Dederichs, "The theory of diffuse x-ray scattering and its application to the study of point defects and their clusters," *Journal of Physics F: Metal Physics*, vol. 3, no. 2, p. 471, 1973.



- [63] H. Trinkaus, "On determination of the double-force tensor of point defects in cubic crystals by diffuse x-ray scattering," *physica status solidi (b)*, vol. 51, no. 1, pp. 307–319, 1972.
- [64] E. Segura and P. Ehrhart, "Interstitials and their agglomerates in electron irradiated gold investigated by diffuse x-ray scattering," *Radiation Effects*, vol. 42, no. 3-4, pp. 233–247, 1979.
- [65] H. Trinkaus, "On the investigation of small dislocation loops in cubic crystals by diffuse x-ray scattering," *physica status solidi (b)*, vol. 54, no. 1, pp. 209–218, 1972.
- [66] P. Ehrhart, H. Trinkaus, and B. Larson, "Diffuse scattering from dislocation loops," *Physical Review B*, vol. 25, no. 2, p. 834, 1982.
- [67] T. Welberry, "Diffuse x-ray scattering and models of disorder," *Reports on Progress in Physics*, vol. 48, no. 11, p. 1543, 1985.
- [68] M. A. Krivoglaz, *X-ray and neutron diffraction in nonideal crystals*. Springer, 1996.
- [69] V. Holy, T. Baumbach, and U. Pietsch, *High-resolution X-ray scattering from thin films and multilayers*. Springer, 1999.
- [70] C. G. Darwin, "LXXVIII. the theory of x-ray reflexion. part ii," *The London, Edinburgh, and Dublin Philosophical Magazine and Journal of Science*, vol. 27, no. 160, pp. 675–690, 1914.
- [71] R. James, "The dynamical theory of x-ray diffraction," *Solid State Physics*, vol. 15, pp. 53–220, 1963.
- [72] M. v. Laue *Ergebn. Exakten Naturwiss*, vol. 10, p. 133, 1931.
- [73] M. v. Laue, "The diffraction of an electron-wave at a single layer of atoms," *Physical Review*, vol. 37, no. 1, p. 53, 1931.
- [74] P. P. Ewald, "Zur begründung der kristallogoptik," *Annalen der Physik*, vol. 354, no. 1, pp. 1–38, 1916.
- [75] P. Ewald, "Zur begründung der kristallogoptik," *Annalen der Physik*, vol. 359, no. 23, pp. 519–556, 1917.
- [76] P. Ewald, "A review of my papers on crystal optics 1912 to 1968," *Acta Crystallographica Section A: Crystal Physics, Diffraction, Theoretical and General Crystallography*, vol. 35, no. 1, pp. 1–9, 1979.
- [77] S.-L. In-Hang, *Multiple Diffraction of X-rays in Crystals*, vol. 50. Springer Science & Business Media, 2012.
- [78] S. Takagi, "Dynamical theory of diffraction applicable to crystals with any kind of small distortion," *Acta Crystallographica*, vol. 15, no. 12, pp. 1311–1312, 1962.
- [79] S. Takagi, "A dynamical theory of diffraction for a distorted crystal," *Journal of the Physical Society of Japan*, vol. 26, no. 5, pp. 1239–1253, 1969.



- [80] D. Taupin, “Théorie dynamique de la diffraction des rayons x par les cristaux déformés,” *Bulletin De La Societe Francaise Mineralogie Et De Cristallographie*, vol. 87, no. 4, p. 469, 1964.
- [81] W. Bartels, J. Hornstra, and D. Lobeek, “X-ray diffraction of multilayers and superlattices,” *Acta Crystallographica Section A: Foundations of Crystallography*, vol. 42, no. 6, pp. 539–545, 1986.



2

Experimental and Computational Techniques

2.1 EXPERIMENTAL TECHNIQUES

2.1.1 ION BEAM ACCELERATOR

IN THIS STUDY, the samples are irradiated in a wide range of temperatures and fluences. The samples were irradiated with two different ion beam accelerators. Irradiations at low temperature (80 K) were conducted at the Tandetron of the Instituto de Física of the Universidade Federal of Rio Grande do Sul, Brazil. The accelerator is a 3 MV tandem from *High Voltage Co.* and is equipped with several beamlines, one of them being an implantation/irradiation line that can be used in a wide range of temperature, *i.e.*, from 80 K up to 1073 K. The rest of the irradiation experiments (*i.e.*, at RT, 573 K, 773 K and 1073 K) were performed at the JANNuS facility at CSNSM laboratory which is in Université Paris-Sud located in Orsay, France. The schematic representation of the JANNuS facility at Orsay is presented in Figure (2.1.1). The accelerator we used was a 2 MV Tandem, known-as ARAMIS, which is equipped with both an external negative ion source and a Penning source inside the chamber. Hence it is able to accelerate a large variety of ions including rare gases, transition metals, heavy metals (*Au* for example). Other particularities include energy range of 0.5-2 MV and the intensity range from 0.01 to 50 μA . The irradiation can be performed under the wide range of temperature from RT to 1073 K [1].

The crystals to be irradiated were placed on a special sample holder making a 7° tilting angle with respect

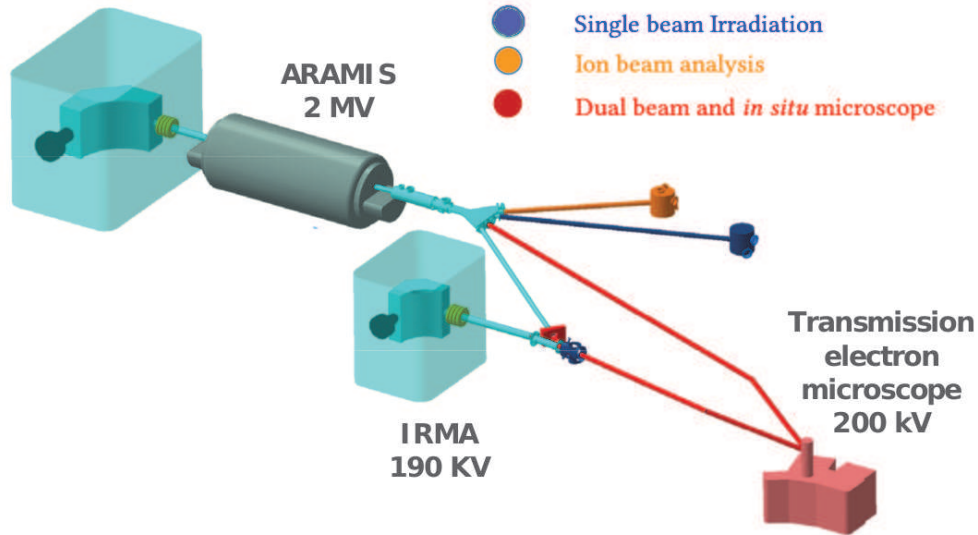


Figure 2.1.1: Schematic representation of the JANNuS facility at Orsay [1]

to the sample surface to prevent any channelling of bombarding ions. The mean projected range of the 4 MeV Au particles we used is estimated - based on SRIM¹ calculations [2] - to be $R_p \sim 530$ nm with a range straggling $\Delta R_p \sim 140$ nm [Figure 2.1.2]. Ion fluences ranged from 5×10^{12} to $2 \times 10^{16} \text{ cm}^{-2}$; the corresponding conversion factor for the dpa at the damage peak is $\sim 4.5 \times 10^{-15} \text{ dpa cm}^2$, as determined by SRIM calculations using a threshold displacement energy of 40 eV for both Zr and O sublattices. Therefore, the dpa ranged from ~ 0.02 to ~ 90 .

2.1.2 RUTHERFORD BACKSCATTERING SPECTROMETRY

Rutherford backscattering spectrometry (RBS) is a widely used technique for the near surface layer analysis of solids. It is based on the elastic interaction between the target nucleus and the projectile. A target is bombarded with light elements such as Hydrogen or Helium ions and the energy of the backscattered projectiles is recorded with an energy sensitive detector. The energy of the projectile ranges from a few hundreds of keV to, most frequently, a few MeV which results in an analysed depth up to a few micrometers.

The principle of RBS is demonstrated in the figure (2.1.3). An incident beam of energy E_{c1} is directed towards the material. The incident beam interacts with lattice atoms at the target surface which results in the scattering of projectile in all directions. The ratio of the projectile energy before (E_0) and after collision (E_1) is known as the kinematic factor (K).

$$E_1 = E_0 \times K \quad (2.1)$$

¹SRIM (Stopping and Range of Ions in Matter) [2] is a Monte-Carlo program that allows simulating ion/matter interactions.



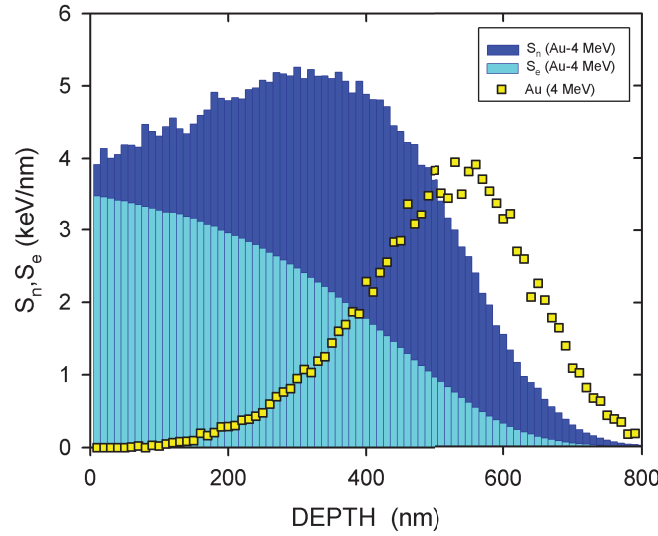


Figure 2.1.2: Energy loss by elastic and inelastic collisions of 4 MeV Au ions in YSZ determined using SRIM calculations.

where the Kinematic factor (K) is given by the equation below

$$K = \frac{M_1^2}{(M_1 + M_2)^2} \left\{ \cos \theta \pm \left[\left(\frac{M_2}{M_1} \right)^2 - \sin^2 \theta \right]^{1/2} \right\}^2 \quad (2.2)$$

In the above equation, when the mass of the projectile is less than the target, *plus* sign is taken and if it is greater, *minus* sign is used. From this equation the masses of the particles composing a material can be known by measuring the energy of the backscattered particles and by the knowledge of both the masses and energy of the projected particles. So this technique allows determining the elemental composition. The number of particles backscattered from a target atom into a given solid angle for a given number of incident particles is related to the backscattering cross section derived from the Coulomb potential. According to the theory of Rutherford interaction, the cross section of the backscattering $d\sigma/d\Omega$ in a solid angle $d\sigma$ along the direction θ is given by [3]

$$\frac{d\sigma}{d\Omega} = \frac{1}{4\pi\epsilon_0} \left(\frac{Z_1 Z_2 e^2}{4E_0} \right)^2 \times \frac{4}{\sin^2 \theta} \frac{\{ [1 - (M_1^2/M_2^2) \sin^2 \theta]^{1/2} + \cos \theta \}^2}{[1 - (M_1^2/M_2^2) \sin^2 \theta]^{1/2}} \quad (2.3)$$

where Z_1 and Z_2 are atomic numbers of the projectile and the target, ϵ_0 is the vacuum permittivity and θ is the scattering angle. From the equation, the cross section is inversely proportional to the square of the energy of the incident particle *i.e.*, higher the incident energy, smaller the cross section. It is possible to estimate the atomic density of M_2 particles in the sample by counting the yield of the scattered particles M_1 detected at the angle θ by the detector.



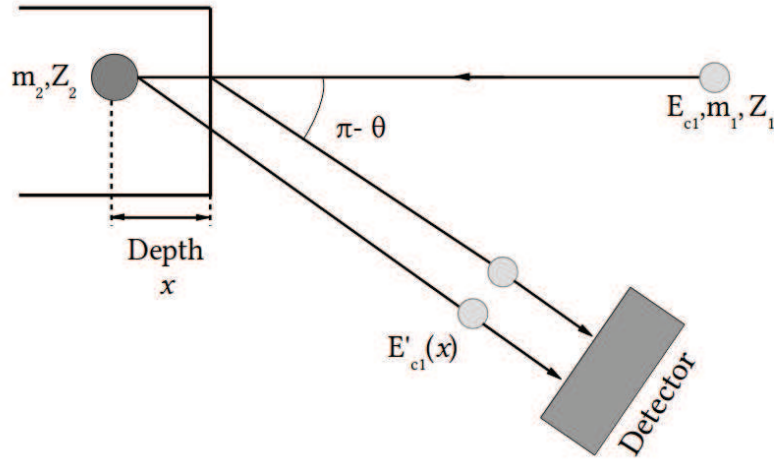


Figure 2.1.3: Rutherford backscattering geometry

ENERGY LOSS AND DEPTH SCALE

The backscattered atoms from deeper parts of the sample also suffers an energy loss while navigating through the sample due to collisions with the sample atoms. Energy-loss per unit length values are tabulated for a very wide projectile-target couple range, allowing to determine composition depth profiles. As mentioned above, the loss of energy during the collision process allows backscattering spectrometry to detect different masses in the target. The energy loss dE/dx by the projectile as it traverses the sample will allow the extraction of depth information from the sample.

In addition to energy losses during collision, incident particles will also lose energy as they travel into the target before the collision and out of the target after the collision. In order to perform the depth profiling of RBS spectra, we need to relate the energy of the backscattered ion to the depth in the sample at which the backscattering takes place [4]. This relation depends on the energy loss of ion while traversing the sample, the kinematic factor of the scattering and on the angle between incident beam and the detector's normal vector. The depth scaling is estimated with the assumption that the stopping powers on the inward and outward paths are constant. Therefore, the energy of detected ion that backscatters at depth x from the surface can be given as follows

$$E_1(x) = KE_0 - xS \quad (2.4)$$

where $E_1(x)$ is the detected energy of ion that backscattered at depth x , E_0 is the initial energy of the incident beam and S is the energy loss factor. In this formula, S is calculated as follows:

$$S = K \left(\frac{dE}{dx} \right)_{in} \frac{1}{\cos \theta_1} + \left(\frac{dE}{dx} \right)_{out} \frac{1}{\cos \theta_2} \quad (2.5)$$



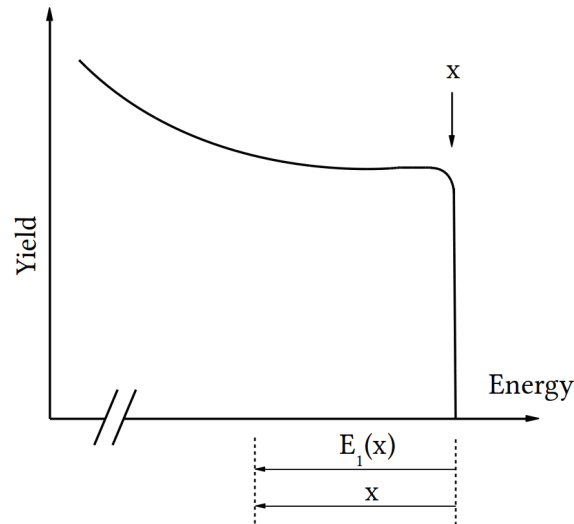


Figure 2.1.4: The graph of energy $E_1(x)$ plotted against the depth x to show that the energy $E_1(x)$ can be linearly related to the depth x

Thus the depth at which the backscattering takes place will be

$$x = \frac{KE_0 - E_1(x)}{S} \quad (2.6)$$

The assumption that dE/dx is constant along the inward and outward paths leads to a linear relation between $E_1(x)$ and the depth, x , at which scattering occurs. One can therefore assign a linear depth to the energy axis, as indicated in figure (2.1.4). It is worth mentioning that RBS/C simulation codes exist (such as RUMP, SIMNRA) which allow fitting the experimental data to get the composition depth profile of samples without using this surface approximation.

CHANNELLING

Channelling is observed when the incident beam is aligned with a major symmetry axis of the crystal. RBS with channelling technique applies only for single crystals or good quality epitaxial layers. The advantage of this technique is that the lattice site target atoms are seen as rows of periodically repeated atoms between which the ion channels. The part of the incident beam which avoids the collision with surface atoms is excluded from collisions with all atoms deeper inside the sample. If the interatomic distance is large with respect to the radius of the shadowed cone, the incident ions can penetrate deeper without being backscattered (figure 2.1.5). This results in the reduction of detected number of backscattered ions as most ions channel through the crystal. A very small fraction (about 1%) of backscattered ions are recorded compared to the situation in which ion beam is randomly oriented.

Figure (2.1.6) shows the classical spectra recorded by RBS in channelling mode. The three different spectra represent the backscattering in different conditions. In the first case (blue spectrum), the ion beam is oriented along the crystallographic orientation of a perfect crystal. Since a perfect crystal has



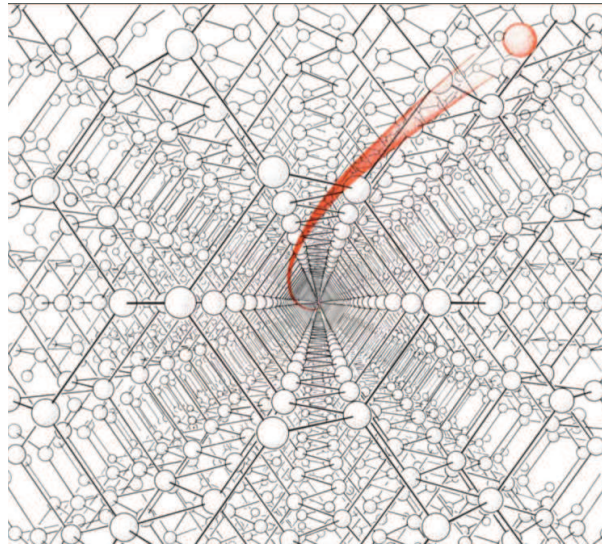


Figure 2.1.5: The path of a Channelling particle inside a diamond-like crystal lattice [5]

no defects, the backscattering signal is extremely weak. Most of the incident ions just channel through the crystal. The second one is measured for a random orientation (red spectrum) of the crystal with respect to the incident beam. In this case, the backscattering signal is high (and maximum) since the probability of backscattering of the incident ion is also maximal. While performing experiments, the random spectrum is usually recorded by rotating the crystal by a random angle around the incident beam. In the third case (green spectrum), the ion beam is oriented along the crystallographic orientation of the crystal containing defects. Here, since some atoms are present in random positions of the crystal, backscattering signal is observed but much less than for the random orientation (considering that the material is not severely damaged). The obstruction to the incident ion beam at a given depth from the surface of the crystal is related to the local concentration of the defects. By careful observation of the spectrum, we can see a surface peak due to the backscattering of ions upon atoms located at the surface of the crystal, a damage peak which results from direct backscattering upon atoms which are randomly distributed within the lattice structure and a de-channelling signal (a kind of S-shaped background) resulting from the small angle scattering of incident ions upon both lattice atoms and defects.

McCHASY CODE

Ion channelling is often used for detecting the structural defects located from the surface layer of a crystalline material to a depth of a few μm . To analyse the data, one of the efficient methods is performing simulations using McChasy code developed by Nowicki et. al. [6]. McChasy (abbreviation for Monte-Carlo CHAnnelling SYmulation) is a computational program designed for the calculation of ion-crystal interaction in channelling mode. The parameters declared in this program include the parameters about the crystal, the geometrical details, the analysing beam specifications and the energy resolution. Using



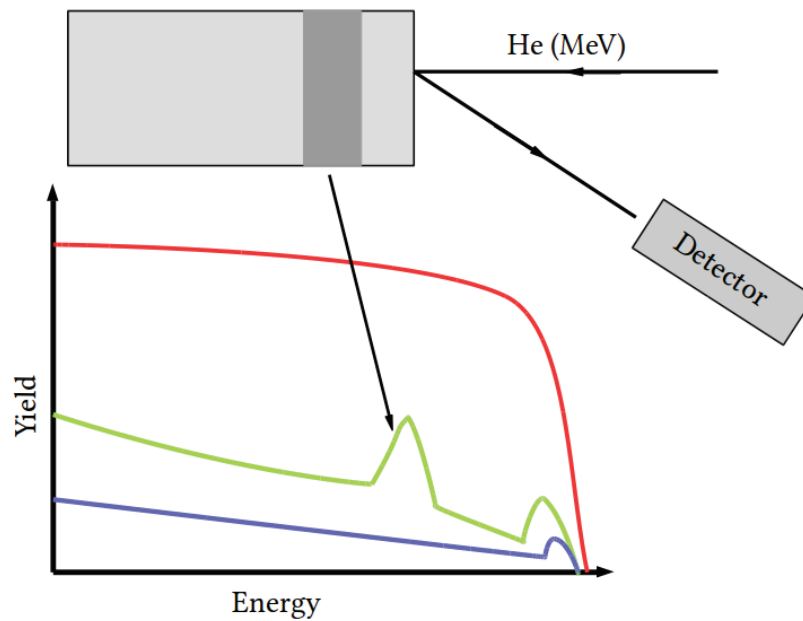


Figure 2.1.6: Conventional channelling spectrum observed for a crystal containing defects (green). The random spectrum is marked in red and the channelling spectrum from a perfect crystal is marked in blue.

McChasy, one can calculate the damage fraction and the distribution of defects versus depth in the crystal. The program can take into account two types of defects : randomly displaced atoms (equivalent to point defects at low concentration) and extended defects, namely dislocations. In the present work, we only used displaced atoms. The analysis by the McChasy program is performed according to the following steps. Firstly, declaring parameters related to (i) the studied crystal, which includes the structure and composition; (ii) and the measurement condition (*e.g.*, analysing beam energy and nature). Secondly, the crystal is divided into thin layers of a few nanometres to a few hundreds nanometres. In each layer, a given fraction of displaced atoms (f_D) is defined as input for simulation. Simulation can then be performed and the output is a channelling spectrum that contains information on the backscattering events as a function of the probing particle energy.

2.1.3 X-RAY DIFFRACTION

EXPERIMENTAL SET-UP

X-ray diffraction was performed with two experimental set-ups. The first one, a high resolution four-circle Seifert XRD3000 Diffractometer operated at 40 kV and 40 mA and equipped with a standard Cu tube. The different rotations are represented in figure (2.1.7). The diffractometer is equipped with a double-crystal monochromator ($2 \times \text{Ge}220$) which provides a parallel and monochromatic incident X-ray beam ($\text{Cu}_{K\alpha 1}$ radiation, $\lambda = 0.15406 \text{ nm}$). A 0.07 mm detector slit were used to obtain a 2θ angular resolution of 0.01° . Crystals irradiated at room temperature were analysed with this diffractometer.

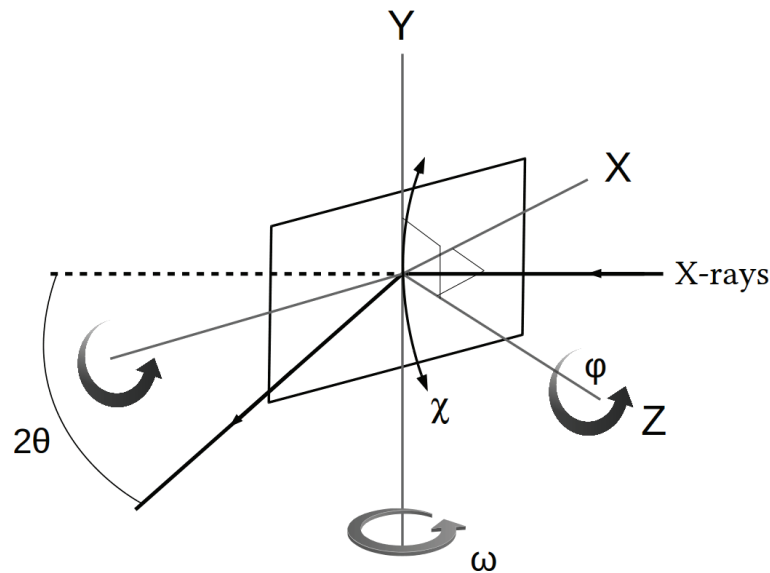


Figure 2.1.7: Different rotations of a four-circle goniometer

The other equipment include a PANalytical X'Pert PRO MRD diffractometer which is also equipped with a standard Cu tube. The schematic representation of the PANalytical X'Pert PRO MRD diffractometer is given in figure (2.1.8). An intense and monochromatic beam was obtained by using a multi-layer mirror behind the tube followed by a four-crystal monochromator ($4 \times Ge(220)$) in asymmetric configuration. The resulting primary-beam divergence was 18 arcsec (0.005°). A three-bounce crystal analyzer ($3 \times Ge(220)$) was used to further limit the detector acceptance. The crystals irradiated at temperatures 80 K, 573 K, 773 K and 1073 K were analysed using this diffractometer. All measurements have been carried out at room temperature. Symmetric $\theta - 2\theta$ scans were recorded in the vicinity of the (4 0 0) Bragg reflection, *i.e.* around $2\theta = 73.575^\circ$.

SYMMETRIC GEOMETRY

The $\theta - 2\theta$ scan is one of the most common scanning configuration. In this geometry, for a symmetric reflection, the angle of both the incoming and the outgoing beam are equal to θ with respect to the sample surface. The figure (2.1.9) represents the scattering plane consisting of the incident and exit wave vectors \mathbf{k}_0 and \mathbf{k} , \mathbf{Q} is the scattering vector. For the symmetric $\theta - 2\theta$ scan, the scattering vector \mathbf{Q} is normal to the sample surface and collinear to the reciprocal lattice vector \mathbf{h} corresponding to the (hkl) planes parallel to the sample surface. During the scan the angle of the incoming and exiting beam are continuously varied, but they remain equal throughout the whole scan *i.e.*, $\theta_{in} = \theta_{out}$. By doing so, the reciprocal space is scanned along the normal component of the scattering vector.



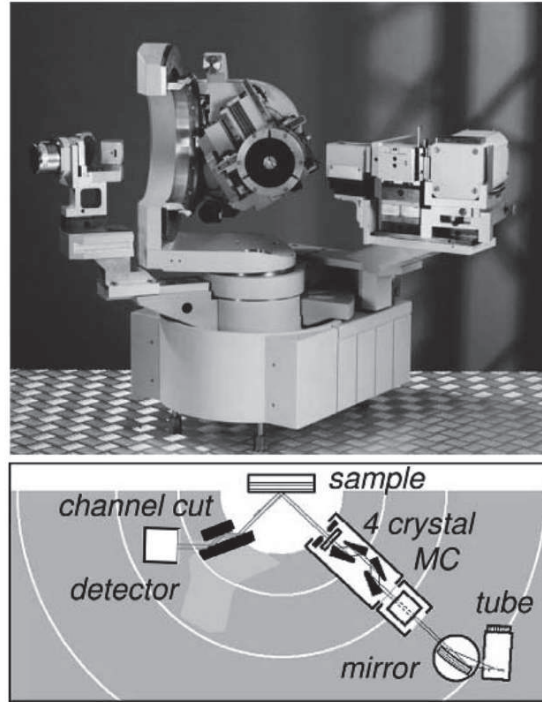


Figure 2.1.8: Four-circle PANalytical diffractometer [7]

ASYMMETRIC GEOMETRY

The measurement of a rocking curve is performed such that the detector on the 2θ circle is fixed, while the sample is tilted on the θ circle ("rocked") in the vicinity of the Bragg angle θ . The θ circle and the 2θ circle are thus decoupled and the θ angle is called ω in the case of its independent variation. In this geometry for a symmetric reflection, the scattering vector scans the reciprocal space along an arc of circle, which, for sufficiently small deviations can be considered as parallel to the surface (See fig. 2.1.9).

RECIPROCAL SPACE MAPPING

From the symmetric $\theta - 2\theta$ scan, we saw that the scattering vector \mathbf{Q} has only a nonzero component in the direction of the substrate normal. This component is denoted by Q_z . However, during a rocking curve scan, there is also a nonvanishing in-plane Q_x component for all angular positions ω except for one point where $\omega = 2\theta/2$ holds. We can visualize the different scanning techniques in the plane of momentum transfer by the in-plane component Q_x and the out-of-plane component Q_z of the scattering vector. The relation between the instrumental coordinates ω and 2θ and Q_x and Q_z coordinates can be derived from the figure (2.1.9). It results from the inspection of the figure that

$$\mathbf{Q}_x = 4\pi/\lambda \sin(\theta) \sin(\omega - \theta) \quad (2.7)$$



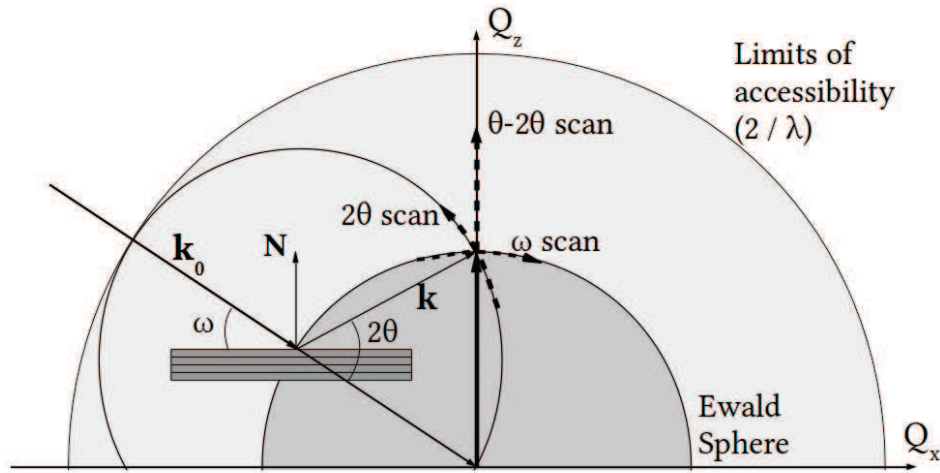


Figure 2.1.9: The schematic representation showing 2θ , $\theta/2\theta$, ω in the case of a symmetric reflection, the Ewald construction where \mathbf{k}_0 and \mathbf{k} are the incident and the exit wave vectors, \mathbf{Q} is the corresponding scattering vector

$$Q_z = 4\pi/\lambda \sin(\theta) \cos(\omega - \theta) \quad (2.8)$$

Reciprocal space mapping is performed such that the Bragg reflection under investigation is fully mapped in a confined area in Q space. This means that the reflection is not only monitored by one rocking curve crossing it, but the whole area in the vicinity of the reflection is included in the measurement. As an example, figure (2.1.10) displays the reciprocal space map (RSM) recorded in the vicinity of the (0 0 4) reflection of a Cs-implanted YSZ crystal [8]. The RSM from this irradiated crystal contains a strong signal (marked as dashed corresponding to $Q_z \sim 4.88 \text{ \AA}$ in the figure). This signal comes from the substrate, *i.e.*, unperturbed part of the sample. In addition to this strong signal, the signal arising in the lower values of Q_z corresponds to the irradiated (damaged) part of the sample. The different features observed in this RSM are extensively discussed in the Chapter 4.

2.2 COMPUTATIONAL TECHNIQUES

2.2.1 INTRODUCTION

The previous chapter gave an account of the theories of X-ray diffraction and the ion irradiation physics. Physically, the dimensions of a typical single crystal is of the order of a few tens of μm thickness and a few millimetres of length and width. This means that, a typical crystal contains several billions of unit cells. The diffracted amplitude from a crystal, as given in equation (1.17), is

$$E(\mathbf{Q}) = \sum_n F_n e^{i\mathbf{Q}\mathbf{r}_n} \quad (2.9)$$

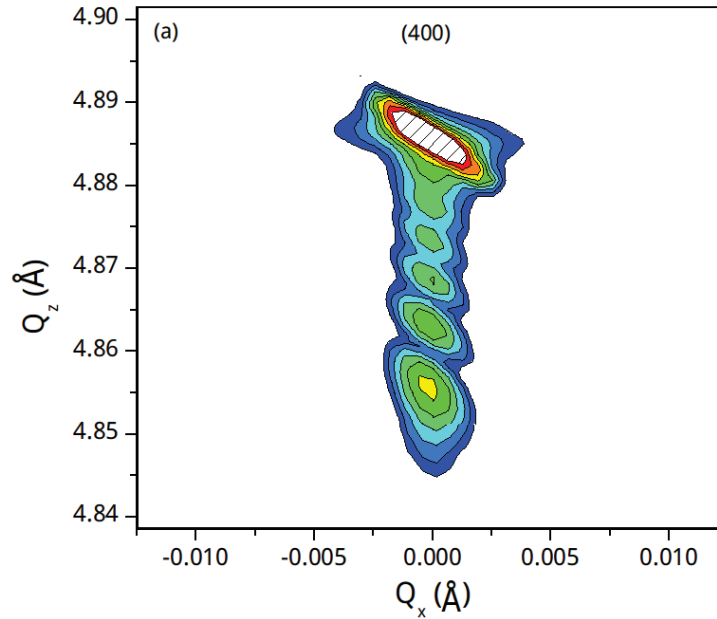


Figure 2.1.10: Reciprocal space map recorded in the vicinity of the (004) reflection of Cs-implanted YSZ crystal [8]

Consequently, to obtain the amplitude for billions of \mathbf{r}_i and for each value of scattering vector \mathbf{Q} , several thousands of billions of function evaluation are required. Using a single-core computer - retaining the unit-cell resolution - it would take several days together to retrieve the overall results. Interestingly, in the case of equation (2.9), the sum over n can be carried out independently for all \mathbf{Q} values. It can therefore be anticipated that the evaluation of equation (2.9) would greatly benefit from parallel computing *i.e.*, breaking a large computational problem into smaller ones and solving them concurrently.

2.2.2 EVOLUTION OF COMPUTING

In the history of computing hardware, the number of transistors in a dense integrated circuit had doubled approximately every two years. This observation, referred to as Moore's law, was presented by Gordon E. Moore, co-founder of Intel, in his paper in 1965 [9] [10]. Though this law is an observation and not a physical or a natural law, it has served as a projection and guidance for the semiconductor industry. Accordingly, the size of the transistors is decreasing consistently in the last few decades as illustrated in the graph (2.2.1) [11]. Currently, manufacturers are able to build transistors of feature size of 14 nm. Although this trend has been followed for more than half a century, doubts about the ability of the projection to remain valid in the future have been expressed [12].

Despite this constant increase in the transistor density, in the last decade, the clock frequency stagnates

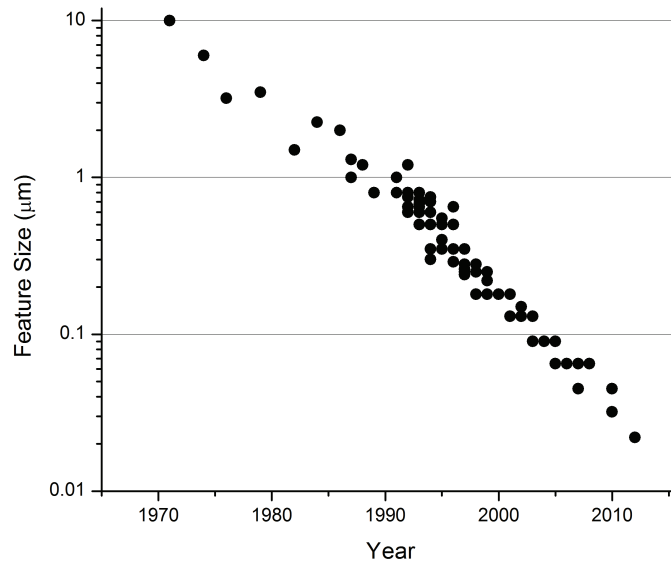


Figure 2.2.1: Feature size of transistors over the past few decades

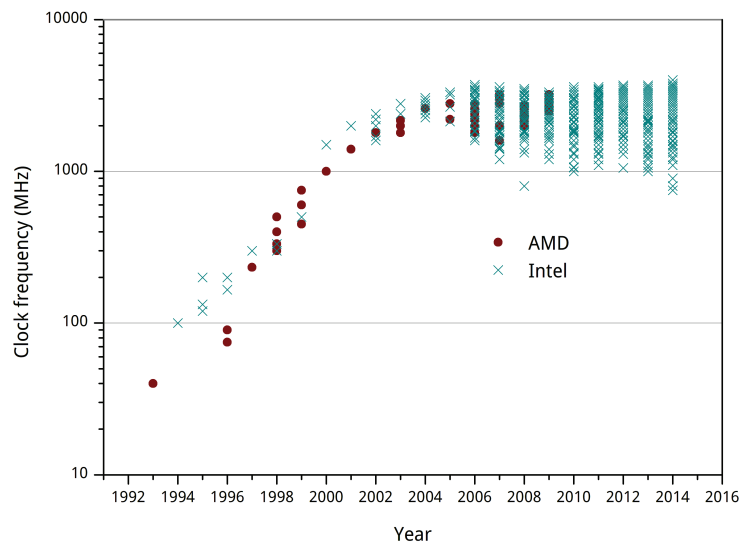


Figure 2.2.2: The clock frequency of different processors from the two major companies in the past 25 years. In the last decade, it has remained almost constant [11].



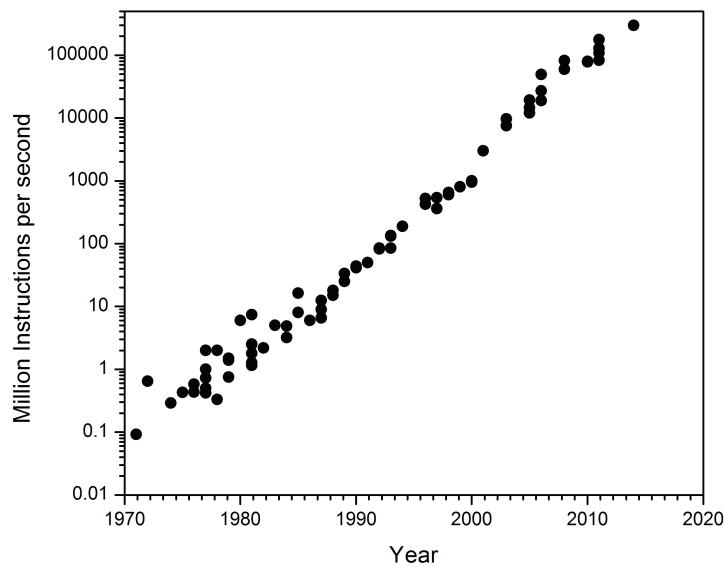


Figure 2.2.3: The computing speed of different processors over the past few decades

at values around 3.7 GHz (figure 2.2.2). Clock speed refers to the frequency at which a single core of a CPU is running, and is used as an indicator of the processor's speed. The reason for this is the so-called power wall [13]: because the power consumption of a CPU is proportional to the frequency cubed [14], the power density was approaching that of a nuclear reactor core [15]. Unable to cool such chips sufficiently, the trend of exponential frequency growth stopped at just below 4.0 GHz (Figure 2.2.2). To overcome the clock stagnation and increase the number of Instructions Per Second (IPS), companies started to include more than one processing cores inside a single computer. This helped in overcoming the problem of clock speed and improve the performance further. Over the years, the CPU manufacturers started to release three-, four-, eight-core central processor units. The release of multicore CPUs have revolutionized the computing performance and allows parallel computing as well [16] [17]. With the help of this, the computing speed (expressed in Million instructions per second) continued increasing over years (Figure 2.2.3). However, this is mainly a commercial argument because most of the end-user applications and programming languages make use of a single core at a time. In order to take full advantage of this theoretical power, the programs have to be actually rewritten in order to address several cores simultaneously. This is the purpose of multiprocessing. Another important limitation comes from the fundamental design philosophy of a CPU, as illustrated in the figure (2.2.4). The design of a CPU is optimized for sequential code performance. It makes use of sophisticated control logic to allow instructions from a single thread of execution to execute in parallel. The time needed to process the data is actually limited by the speed at which the data is transferred to the CPU. This latency is known as von Neumann bottleneck. Interestingly, this problem is solved by Graphical Processing Units (GPUs)



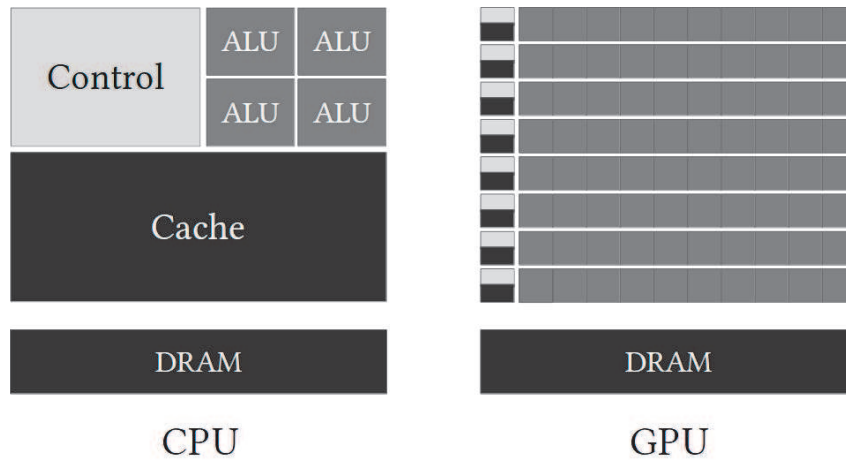


Figure 2.2.4: The design philosophy of a CPU and a GPU

which rely on a different architecture. The design philosophy of a GPU is shaped by the fast growing video game industry, which exerts tremendous economic pressure for the ability to perform a massive number of floating-point calculations per video frame in advanced games. This resulted in optimization of data transfer rate of massive number of threads. The hardware takes advantage of a large number of execution threads to work while waiting for long-latency memory accesses *i.e.*, minimizing the control logic required for each execution thread. With the GPU architecture, the peak performance is much higher than CPUs (figure2.2.5). The price to pay to benefit from this huge computing power is that the programs have to be completely rewritten so as to be executed on a GPU instead of a CPU.

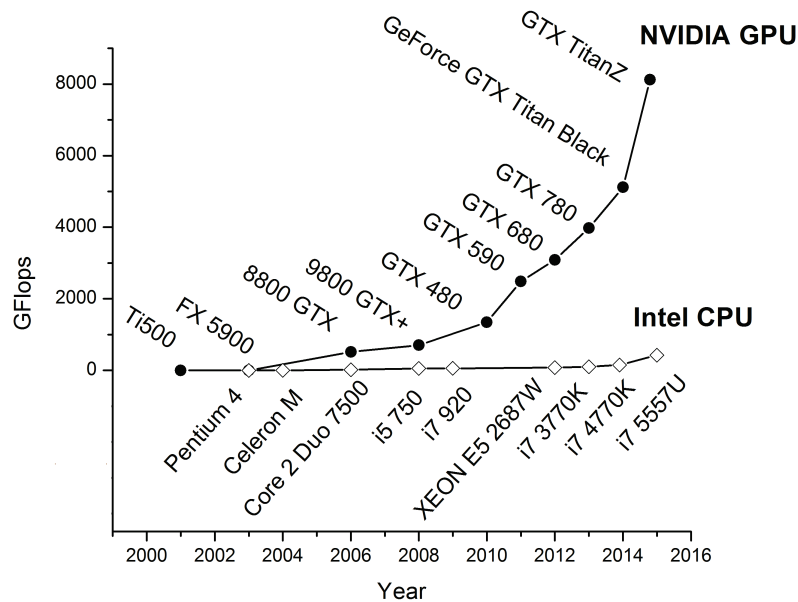


Figure 2.2.5: The evolution of the peak performance in terms of GFlops for CPUs and GPUs over time



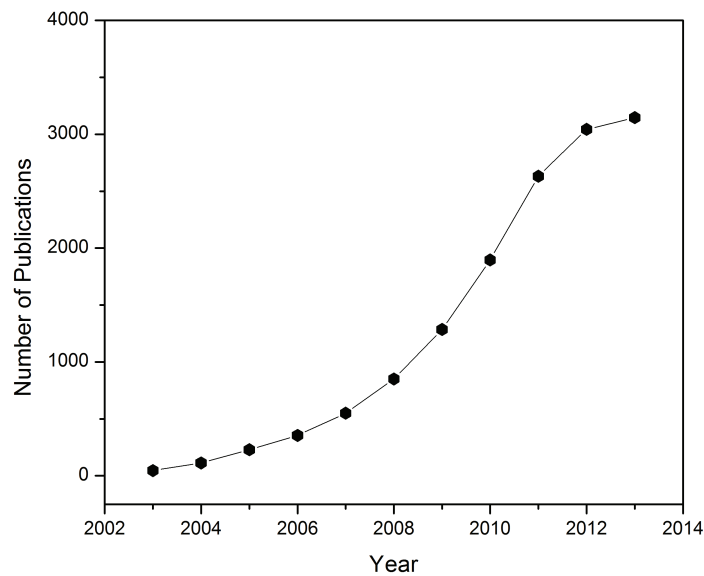


Figure 2.2.6: The number of publications on the title "GPU" OR "Graphical Processing Unit" OR "Graphic Processing Unit" obtained from the WebOfScience dated 12/06/2015 [32]

2.2.3 GPUs AS PARALLEL COMPUTERS

Curiously, GPUs were never designed with high-performance computing in mind. They were built mostly for the gaming industry. But nonetheless, they have evolved into powerful processors in less than ten years. The development of both the software and hardware together have lead us to a new era of parallel computing. In the scientific community, the usage of GPU has already been implemented in many fields, like molecular dynamics [18] [19], bioinformatics [20], geoscience [21], quantum chemistry calculations [22] [23], medical imaging [24] [25] [26] [27], astronomy [28], fast Monte-Carlo in proton therapy [29] *etc.* The number of scientific publications on GPU is increasing on a very fast rate since 2003 (graph 2.2.6).

At around 1980, the company *Silicon Graphics* popularized the use of three-dimensional graphics in the market. It was used in government and defence applications and scientific and technical visualization. Later in 1992, Silicon graphics released the *OpenGL* library which is a programming interface to its hardware [30]. In a few years, the gaming industry started booming and companies such as NVIDIA and ATI Technologies began releasing graphics accelerators that were affordable enough to attract widespread attention. For the first time, transform and lighting computations could be performed directly on the graphics processor. From a parallel-computing standpoint, NVIDIA's release of the GeForce 3 series in 2001 represents arguably the most important breakthrough in GPU technology [31]. For the first time, developers had some control over the exact computations that would be performed on their GPUs.

Though the release of GPUs that possessed programmable pipelines attracted many researchers, there



were numerous problems and complexities that were preventing the programmers from taking full benefits from the GPU. In November 2006, NVIDIA unveiled the industry's first DirectX 10 GPU, the GeForce 8800 GTX. The GeForce 8800 GTX was also the first GPU to be built with NVIDIA's Compute Unified Device Architecture (CUDA). In order to reach the maximum number of developers possible, NVIDIA took industry-standard C and added a relatively small number of keywords in order to harness some of the special features of the CUDA architecture. Consequently, CUDA C became the first language specifically designed by a GPU company to facilitate general-purpose computing on GPUs (GPGPUs). In addition to creating a parallel-computing platform for the GPU, NVIDIA also provides a specialized hardware driver to exploit the CUDA Architecture's massive computational power.

Currently, GPUs are equipped with humongous number of CUDA cores in comparison with CPU cores. As an example, the latest GPU NVIDIA GeFORCE GTX TITAN Z has 5760 CUDA cores in comparison with GeForce 8 series (released in 2008) which had 32 CUDA cores only. The number of CUDA cores in GPUs are increasing in a rapid manner because of which GPUs are able to perform massively parallel calculations. Clearly, the memory capacity of each CUDA core is much smaller compared to a single CPU core. However, with the help of parallelization, GPUs have the ability to handle big data.

2.2.4 CUDA PROGRAMMING

General Purpose GPU (GPGPU) using CUDA has been used to accelerate non-graphical applications in computational biology, cryptography and many other fields [33] [34] [35]. In CUDA programming, the computer is treated as a heterogeneous computer. This means that along with other essential components, they have two different processors in them, the CPU and the GPU. The CUDA programming model allows the programmers to utilize both processors with one program so that the full power of the GPU can be harnessed. Though it is built on ANSI C with some extensions to express parallelism, CUDA supports numerous programming languages. To understand the functioning of the GPU, we shall assign the CPU as *host* and GPU as *device*. The CUDA compiler will compile the program, split it into pieces that will run on the CPU and the GPU, and generate code for each. CUDA assumes that the device, the GPU, is a co-processor to the host, the CPU. It also assumes that both the host and the device have their own separate memories where they store data. Both the CPU and the GPU have their own physical dedicated memory in the form of DRAM (Dynamical Random Access Memory), with CPU as the primary memory unit and the GPU being the massively parallel processors equipped with large number of arithmetic execution units (figure 2.2.4). GPUs consist of DRAM much lesser in comparison with the CPUs. Currently, the best GPU for a desktop computer consists of 12GB of RAM whereas, we can find computers having CPU RAM upto 128GB. So this allows the computation of huge amount of data to be performed in a CPU and relatively less amount of data can be computed in the GPU. Now, in this relationship between CPU and GPU, CPU is the primary device. It runs the main program, and it sends directions to the GPU. It's the part of the system that's responsible for moving the data from the



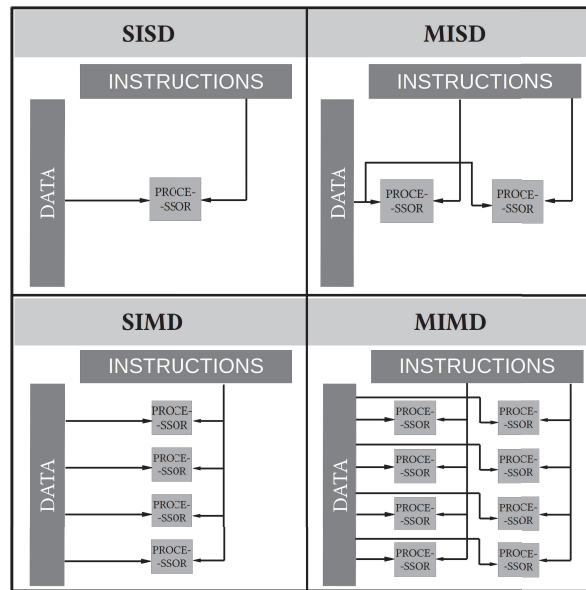


Figure 2.2.7: Visualization of Flynn's taxonomy

CPU's memory to the GPU's memory and vice versa.

The algorithm for a typical program looks like this :

- CPU allocates storage on GPU
- CPU copies input data from CPU to GPU
- CPU launches kernel(s) on GPU to process the data
- CPU copies results back to the CPU from GPU

In CUDA, invoking programs on the GPU that compute things in parallel are called *kernels*. Two of the above steps in the algorithm require moving data back and forth between the CPU and the GPU. In general, the most efficient parallel computing method is to minimize data transfer between the CPU and the GPU. CUDA or GPU computing probably isn't the right choice if there are ample data transfer and minor computation. It is not simply the speed at which a certain algorithm processes data that is important, but how that data has been used prior to, and how it will be used after the kernel is run. GPU kernels are fast, and in many cases kernels are completed in the tens of milliseconds timeframe. Given that, the movement of data to and from the GPU becomes relevant, both because of the amount of data that needs to be moved, and because of the inherent bottleneck from the interconnect between the CPU and GPU. Without acknowledging the time for these data transfers, comparisons do not provide a true representation of the real speedup provided by a device. Universally, the most successful GPU computing applications have complex computation and a high ratio of computation to communication.



2.2.5 FLYNN'S TAXONOMY

Computer architectures characterize the methodologies of the processors, how they work, communicate, organize etc. Michael J. Flynn proposed a classification of computer architectures in 1966, which is now known as Flynn's taxonomy [36] [37] [38]. This classification is used as a tool to design modern processors and their functionalities [39] [40] [41]. Flynn classified the whole computer architecture into four different categories, Single Instruction, Single Data stream (SISD), Single Instruction, Multiple Data stream (SIMD), Multiple Instruction, Single Data stream (MISD) and Multiple Instruction, Multiple Data stream (MIMD). Each of them can be visualized in the figure (2.2.7). This classification mainly depends on number of concurrent instructions and the available data stream in the architecture. A data stream is nothing but a sequence of objects or actions.

SINGLE INSTRUCTION, SINGLE DATA STREAM (SISD)

The SISD class of processor architecture is a sequential computer which offers no parallelism in either the instruction or data streams [42]. Single control unit fetches single instruction stream from memory and generates appropriate control signals to direct single processing system to operate single data stream. A typical example is the uniprocessor CPUs of the 1950s, which were based on the original von Neumann architecture. The rest of the architectures are built by combining many von Neumann building blocks.

SINGLE INSTRUCTION, MULTIPLE DATA STREAM (SIMD)

SIMD is a type of architecture which offers data parallelism. In this architecture, a computer exploits multiple data streams against a single instruction stream to perform naturally parallelized operations. This architecture is very useful for building mathematical models for various problems. It was first implemented in vector computers during 1970 and 80s. Current GPUs are contemplated as an evolution from SIMD architecture.

MULTIPLE INSTRUCTION, SINGLE DATA STREAM (MISD)

MISD is an uncommon architecture in which multiple instructions operate on a single data stream. Heterogeneous systems operate on the same data stream and hence they must agree on the result. Since the problems MISD computer can calculate are uncommon and very specific, there aren't many actual examples. One example include the space shuttle flight control computer.

MULTIPLE INSTRUCTION, MULTIPLE DATA STREAM (MIMD)

MIMD class of parallel architecture consists of multiple processors with some form of interconnection. Here, multiple processors simultaneously execute different instructions on different data. It has the ability to handle one different instruction for each data stream and can achieve any type of parallelism. This



architecture is implemented in the current CPUs and in some GPUs.

The MIMD can be further classified into SPMD (single program multiple data) and MPMD (multiple program multiple data).

SPMD : SPMD refers to the case in which a simple program is executed simultaneously by different processors. SPMD is the most common style of parallel computing and can be built upon any combination of the parallel programming models. SPMD programs usually have the necessary logic programmed into them to allow different tasks to branch or conditionally execute only those parts of the program they are designed to execute. *i.e.*, tasks do not necessarily have to execute the entire program - perhaps only a portion of it. In CUDA, a kernel function specifies the code to be executed by all threads during a parallel phase. Because all of these threads execute the same code, CUDA programming is an instance of SPMD [43].

MPMD : Like SPMD, MPMD is also a high level programming model that can be built upon any combination of the parallel programming models. Multiple program, which means, tasks may execute different programs simultaneously. It is the most flexible architecture but MPMD applications are not as common as SPMD applications. They are best suited for certain types of problems, particularly those that lend themselves better to functional decomposition than domain decomposition.

2.2.6 PARALLEL COMPUTING SPEEDUP

Speedup is a unit to measure the relative performance improvement of a particular task. It is one of the important aspect in parallel computing, to measure how much faster a parallel program executes in comparison to the serial program. Speedup can be defined for two different types of values: throughput and latency. Latency is the amount of time to complete a task and is measured in the units of time. Throughput is tasks completed per unit time. Traditionally CPUs optimize for latency as they try to minimize the time elapsed for one particular task. GPUs on the other hand are optimized for throughput. For latency values, speedup for a problem of size S is given by the expression :

$$Speedup = \frac{T_s(S, 1)}{T(S, N)} \quad (2.10)$$

where $T_s(S, 1)$ is the time of the best sequential algorithm (*i.e.*, $T_s(S, 1) \leq T(S, 1)$) and $T(S, N)$ is the time of the parallel algorithm with N processors, both solving the same problem. Speedup is upper bounded when S is fixed.



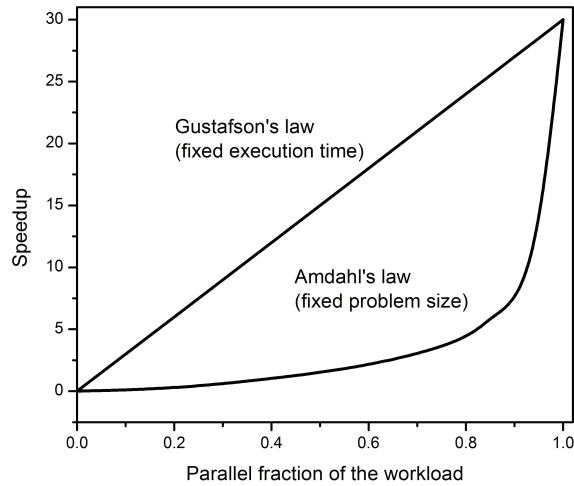


Figure 2.2.8: Speedup behaviour using Amdahl's law and Gustafson's law [42].

AMDAHL'S LAW

The idea of speedup was first given by Amdahl's law[44][45]. According to Amdahl's law, for parallelization, the maximum speedup that can be achieved is written as:

$$S(N) = \frac{1}{(1 - P) + \frac{P}{N}} \quad (2.11)$$

where P is the fraction of a program that can be made parallel and $(1-P)$ that cannot be parallelized (remains serial) and N is the number of processors. When N tends to infinity, the maximum speedup tends to $1/(1 - P)$.

GUSTAFSON'S LAW

Gustafson's law [46] is another useful measure for theoretical performance analysis. It provides a counterpoint to Amdahl's law as it uses the fixed-time model where work per processor is kept constant when increasing P and N . In Gustafson's law, the execution time of a parallel program is decomposed into sequential time s and parallel time c :

$$T(p) = s + c \quad (2.12)$$

So according to Gustafson's law, the speedup becomes

$$S(N) = N - a(N - 1) \quad (2.13)$$

where N is the number of processors and a is the non-parallelizable fraction of any parallel process given by $s/(s + c)$. Gustafson's law helps in exploiting the shortcomings of Amdahl's law, which does not fully



exploit the computing power which becomes available as the number of machines increases. Amdahl's law only applies to cases where the problem size is fixed. Gustafson's Law proposes the possibility to solve a larger problem in the same amount of time. It suggests that programmers tend to set the size of problems to use the available equipment to solve problems within a practical fixed time. Hence, if an equipment with more parallel option is available, larger problems can be solved in the same time. The idea is that if the problem size is allowed to grow monotonically with N , then the sequential fraction of the workload would not dominate in the end.

2.2.7 WORK STATION AND GPU SPECIFICATIONS

All the simulations in this work were performed on a Dell Precision T5610 workstation and a NVIDIA Quadro K4000 GPU. Workstations offer higher performance than mainstream personal computers with respect to CPU, graphics, memory capacity and multitasking capabilities. Our workstation has a total RAM of 64 GB and consists of two Intel Xeon E5-2609 CPUs which correspond to 8 cores in total and performs at a clock frequency of 2.5 GHz. NVIDIA Quadro GPUs are designed for workstations which are used ideally for technical or scientific applications. This table gives an overall technical specifications of the NVIDIA Quadro K4000 GPU:

Table 2.2.1: NVIDIA Quadro K4000 GPU technical specifications

GPU Memory	3 GB GDDR5
Memory Interface	192-bit
Memory Bandwidth	134.0 GB/s
CUDA Cores	768
Maximum Power Consumption	80 W
Graphics APIs	Shader Model 5.0, OpenGL 4.4, DirectX11
Compute APIs	CUDA, DirectCompute, OpenCL



Figure 2.2.9: NVIDIA Quadro K4000 GPU



2.2.8 PYTHON PROGRAMMING LANGUAGE

Python is a powerful programming language considering portability, flexibility, syntax, style and extendibility [47]. All the programs written during this thesis are written in Python. Python is attractive for scientists mainly because of these following reasons :

- Python is easier to read and to program than other programming languages. It is very well designed and it is easier than other languages to transform the ideas into code.
- Open-source software and freely available, whereas languages, such as Matlab (which can be used to perform scientific computing) is a closed-source commercial product. The consequence of which, Python's ever increasing libraries - built by users to perform scientific and mathematical operations- makes Python more powerful. Additionally, a large community is dedicated in the development of packages, bug fixes and user-support. It also includes an adequate online help and detailed documentation.
- Portability : Implementation on all standard platforms, *e.g.*, Linux, Unix, Windows, Mac OS X.

The basic operations used in scientific programming include arrays, matrices, integration, differential equation solvers, statistics and much more. Python, by default, does not have any of these functionalities built in, except for some basic mathematical operations that can only deal with a variable and not an array or matrix. Three packages in particular are the powerhouses of scientific Python: *NumPy*, *SciPy* and *matplotlib*.

NUMPY

NumPy is one of the fundamental Python packages for scientific computing. Documentation and download are available at <http://www.numpy.org/> [48]. It is based on Numeric, one of the earlier Python array packages. NumPy adds the capabilities of N -dimensional arrays, element-by-element operations, large library of high-level mathematical functions to operate on these arrays including mathematical, logical, shape manipulation, sorting, selecting, I/O, discrete Fourier transforms, basic linear algebra, basic statistical operations, and much more; and the ability to wrap C/C++/Fortran code. At the core of the NumPy package, is the *ndarray* object, which allows us to do the vector programming. NumPy arrays are by far more efficient than the lists in Python. Numpy supports *array slicing*, with which arrays can be modified, without any extra computational cost.

SciPy

Numpy is focused on the *ndarray* and associated vector operations as well as some advanced mathematical functions. Scipy is another open source Python library which extends the possibility of Numpy in order to perform operations such as optimization, linear algebra, integration, interpolation, special



functions, FFT, signal and image processing, ODE solvers and other tasks common in science and engineering. SciPy is built on the Numpy array framework and takes scientific programming to a whole new level by supplying advanced mathematical functions. Documentation and download are available at <http://www.scipy.org/> [49].

MATPLOTLIB

matplotlib is a library for making 2D plots of arrays in Python. Although matplotlib is written primarily in pure Python, it makes heavy use of NumPy and other extension code to provide good performance even for large arrays. *Matplotlib* makes plotting simple, fast and convenient for interactive visualization of the Python programs.

2.2.9 IMPLEMENTATION : MULTIPROCESSING

As explained in the introduction, CPUs with multiple cores has almost become obligatory in most of the modern computers. Nowadays we can see multicore processors even on mobile phones. However, for a single program, these multicores usually won't run together at the same time. In order to achieve full usage of all the available cores, we rely on the multiprocessing module of Python.

In the scientific community, researchers often come across a problem wherein which they have to apply a specific formula on a huge amount of independent data. In parallel computing, this kind of problem is referred to as *embarrassingly parallel problems*, where we need very little or no effort to split the problem into a number of parallel tasks. multiprocessing module tackles this problem by taking advantage of the multiple cores present inside the computer by spawning different processes.

In the following, the overview of multiprocessing methodology and its functioning are presented. multiprocessing consists of different classes assigned to perform different tasks. Let us consider a simple scientific example of the type *embarrassingly parallel* in order to compute a sine function.

```
import multiprocessing as mp
import random
from numpy import *
from scipy import math, linspace
from numpy import zeros
def func(x,out):
    res = (sin(x)/x)**2
    return out.put(res)
```

```
Nprocs = 8 #Define the number of processors #mp.cpu_count() for maximum
N = 100000 #size of the array
x = linspace(-2*pi, 2*pi, N)
```



```

res = zeros(((size(x)/Nprocs), Nprocs), dtype = 'float')
out = mp.Queue()
jobs = []
for i in range(Nprocs-1):
    p = mp.Process(target=func, args=(x[i*N/Nprocs:(i+1)*N/Nprocs:], out))
    jobs.append(p)
    p.start()

for i in range(Nprocs-1):
    res[:,i] = out.get()
p.join()

final_result = zeros((size(x)/Nprocs), dtype = 'float')

for i in range(Nprocs):
    final_result = out.get()
p.join()

for i in range(Nprocs-1):
    if i == -1:
        final_result = res[:, i]
    else:
        final_result = concatenate((final_result, res[:, i]))

```

The above problem calculates $\sin^2(x)/x^2$ for N different values of x by using $Nprocs$ number of processors. `mp.cpu_count()` will give the output of the number of processors present in the computer. Most of the modern computers contain at least 4 processors. For instance, instead of performing a computation on 10000 values using one processor, we split the calculation between 4 processors and run simultaneously using multiprocessing. This is going to accelerate the computation substantially.

In the above program, 2 different classes of multiprocessing are used, namely, `multiprocessing.Process` and `multiprocessing.Queue`. The function to calculate the $\sin^2(x)/x^2$ is defined in the first part of the program. In the second part, we have initiated a `Process` object with the assigned function with arguments as N and `out` respectively. The `Process` class will not initiate until it reaches the step `p.start()`. The process will then run and return its result. Finally, the process completes via `p.join()`. Without the `p.join()`, the child process will be idle and not terminate, becoming a zombie which we must later kill manually.

Processes share nothing and they only communicate between different processes by using interprocess communication channel. To accomplish a communication, we use `multiprocessing.Queue`. `Queue` objects are, like the name says, a thread/process safe, First In First Out (FIFO) data structure queue. It



is used to establish a connection between different processes. They can store any pickle-able (serialized) Python object and the usage is easy. Queues are especially useful when passed as a parameter to a `Process` target function to enable the `Process` to intake or retrieve data. The above program is tested for a different number of processors and is plotted in figure (2.2.10 a). It shows a straightforward speedup as the array size increases. Since this is just a simple function, we can see the speedup of ~ 2 for 2 processors, ~ 3.5 for 4 processors, and ~ 6 for 8 processors compared to a single processor. The slight decrease in speedup for 8 processors comes from the fact that the computation is so weak, as the number of floating point operations are very few. So the program consumes more time to create the process and gather the data than to perform the actual computation. `multiprocessing` delivers a better speedup for more complex operations.

MULTIPROCESSING.POOL

`multiprocessing.Pool()` is another more convenient approach from the `Multiprocessing` module for simple parallel tasks. The job of this class is to manage a fixed number of workers and distribute the work between workers independently. The output return values from different jobs are then collected and returned as a list. The main advantage of using this class is that it is easy to implement and we don't have to worry about managing the queues, processes etc. The pool arguments include the number of processes and a function to run when starting the task process (invoked once per child). There are four methods in this module:

- *Pool.apply*
- *Pool.map*
- *Pool.apply_async*
- *Pool.map_async*

Here only `Pool.map` is discussed since the differences between the different methods are subtle. The `Pool.apply` and `Pool.map` methods are basically equivalents to Python's in-built `apply` and `map` functions. Given below is the example to calculate $\sin^2(x)/x^2$ using `Pool.map`.

```
import multiprocessing as mp
from multiprocessing import Pool
Nprocs = mp.cpu_count()
def func(x):
    return (math.sin(x))*(math.sin(x))/(x*x)

pool = mp.Pool(processes=Nprocs)
results = pool.map(func, range(1,10))
print(results)
```



`Pool.map` breaks the iteration into different parts which is submitted to the process pool as separate tasks. So it takes advantage of all the processes in the pool. `Pool.map` returns the result in an order corresponding to the order of the arguments.

Though `Pool.map` looks relatively simpler compared to `multiprocessing.Process`, it provides limited control over the data. Using `multiprocessing.Process`, we can have absolute control over the data which is sent to different processors.

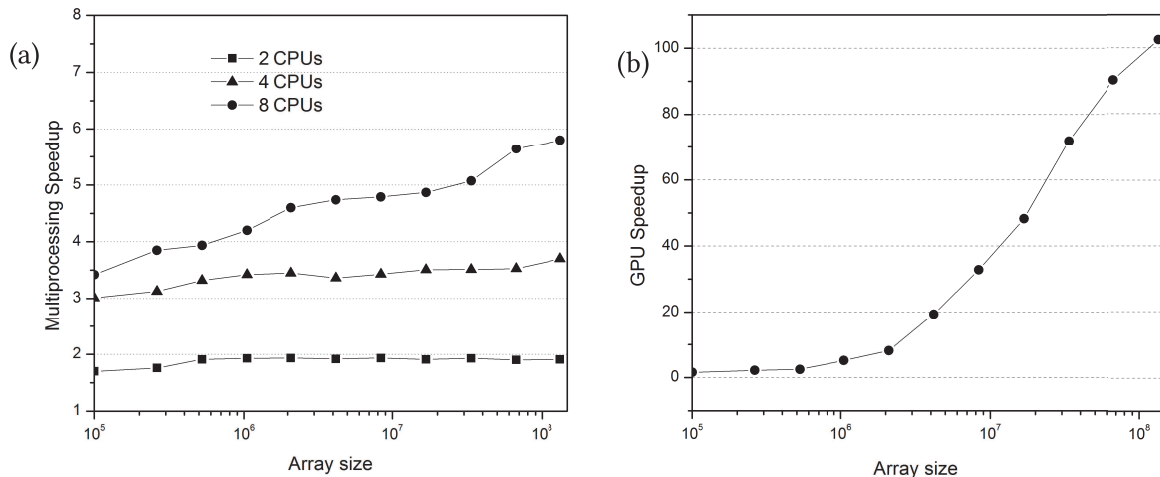


Figure 2.2.10: (a) Multiprocessing Speedup plotted for different number of processors vs total array size (b) Speedup obtained by GPU with respect to a single core processor

2.2.10 IMPLEMENTATION : GPU COMPUTING

GPU computing is another way of accelerating the program by using graphics cards as general-purpose GPUs. The GPU parallelism is advantageous provided that

- Computational requirements are large : There should be sufficient amount of operations in the calculation. Ample acceleration can be obtained for a fairly complex computations.
- Substantial Parallelism : Operation of same function on a large amount of independent data.
- Less Memory transfer : The number of memory transfers has to be minimal, as the amount of time taken for memory transfer highly impact the resulting speedup.

GPU computing is performed using PyCUDA, a Python wrapper to NVIDIA's CUDA [50]. The most common functions such as sin, cos, exp, log, square root etc, are highly optimized for GPUs. Here we give a glimpse on the basic code needed to initiate CUDA and use the same sample example which was used in multiprocessing.



```
import numpy
from pycuda import cumath
```

In order to send the data and retrieve from GPU, we need to import `gpuarray` module and also CUDA driver API root and context creation function.

```
import pycuda.driver as cuda
from pycuda.tools import make_default_context
import pycuda.gpuarray as gpuarray
import pycuda.autoinit
```

Subsequently, CUDA must be initialized before starting any CUDA functions. By default, `cumath` will use existing context, but there are also many other possibilities. Stream creation is optional and if we don't provide any stream, PyCUDA will create one on its own. The function definition in this case is very similar to that of `multiprocessing` except that PyCUDA uses `cumath` instead of the SciPy `math` function.

```
N = 10000
x = linspace(0, 2*pi, N+1)
def gpu_func(x):
    x_gpu = gpuarray.to_gpu(x) #Array transferred to GPU
    eqn = (pycuda.cumath.sin(x_gpu))*(pycuda.cumath.sin(x_gpu))/x_gpu*x_gpu
    return eqn
```

Last step is releasing CUDA context :

```
context.pop()
```

The above program was run on the NVIDIA Quadro K4000 GPU, and for the array size similar to that of the previous `multiprocessing` example. The graph (2.2.10 b) shows a speedup of ~ 100 for the array size of 10^8 . It is evident that GPU parallelism is efficient only for large size arrays. The methodology is very similar even in the case of PyOpenCL and can be found in the manual [51]. PyOpenCL is a Python wrapper to OpenCL, which is similar to CUDA but can be used for NVIDIA, as well as for GPUs from other companies, mainly AMD.

2.3 CONCLUSION

The main focus of this chapter was to present all the experimental techniques and computational tools which will be used in the following chapters for the comprehensive study of cubic zirconia under ion irradiation. Ion beam accelerators from the laboratories of France and Brazil were used to irradiate the YSZ



sample. The irradiated samples were studied under X-ray diffraction and RBS/C techniques. The XRD $\theta - 2\theta$ scans will be analysed in the Chapter 3 and the reciprocal space maps in the Chapter 4. In the second part of this chapter, computational techniques are required to build a model to calculate the diffuse X-ray scattering. In order to overcome the massive amount of computational time and memory for the calculation, we have programmed using heterogeneous parallel computing. GPU parallel computing, which is relatively new in the field of materials science is well-documented. The model is built using Python programming language with *multiprocessing* module for CPU parallel computing and CUDA programming for GPU computations. With the help of a simple example, it is demonstrated that parallel computing is a powerful approach to accelerate *embarrassingly parallel* calculations. The next chapter focuses on the results obtained by using all the experimental techniques presented in this chapter.



REFERENCES

- [1] Y. Serruys, M.-O. Ruault, P. Trocellier, S. Henry, O. Kaitasov, and P. Trouslard, “Multiple ion beam irradiation and implantation: JANNUS project,” *Nuclear Instruments and Methods in Physics Research Section B: Beam Interactions with Materials and Atoms*, vol. 240, no. 1, pp. 124–127, 2005.
- [2] J. F. Ziegler and J. P. Biersack, “The stopping and range of ions in matter,” in *Treatise on Heavy-Ion Science*, pp. 93–129, Springer, 1985.
- [3] W.-K. Chu, J. W. Mayer, and M.-A. Nicolet, “Backscattering spectroscopy,” 1978.
- [4] J. Tesmer, M. Nastasi, J. Barbour, C. Maggiore, and J. Mayer, “Handbook of modern ion beam materials analysis (pittsburgh, pa: Materials research society),” 1995.
- [5] W. Brandt, “Channeling in crystals,” *Scientific American*, vol. 218, no. 3, pp. 90–98, 1968.
- [6] L. Nowicki, A. Tuross, R. Ratajczak, A. Stonert, and F. Garrido, “Modern analysis of ion channeling data by monte carlo simulations,” *Nuclear Instruments and Methods in Physics Research Section B: Beam Interactions with Materials and Atoms*, vol. 240, no. 1, pp. 277–282, 2005.
- [7] M. Birkholz, *Thin film analysis by X-ray scattering*. John Wiley & Sons, 2006.
- [8] A. Debelle and A. Declémy, “XRD investigation of the strain/stress state of ion-irradiated crystals,” *Nuclear Instruments and Methods in Physics Research Section B: Beam Interactions with Materials and Atoms*, vol. 268, no. 9, pp. 1460–1465, 2010.
- [9] G. E. Moore, “Cramming more components onto integrated circuits, electronics, volume 38, number 8, april 19, 1965,” *Also available online from <ftp://download.intel.com/research/silicon/-moorepaper.pdf>*, 1965.
- [10] D. C. Brock and G. E. Moore, *Understanding Moore’s law: four decades of innovation*. Chemical Heritage Foundation, 2006.
- [11] A. Danowitz, K. Kelley, J. Mao, J. P. Stevenson, and M. Horowitz, “CPU DB: Recording micro-processor history,” *Commun. ACM*, vol. 55, pp. 55–63, Apr. 2012.
- [12] M. Hilbert and P. López, “The world’s technological capacity to store, communicate, and compute information,” *science*, vol. 332, no. 6025, pp. 60–65, 2011.
- [13] K. Asanovic, R. Bodik, B. C. Catanzaro, J. J. Gebis, P. Husbands, K. Keutzer, D. A. Patterson, W. L. Plishker, J. Shalf, S. W. Williams, *et al.*, “The landscape of parallel computing research: A view from



- berkeley,” tech. rep., Technical Report UCB/EECS-2006-183, EECS Department, University of California, Berkeley, 2006.
- [14] A. R. Brodtkorb, C. Dyken, T. R. Hagen, J. M. Hjelmervik, and O. O. Storaasli, “State-of-the-art in heterogeneous computing,” *Scientific Programming*, vol. 18, no. 1, pp. 1–33, 2010.
- [15] G. Taylor, “Energy efficient circuit design and the future of power delivery,[conference presentation],” *Electrical Performance of Electronic Packaging and Systems*, 2009.
- [16] H. Sutter and J. Larus, “Software and the concurrency revolution,” *Queue*, vol. 3, no. 7, pp. 54–62, 2005.
- [17] M. Herlihy and V. Luchangco, “Distributed computing and the multicore revolution,” *ACM SIGACT News*, vol. 39, no. 1, pp. 62–72, 2008.
- [18] S. Le Grand, A. W. Götz, and R. C. Walker, “SPFP: Speed without compromise—a mixed precision model for GPU accelerated molecular dynamics simulations,” *Computer Physics Communications*, vol. 184, no. 2, pp. 374–380, 2013.
- [19] M. Zheng, X. Li, and L. Guo, “Algorithms of GPU-enabled reactive force field (ReaxFF) molecular dynamics,” *Journal of Molecular Graphics and Modelling*, vol. 41, pp. 1–11, 2013.
- [20] C.-M. Liu, T. Wong, E. Wu, R. Luo, S.-M. Yiu, Y. Li, B. Wang, C. Yu, X. Chu, K. Zhao, *et al.*, “Soap3: ultra-fast GPU-based parallel alignment tool for short reads,” *Bioinformatics*, vol. 28, no. 6, pp. 878–879, 2012.
- [21] P. Tahmasebi, M. Sahimi, G. Mariethoz, and A. Hezarkhani, “Accelerating geostatistical simulations using graphics processing units (GPU),” *Computers & Geosciences*, vol. 46, pp. 51–59, 2012.
- [22] X. Wu, A. Koslowski, and W. Thiel, “Semiempirical quantum chemical calculations accelerated on a hybrid multicore CPU–GPU computing platform,” *Journal of Chemical Theory and Computation*, vol. 8, no. 7, pp. 2272–2281, 2012.
- [23] J. D. C. Maia, G. A. Urquiza Carvalho, C. P. Manguera Jr, S. R. Santana, L. A. F. Cabral, and G. B. Rocha, “GPU linear algebra libraries and GPGPU programming for accelerating mopac semiempirical quantum chemistry calculations,” *Journal of Chemical Theory and Computation*, vol. 8, no. 9, pp. 3072–3081, 2012.
- [24] A. Eklund, P. Dufort, D. Forsberg, and S. M. LaConte, “Medical image processing on the GPU—past, present and future,” *Medical image analysis*, vol. 17, no. 8, pp. 1073–1094, 2013.
- [25] Y. Otake, M. Armand, R. S. Armiger, M. D. Kutzer, E. Basafa, P. Kazanzides, and R. H. Taylor, “Intraoperative image-based multiview 2D/3D registration for image-guided orthopaedic



- surgery: incorporation of fiducial-based c-arm tracking and gpu-acceleration,” *Medical Imaging, IEEE Transactions on*, vol. 31, no. 4, pp. 948–962, 2012.
- [26] X. L. Dean-Ben, A. Ozbek, and D. Razansky, “Volumetric real-time tracking of peripheral human vasculature with GPU-accelerated three-dimensional optoacoustic tomography,” *Medical Imaging, IEEE Transactions on*, vol. 32, no. 11, pp. 2050–2055, 2013.
- [27] D. S. Smith, J. C. Gore, T. E. Yankeelov, and E. B. Welch, “Real-time compressive sensing MRI reconstruction using GPU computing and split bregman methods,” *International journal of biomedical imaging*, vol. 2012, 2012.
- [28] F. Heymann and R. Siebenmorgen, “GPU-based monte carlo dust radiative transfer scheme applied to active galactic nuclei,” *The Astrophysical Journal*, vol. 751, no. 1, p. 27, 2012.
- [29] X. Jia, J. Schümann, H. Paganetti, and S. B. Jiang, “GPU-based fast monte carlo dose calculation for proton therapy,” *Physics in medicine and biology*, vol. 57, no. 23, p. 7783, 2012.
- [30] M. J. Kilgard, “The opengl utility toolkit (glut) programming interface API version 3. silicon graphics,” *Inc., Nov*, vol. 13, 1996.
- [31] J. Sanders and E. Kandrot, *CUDA by example: an introduction to general-purpose GPU programming*. Addison-Wesley Professional, 2010.
- [32] “Web of Science is an online subscription-based scientific citation indexing service maintained by thomas reuters, which provides a comprehensive citation search.” <http://thomsonreuters.com/en/products-services/scholarly-scientific-research/scholarly-search-and-discovery/web-of-science.html>.
- [33] S. A. Manavski and G. Valle, “Cuda compatible GPU cards as efficient hardware accelerators for smith-waterman sequence alignment,” *BMC bioinformatics*, vol. 9, no. Suppl 2, p. S10, 2008.
- [34] G. Vasiliadis, S. Antonatos, M. Polychronakis, E. P. Markatos, and S. Ioannidis, “Gnort: High performance network intrusion detection using graphics processors,” in *Recent Advances in Intrusion Detection*, pp. 116–134, Springer, 2008.
- [35] M. C. Schatz, C. Trapnell, A. L. Delcher, and A. Varshney, “High-throughput sequence alignment using graphics processing units,” *BMC bioinformatics*, vol. 8, no. 1, p. 474, 2007.
- [36] M. J. Flynn, “Some computer organizations and their effectiveness,” *Computers, IEEE Transactions on*, vol. 100, no. 9, pp. 948–960, 1972.
- [37] R. Duncan, “A survey of parallel computer architectures,” *Computer*, vol. 23, no. 2, pp. 5–16, 1990.



- [38] M. J. Flynn, “Very high-speed computing systems,” *Proceedings of the IEEE*, vol. 54, no. 12, pp. 1901–1909, 1966.
- [39] M. Schmeisser, B. C. Heisen, M. Luettich, B. Busche, F. Hauer, T. Koske, K.-H. Knauber, and H. Stark, “Parallel, distributed and GPU computing technologies in single-particle electron microscopy,” *Acta Crystallographica Section D: Biological Crystallography*, vol. 65, no. 7, pp. 659–671, 2009.
- [40] M. J. Flynn and K. W. Rudd, “Parallel architectures,” *ACM Computing Surveys (CSUR)*, vol. 28, no. 1, pp. 67–70, 1996.
- [41] C. A. Navarro, N. Hitschfeld-Kahler, and L. Mateu, “A survey on parallel computing and its applications in data-parallel problems using gpu architectures,” *Communications in Computational Physics*, vol. 15, no. 2, pp. 285–329, 2014.
- [42] M. Flynn, “Flynn’s taxonomy,” in *Encyclopedia of Parallel Computing*, pp. 689–697, Springer, 2011.
- [43] M. J. Atallah, *Algorithms and theory of computation handbook*. CRC press, 2002.
- [44] G. M. Amdahl, “Validity of the single processor approach to achieving large scale computing capabilities,” in *Proceedings of the April 18-20, 1967, spring joint computer conference*, pp. 483–485, ACM, 1967.
- [45] M. T. Heath, “A tale of two laws,” *International Journal of High Performance Computing Applications*, p. 1094342015572031, 2015.
- [46] J. L. Gustafson, “Reevaluating amdahl’s law,” *Communications of the ACM*, vol. 31, no. 5, pp. 532–533, 1988. cited By 370.
- [47] G. van Rossum, “Scripting the web with python,” *World Wide Web J.*, vol. 2, pp. 97–120, Apr. 1997.
- [48] S. Van Der Walt, S. C. Colbert, and G. Varoquaux, “The NumPy array: a structure for efficient numerical computation,” *Computing in Science & Engineering*, vol. 13, no. 2, pp. 22–30, 2011.
- [49] E. Jones, T. Oliphant, P. Peterson, *et al.*, “SciPy: Open source scientific tools for Python,” 2001–. [Online; accessed 2015-07-07].
- [50] A. Klöckner, N. Pinto, Y. Lee, B. Catanzaro, P. Ivanov, and A. Fasih, “PyCUDA and pyopenCL: A scripting-based approach to GPU run-time code generation,” *Parallel Computing*, vol. 38, no. 3, pp. 157–174, 2012.
- [51] “PyFFT for PyCuda and PyOpenCL.” <https://pythonhosted.org/pyfft/>.



3

Strain and damage build-up in Au-irradiated zirconia

3.1 INTRODUCTION

IN THIS CHAPTER, Au-irradiated yttria-stabilized zirconia (YSZ) is investigated under various conditions and with different techniques. As previously detailed in the first chapter, YSZ is predicted to be used as an inert matrix for the transmutation of radiotoxic actinides. Furthermore, YSZ has an advantage of being easily available and non-radioactive and also its isostructural property with urania (UO_2), thoria (ThO_2) and plutonia (PuO_2) makes the material interesting for the study of its properties under irradiation conditions. Ion irradiation is used as a tool to simulate different irradiation conditions. The strain and damage build-ups are determined with the help of X-ray diffraction. The determination of atomic displacements from the XRD data is limited by the so-called *phase problem*. In the first part of the chapter, the simulation procedure involved in overcoming the phase problem and the extraction of the strain and damage profiles from the X-ray data is presented. In the second part, the results obtained from the simulation of X-ray diffraction curves are elucidated. The results from the RBS/C method are detailed in the final section of the chapter.

3.2 SIMULATION PROCEDURE

There exists several methods in order to simulate the XRD curves to extract the depth dependent profiles of the ion-irradiated materials. But the determination of these profiles from XRD data is hindered by

the so-called *phase problem*. Previously on the first chapter, we have seen that the atomic displacements affect the phase of the diffracted amplitude E (equation 1.23). But in an actual XRD experiment, only the intensity EE^* can be measured. Consequently, the phase, hence the information regarding atomic displacements is partly lost in the diffraction experiment.

Over the years different theoretical and experimental approaches have been proposed and utilized to retrieve the phase information [1] [2] [3] [4]. One of such methods is the Gerchberg and Saxton (GS) iterative procedure [4] [5] [6]. GS method performs an iterative Fourier transformation back and forth between the object and Fourier domains and inserts the measured data in each domain [7]. The algorithm is given below. Firstly, a random set of phases are considered. Later, in the iteration loop

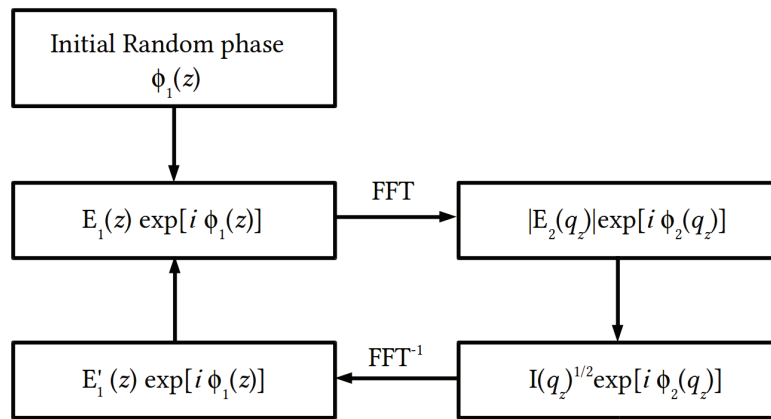


Figure 3.2.1: Illustration of the Gerchberg - Saxton algorithm.

it switches between real and reciprocal space using a fast Fourier transform (FFT) and the inverse FFT. The amplitudes are updated at the end of each loop. In the real space, the amplitude $E_1(z)$ is submitted to physically plausible constraints (positivity, support, *etc*) and in the reciprocal space, the amplitude $|E_2(q_z)|$ is changed to the experimentally measured value. After a number of iterations, the algorithm converges to a value of the phase that satisfies both constraints in real and reciprocal space [8]. Another method of phase retrieval of the X-ray wave diffracted by a single crystal under Bragg condition is by using logarithmic dispersion method [3] [9]. But these methods are difficult to apply in our materials mainly because the GS iterative method is based on the Fourier transform and it therefore implicitly assumes the kinematical theory of diffraction. This method is very useful for nano materials where the kinematical theory holds [10] [11]. But in the case of irradiated materials, the diffraction profile consists of multiple peaks, including the strong diffraction from the substrate which has to be treated with the dynamical theory.

Another alternative method is based on fitting the Takagi-Taupin equations (equation 1.44) where the displacement is described by a specific model. The model is built by dividing the crystal layer into different lamellas with constant strain e_z and Debye-Waller (DW) [12] [13]. There exists a simple analytical solution for each lamella and the Takagi-Taupin equations [14] [15] can be solved recursively in this

approximation [16] [17]. The structure factor in each layer is constant but is multiplied by a static DW factor to take into account the effect of lattice disorder consecutive to implantation [13]. This approach implies that a large number of parameters have to be refined. For instance, if the crystal is divided into 100 lamellas, there exists minimum 200 parameters to refine. This brings in the need of applying constraints on the lamellas. One way to constrain is by assuming that the strain profile follows an arbitrary functional form, *i.e.* a polynomial or a gaussian. Here, we rely on the method developed by Boule *et.al* which uses cubic B-spline functions to model the strain $e(z)$ and damage profiles, $DW(z)$ [18] [19] [20].

The effects of atomic displacements can be phenomenologically divided into two categories (i) non-random displacements, which correspond to lattice strains $e(z)$, and (ii) random displacements which can be characterized by the root-mean-squared atomic displacements $\langle u(z)^2 \rangle^{1/2}$. Lattice strain is written as

$$e(z) = \frac{a(z) - a_{YSZ}}{a_{YSZ}} \quad (3.1)$$

where $a(z)$ is the lattice parameter at depth z and a_{YSZ} is the lattice parameter of virgin YSZ. Lattice strains correspond to a change in the lattice parameters and therefore only give rise to a shift of the diffraction peaks emanating from the strained region.

In ion-irradiated crystals, a significant fraction of the atoms may be displaced from lattice positions. The statistical distribution of displacements \mathbf{u}_j away from lattice site j is described by a function $\rho(\mathbf{u}_j)$. Such a distribution results in a mean structure factor. From (equation 1.16)

$$\langle F_H \rangle = \int d^3u \rho(\mathbf{u}_j) \sum_j f_j \exp[-i\mathbf{Q}(\mathbf{r}_j + \mathbf{u}_j)] \quad (3.2)$$

where f_j is the atomic scattering factor for site j , located at \mathbf{r}_j in undamaged crystal. If ρ is assumed to be a spherically symmetric Gaussian distribution for all sites, the mean structure factor becomes

$$\langle F_H \rangle = \exp\left(-\frac{1}{2}\mathbf{Q}^2\langle u(z)^2 \rangle\right) F_H^0 \quad (3.3)$$

where F_H^0 is the structure factor from the undamaged part of the crystal. From the above equation, the DW factor is defined as

$$DW(z) = \exp\left(-\frac{1}{2}Q^2\langle u(z)^2 \rangle\right) \quad (3.4)$$

where Q is the magnitude of the scattering vector $\mathbf{Q} = 4\pi \sin \theta / \lambda$. A perfect (defect-free) crystal is characterized by a $DW = 1$, whereas a highly defective, or an amorphous material, will have a $DW = 0$. In the above equation (3.2), ρ is assumed to be Gaussian and this could only hold good in two cases. Either the displacements are actually gaussian or otherwise, it can be explained in the framework of central limit theorem. The theorem states that the probability distribution of the average of the independent random variables with finite variance approaches a Gaussian distribution. This means that the displacement of



an atom at site j results from the sum of all displacements in the whole crystal. If this is random and has finite variables, it assumes a gaussian distribution. It has to be noted that in the case of displacement cascades occurring in irradiated materials, very large displacements from the average atomic position can be encountered, so that the finite variance condition might be unjustified. The central limit theorem fails to account for XRD profiles exhibiting for instance, power law type tails. Hence removing the finite variance condition leads to the so-called *generalized central limit theorem* which states that the sum of identically distributed random variables converges to the Lévy-stable distribution [21] [22]. This distribution accounts for a wide range of shapes usually encountered in practice. Symmetrical Lévy-stable distribution allows the DW factor to be written in a simple form as [23]

$$DW(z) = \exp\left(-\frac{1}{2}|Q|^\gamma \sigma_u^\gamma\right) \quad (3.5)$$

where γ is the tail index, that determines the shape of the displacement distribution function, and σ_u is the *characteristic width* of the distribution. It can be noted that $\gamma = 2$ corresponds to a Gaussian, and $\gamma = 1$ to a Lorentzian distribution. In the following, the functions $e(z)$ and $DW(z)$ are modelled with cubic B-splines. It should be mentioned that thermal vibrations also contribute to lower the diffracted amplitude through the term given by equation (3.5) (except that the average $\langle \dots \rangle$ is a time average). In order to disentangle both contributions, the Bragg peak of the unirradiated part of the crystal is used as an intensity reference, so that in the following simulations the sole static disorder is refined.

3.3 CUBIC B-SPLINES

The strain and damage profiles are described with the help of cubic B-spline (basis spline) function. Spline functions are a piecewise-defined polynomial functions. Cubic B-spline consists of a polynomial of the order 3 and is the most commonly used splines.

Given a set of knots $x_i (i = 1, 2, \dots, N)$, a spline function of degree m , $S_m(x)$, is such that $S_m(x)$ is a polynomial of degree m in each x_i, x_{i+1} interval, and has $m - 1$ continuous derivatives over the whole x range [24]. In the B-spline representation, any spline function can be written as [25]

$$S_m(x) = \sum_{i=1}^N w_i B_{i,m}(x) \quad (3.6)$$

where w_i is the weight of the i th B-spline of degree m , $B_{i,m}(x)$. Any spline function is therefore entirely determined by a set of N discrete weights. The basis functions are defined as successive convolutions of step functions [26]

$$B_{i,m}(x) = \underbrace{B_{i,0}(x) * B_{i,0}(x) * \dots * B_{i,0}(x)}_{m+1 \text{ times}} \quad (3.7)$$



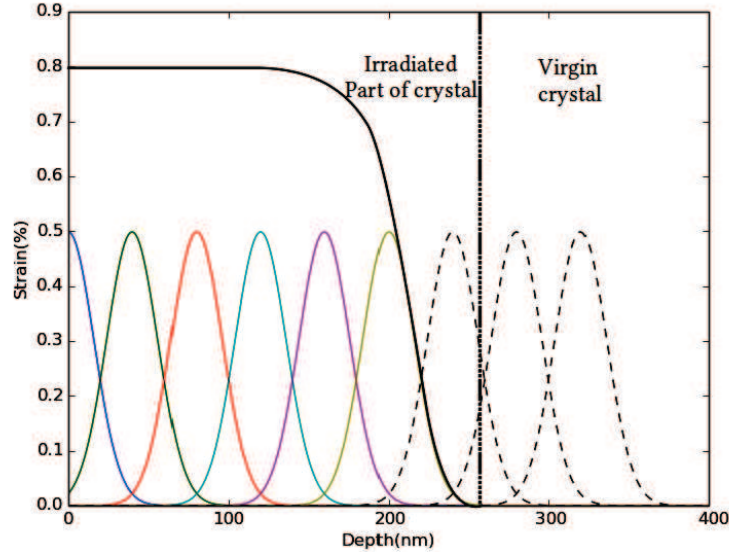


Figure 3.3.1: Illustration of strain profile (thick black line) calculated with six nonzero basis functions (in color). The weight w of each basis function is taken to be equal to 0.8. The weight of the last three basis functions (dotted curves) is fixed to zero in order to ensure a smooth transition from the implanted region to the virgin region of the crystal.

with base cases

$$B_{i,0}(x) = \begin{cases} 1 & \text{if } 0 \leq x \leq 1 \\ 0 & \text{otherwise} \end{cases} \quad (3.8)$$

For the case of cubic B-spline ($m = 3$), the basis functions are

$$B_{0,3}(x) = \begin{cases} \frac{1}{6}x^3 & \text{if } x \in [0, 1] \\ \frac{1}{6}(-3x^3 + 12x^2 - 12x + 4) & \text{if } x \in [1, 2] \\ \frac{1}{6}(3x^3 - 24x^2 + 60x - 44) & \text{if } x \in [2, 3] \\ \frac{1}{6}(4 - x)^3 & \text{if } x \in [3, 4] \\ 0 & \text{otherwise} \end{cases} \quad (3.9)$$

and

$$B_{i,m}(x) = B_{0,m}(x - i) \quad (3.10)$$

Therefore, with the set of weights w_i , we can generate complete strain and damage profiles by means of equation (3.6). The degree of detail entirely depends on the number of knots. With less number of knots, the resulting strain profile is very smooth and might wipe out small details. On the other hand, if we have a large number of knots, the ability to render tiny features of $e(z)$ is high. But this leads to the possibility of the profile exhibiting unphysical oscillations during the simulation. So we need to find the balance in the number of knots in order to ensure that the strain profile is smooth enough and without any wild oscillations.

Moreover, during the simulation, in order to ensure the smooth transition from the irradiated region to

the virgin crystal, the weights of the last three B-splines are fixed to zero. Hence if N knots are used, the strain profile is actually divided into $N - 3$ equally sized regions. A representation of a strain profile defined by nine basis functions is given in figure (3.3.1). In this case, the crystal is divided into 6 equally sized regions and the last three weights are fixed to zero. All weights were taken to be equal to 0.5 in figure (3.3.1), so that, in the implanted region (ignoring the transition zone), the strain is constant and is equal to 0.8%.

These basis functions have restricted support; we hence have local control over the overall curve. This property is also very appropriate for implementation in a non-linear least-square routine, as the w_i are almost uncorrelated. Finally, the main interest of these functions lies in their extremely high versatility as it is virtually possible to describe any shape, provided that the number of knots are sufficient. In practice, however, very few knots are necessary. During the simulations, we have used around 7 to 10 knots to describe the profiles. Overall, the properties of smoothness, minimum curvature and local control makes the cubic B-spline functions very well suited to model the lattice displacement profile in single crystals.

3.4 GENERALIZED SIMULATED ANNEALING

Generalized simulated annealing (GSA) is a search algorithm for the global minimization of a given function. The basic aspect of the simulated annealing method is analogous to metallurgy, wherein annealing a molten metal causes it to reach its crystalline state which is the global minimum in terms of energy. The simulated annealing algorithm was developed to simulate the annealing process with the objective of finding the global minimum of the given function and was described by Kirkpatrick *et. al.* [27] which holds good for classical systems. During the simulation, the objective function is treated as the energy function of molten metal and artificially, a temperature function is introduced and cooled gradually. It can be best illustrated with the help of figure (3.4.1). Here the goal is to reach the global minimum, which is at point 3. With a local search algorithm starting from S , we would reach point 1 or 2, and which is a local minimum. But it will be a problem if we have to get it over the hump after point 2 to find the global minimum at point 3. Using simulated annealing, it is possible to reach the global minimum. The algorithm follows the quasi-equilibrium Boltzmann-Gibbs statistics using a Gaussian visiting distribution, which we refer to as Classical Simulated Annealing(CSA) or Boltzmann machine.

To fit the experimental data with a calculated model, we use the following error function, which measures the difference between the experimental and the calculated curves [19] :

$$E = \sum_{i=1}^N [\log(I_i^{cal}) - \log(I_i^{obs})]^2 / N \quad (3.11)$$

where I_i^{cal} and I_i^{obs} are the calculated and observed intensities and N is the number of data points. The values of the error function for all possible values of the parameters of the model form a hypersurface



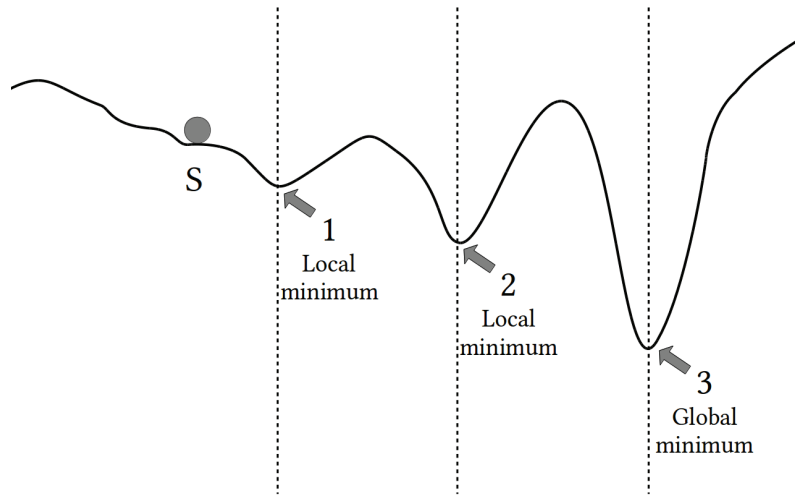


Figure 3.4.1: Illustration of the problem of finding the global minima.

with several maxima and minima. The aim of an optimization algorithm is to find the deepest minimum, which corresponds to the best possible agreement between the model and the experimental data.

In CSA, the algorithm performs the minimization by randomly exploring the hypersurface using a Gaussian visiting distribution. If \mathbf{x}_t is a N -dimensional vector that contains all parameters to be optimized, then the geometry for two consecutive steps is given by $\mathbf{x}_t = \mathbf{x}_{t-1} + \Delta\mathbf{x}$, where $\Delta\mathbf{x}$ is a vector of Gaussian random variables and t is the computing time (expressed in Monte Carlo steps, MCS). If the parameter jump is downhill (the error function is lowered, $\Delta E < 0$) the new configuration is accepted and constitutes the starting point for the next jump. If the jump is uphill (the error function is increased, $\Delta E > 0$) the jump might be accepted according to an acceptance probability, which, in the case of CSA, is the Boltzmann-Gibbs acceptance probability. This gives rise to the Metropolis criterion for the uphill jump acceptance [28] :

$$r \leq \exp[-\Delta E/T(t)] \quad (3.12)$$

where T is an artificial temperature and r is a uniform random number lying between 0 and 1. The possibility of uphill moves allows the algorithm to detrap from local minima. With increasing time, the temperature is decreased so that the uphill jump probability decreases and the system is hopefully in the close vicinity of the global minimum [27] [29]. Geman and Geman [30] showed that for a classical case, a necessary and sufficient condition for having the probability of reaching a global minimum is that the temperature decreases logarithmically with time. This means that, though CSA converges to a global minimum, the convergence is fairly slow [20] [31]. Much effort has therefore been directed towards increasing the convergence speed without increasing the probability of being trapped in a local minimum. Along this line an efficient algorithm, the GSA algorithm, has been proposed by Tsallis and Stariolo [29].

In the framework of GSA, generalized thermostatics [32] is used instead of the Boltzmann-Gibbs

statistics, so that the Gaussian visiting distribution is replaced with

$$g_{q_v}(\Delta \mathbf{x}) = \left(\frac{q_v - 1}{\pi} \right)^{D/2} \frac{\Gamma[1/(q_v - 1) + (D - 1)/2]}{\Gamma[1/(q_v - 1) - 1/2]} \quad (3.13)$$

$$\times \frac{[T(t)]^{-D/(3-q_v)}}{\{1 + (q_v - 1)(\Delta \mathbf{x})^2/[T(t)]^{2/(3-q_v)}\}^{1/(q_v-1)+(D-1)/2}}$$

where D is the number of fitting parameters (the dimension of the vector \mathbf{x}), Γ is the Gamma function and $q_v \in (1, 3)$ defines the shape of the distribution: for $q_v \rightarrow 1$ we obtain the Gaussian distribution, $q_v = 2$ corresponds to the Lorentzian distribution and for $q_v > 2$ we obtain 'super-Lorentzian' distributions exhibiting tails decreasing slower than $1/\Delta \mathbf{x}$. With such tails, the parameters occasionally perform very long jumps, which ensures a more efficient detrapping as compared to the Gaussian distribution and hence a faster convergence. The GSA algorithm implies the generation of random numbers $\Delta \mathbf{x}$ effectively obeying equation (3.13), *i.e.* Tsallis random numbers (instead of Gaussian random numbers). In this work we make use of the Tsallis random number generator proposed by Schanze (2006) [33] which produces random numbers obeying exactly equation (3.13).

$$\Delta \mathbf{x} = \mathbf{y}/(su^{1/2}) \quad (3.14)$$

where \mathbf{y} is a D -dimensional vector of Gaussian random variables, u is a random variable obeying the $\gamma(1, p)$ distribution, and the parameters p and s are given by

$$p = \frac{3 - q_v}{2(q_v - 1)} \text{ and } s = \frac{[2(q_v - 1)]^{1/2}}{T^{1/(3-q_v)}} \quad (3.15)$$

To implement equations (3.14) and (3.15), we use the default Gaussian and gamma random number generators from the *SciPy* library. At each computing step, a new random vector $\Delta \mathbf{x}$ is generated (using 3.14) and each parameter $x_i (i \in [1, D])$ is modified according to

$$x_{i,t} = x_{i,t-1} + \Delta x_i \quad (3.16)$$

Within the framework of GSA, the temperature cooling schedule is given by [29]

$$T(t) = T(0) \frac{2^{q_v-1} - 1}{(1+t)^{q_v-1} - 1} \quad (3.17)$$

The initial temperature $T(0)$ is chosen so that the jump for each parameter remains roughly within the range of acceptable values for each parameter. Each time x_i exceeds the range of acceptable values, a new Δx_i is generated using equation (3.14) and (3.15). Moreover, we have found that the efficiency of the algorithm is increased if the temperature is decreased stepwise, each step lasting 100 or even 1000 MCS. This allows the parameter space to be sufficiently explored for each temperature.



In GSA, a downhill jump is always accepted similar to CSA. An uphill jump is accepted only if the generalized Metropolis criterion is met

$$r \leq [1 + (q_a - 1)\Delta E/T(t)]^{1/(1-q_a)} \quad (3.18)$$

where $q_a \in (-\infty, 1)$ is the acceptance parameter and r is a uniform random number lying between 0 and 1. For $q_a < 1$ the uphill probability is set to 0 when $1 + (q_a - 1)\Delta E/T(t) < 0$ to ensure that the probability lies in the range $[0, 1]$. Here $q_v = q_a = 1$ corresponds to CSA and $q_v = 2q_a = 2$ (i.e. a Lorentzian visiting distribution combined with the classical Metropolis criterion) corresponds to the so-called *fast simulated annealing algorithm* [34]. It has been shown by earlier studies that convergence is faster for $q_a < 1$ [35].

A significant improvement of the GSA algorithm has been implemented by Xiang *et.al.* (1997)[31] in which they suggest to use a decreasing q_a instead of a constant q_a

$$q_a(t) = q_a(0) - \lambda t \quad (3.19)$$

where λ is a constant (0.85 in the present case). With this modification, for large computing times, the uphill acceptance probability is almost zero [equation (3.18)] so that GSA behaves as a steepest-descent-type algorithm.

In brief, the GSA algorithm can be summarized as follows [20]:

1. Given a set of parameters $[q_v, q_a(0)$ and $T(0)]$, generate a random vector of parameters \mathbf{x}_0 . Compute the corresponding error function E_0 [equation (3.11)].
2. Using equations (3.14) and (3.15), generate a random jump of parameters $\Delta \mathbf{x}$, compute \mathbf{x}_t [equation (3.16)] and the corresponding error function E_t [equation (3.11)].
3. If the jump is downhill ($E_t \geq E_{t-1}$), the new configuration is accepted only if the generalized Metropolis criterion is satisfied [equation (3.18)]. Otherwise, the configuration is rejected (i.e., keep the previous configuration \mathbf{x}_{t-1}).
4. Decrease T [equation (3.17)] and q_a [equation (3.19)] and return to step 2 until the maximum number of iterations is reached, $t = t_{max}$. The algorithm returns the parameters \mathbf{x}_t corresponding to the lowest error function encountered, $E_{t,min}$.

3.5 RESULTS

3.5.1 X-RAY DIFFRACTION

Yttria-stabilized zirconia was studied in detail by using XRD and we have extracted the strain and the damage profiles with the help of the simulation procedure discussed above. Irradiation of YSZ was done



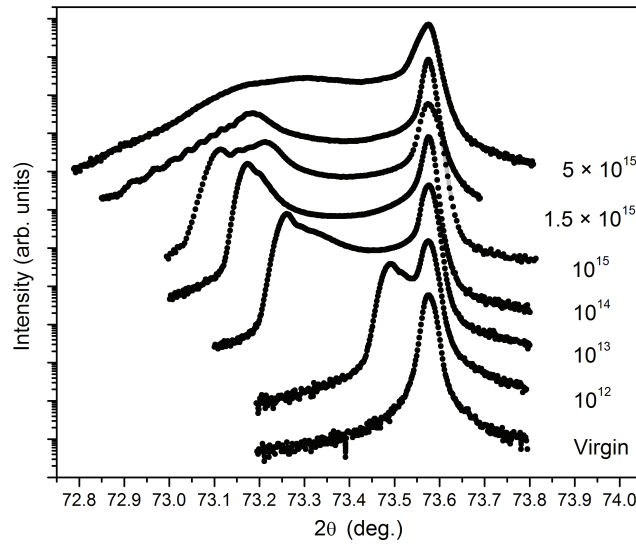


Figure 3.5.1: $\theta - 2\theta$ scans recorded in the vicinity of the (400) reflection for virgin and YSZ crystals irradiated at room temperature for increasing Au-ion fluences. The curves are shifted vertically for clarity.

under five different temperatures, namely, 80, 300, 573, 773 and 1073 K. For each temperature, samples were irradiated with 4 MeV Au^{2+} ions with fluences ranging from 10^{12} to $10^{16} cm^{-2}$. First, we consider the case of room temperature. The $\theta - 2\theta$ scans recorded in the vicinity of the (400) reflection for virgin and YSZ crystals irradiated at increasing Au-ion fluences are given in the figure (3.5.1). The XRD curves for all the fluences exhibit an intense narrow peak at $2\theta = 73.57^\circ$ which corresponds to the unirradiated part of the samples. The appearance of this peak was expected since the thickness probed by X-rays in this configuration ($4\mu m$ with the $1/e$ attenuation-length criterion) is greater than the damaged thickness $\sim 1\mu m$. The position of this peak will be used to determine the irradiation induced strain free lattice parameter of YSZ. The presence of a complex additional signal at smaller 2θ values indicates the existence of a dilatation gradient associated to the energy-deposition profile of Au^{2+} ions.

As the ion fluence increases, the signal from the damage region shifts towards lower angles, indicating an increase in the tensile strain in the direction normal to the surface of the samples. Additionally, decrease in the Bragg intensity can be clearly observed. The simulations of the XRD data were performed with the model described above and are shown in the figure (3.5.2). The simulation condition for the strain and the Debye-Waller profiles consists of six non-zero B-splines each. A maximum temperature was set in the initial conditions and the simulations were performed by finding the global minimum using general simulated annealing on a standard 1000 cycles. At the end of 1000 iterations with the progressive decrease in the temperature function, the program returned the parameters corresponding to the lowest error function encountered. It is evident from the figure (3.5.2) that the simulation results are close to

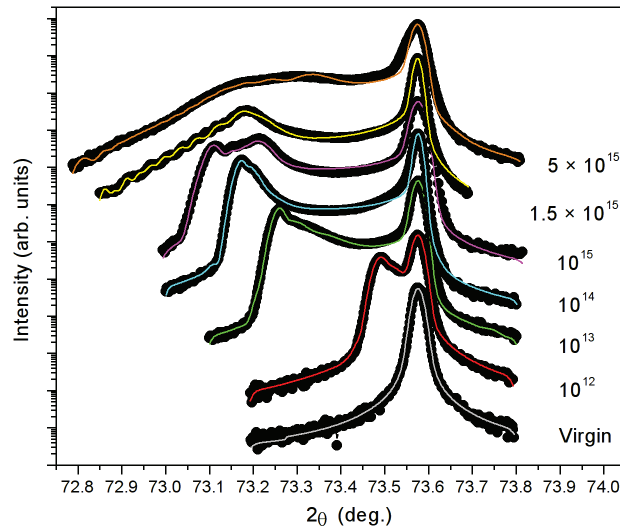


Figure 3.5.2: $\theta - 2\theta$ scans (black circles) and corresponding simulated curves (coloured lines) recorded in the vicinity of the (400) reflection for virgin and YSZ crystals irradiated at room temperature for increasing Au-ion fluences. The curves are shifted vertically for clarity.

perfect and all the details of the fringe structure of the diffraction profiles are very well rendered. These simulations enable us to extract the strain and the damage profiles and an excellent agreement with the experimental data strongly suggests that the resultant profiles are valid.

Figure (3.5.3) shows the strain and the Debye-Waller profiles obtained as a result of simulations for XRD curves irradiated at room temperature. First, we discuss the strain profiles which are presented in fig(3.5.3 a). As the ion fluence increases, it can be observed that the maximum strain level in the irradiated region increases. For the lowest fluence, it starts with 0.1% and it reaches values as high as 0.9% for the highest fluence. This is in agreement with the qualitative observation of the XRD data. Additionally, it can be observed that the width of the strained region increases with fluence. For the lowest fluence, the width of the strained region is around $0.75 \mu\text{m}$ whereas for the highest fluence, it is up to $1.5 \mu\text{m}$. Another interesting feature is that the depth of the maximum strain is shifted towards higher values. Since the statistical properties of the atomic displacements within the displacement cascades induced by irradiation is not precisely known, we shall not discuss the $\langle u(z) \rangle$ (or σ_u) and restrict ourselves to the analysis of the DW term. The Debye-Waller profiles are presented in fig (3.5.3 b). Similar to what is observed for the strain, the maximum damage level (*i.e.* minimum DW) in the irradiated region increases with fluence. In addition, the width of the damaged region increases with the increase in fluence. Interestingly, for high fluences, the position of the DW minimum coincides with the position of the maximum strain. In addition, for the last two fluences, *i.e.*, 1.5×10^{15} and $5 \times 10^{15} \text{cm}^{-2}$, the DW values are found to be very low (~ 0) which means that the crystal in these regions is highly defective

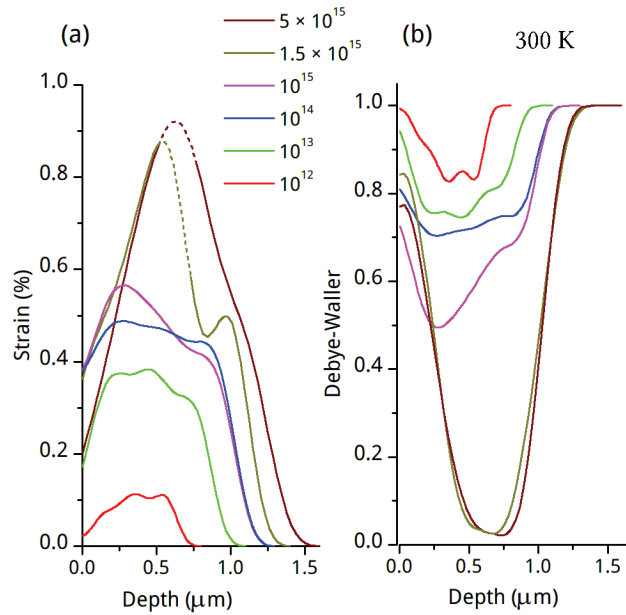


Figure 3.5.3: Strain (a) and the Debye-Waller profile (b) obtained after the simulation of the XRD curves displayed in (3.5.2) for 300 K.

(at least, as seen by XRD on the (400) reflection). Hence the corresponding strain values in this region cannot be reliably determined (as represented by dotted lines in figure 3.5.3). This behaviour will be further explained with the help of strain build-ups for all temperatures in the discussion section.

In the XRD curves (3.5.2), the shift in the signal from the damage region towards lower angles with the increase in ion fluence was previously analysed by *Moll et. al.* [36]. It has been shown that this also corresponds to an increase of the defect density and the formation of interstitial defects during irradiation might be at the origin of this lattice expansion [36]. The qualitative analysis indicated that as the fluence increases, more defects are created and correspondingly, the strain level increases. At a given strain level, the width of the strain profile increases with fluence. As it reaches higher fluence *i.e.* $1.5 \times 10^{15} \text{ cm}^{-2}$, the fringe pattern begins to vanish and the scattered intensity decreases. This can be attributed to the increase of random atomic displacements. Finally, for the highest fluence, *i.e.* $5 \times 10^{15} \text{ cm}^{-2}$, the scattered intensity decreases drastically indicating a strong increase of the random atomic displacements. Figure (3.5.4) displays the evolution of the maximum strain and damage as a function of the ion fluence. This figure is obtained by selecting the maximum physical strain (ϵ_N^{max}) and the minimum DW (DW^{min}) values in the profiles presented in figure (3.5.3). The kinetics exhibit a two-step behaviour. The slow rate of increase in the evolution of strain and damage up to a critical fluence (*i.e.* $1 \times 10^{15} \text{ cm}^{-2}$) is recorded. This is followed by a dramatic increase beyond this fluence. As explained in chapter 1, previous studies [36] [37] [38] revealed a strain relaxation in the second step, which is due to formation of extended defects. Here, since we have full strain profiles, we monitored the maximum strain for all fluences, but

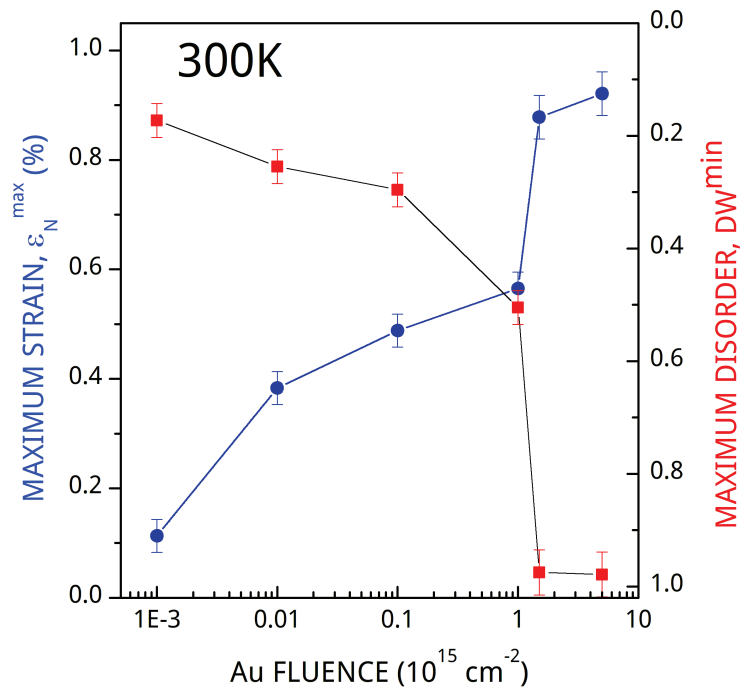


Figure 3.5.4: Variation of the maximum strain and damage levels as a function of the ion fluence irradiated at 300 K.

this later shifted towards the interface with the pristine region. The explanation of point defects rearrangement to form extended defects holds good for this case too, confirmed by DW close to zero.

$\theta - 2\theta$ scans (black circles) and the corresponding simulated curves (coloured lines) recorded in the vicinity of the (400) reflection for virgin and YSZ crystals irradiated at 80 K for increasing Au-ion fluences are given in figure (3.5.5). The simulations for 80 K were particularly challenging which is evident from the numerous fringes in the XRD curves. But with the efficient simulation program, we were able to tackle it and obtain nearly perfect fits. Starting from the lower fluence, the XRD curves exhibit fringes and the intensity of the damaged region moves towards lower angles. Then, the fringe pattern vanishes for the fluence $5 \times 10^{15} \text{ cm}^{-2}$ and the scattered intensity dramatically decreases, indicating a strong increase in random atomic displacements. Simulations were successful even for the highest fluence for which no fringe pattern is recorded. The corresponding strain and damage profiles are given in figure (3.5.6). For low fluences, the strain and damage profiles show a similar behaviour as that of room temperature. With the increase of ion fluence, the maximum strain level in the irradiated region and the width of the damage region increases. For the lowest fluence, the width of the strained region is around $0.8 \mu\text{m}$ whereas for the highest fluence, it is upto $1.75 \mu\text{m}$. Another interesting feature is that the depth of the maximum strain is shifted towards higher values. For the last fluence, for the depth upto $\sim 1 \mu\text{m}$, the strain profile exhibit unrealistic oscillations (shown as dotted lines). This behaviour can be under-



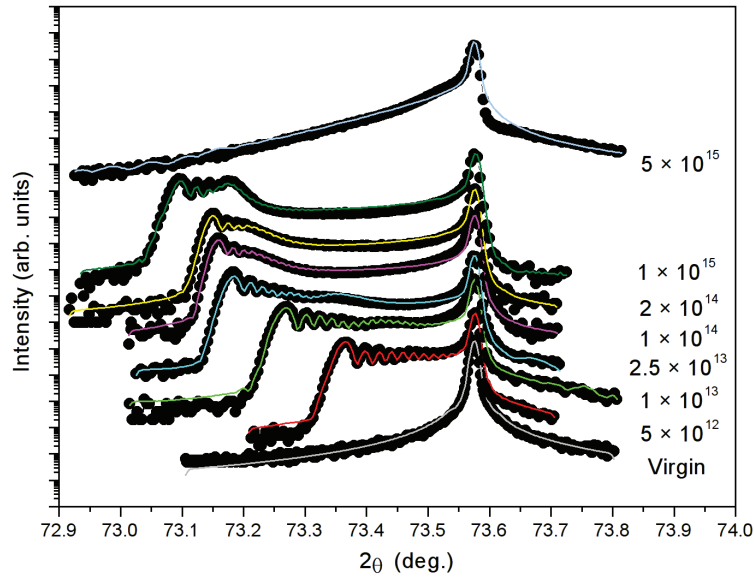


Figure 3.5.5: $\theta - 2\theta$ scans (black circles) and the corresponding simulated curves (coloured lines) recorded in the vicinity of the (400) reflection for virgin and YSZ crystals irradiated at 80 K for increasing Au-ion fluences. The curves are shifted vertically for clarity.

stood by the examination of the DW profiles displayed in fig (3.5.6b). Upon increasing fluence, as expected from the qualitative observation of the curves, we clearly observe an increase in the level of disorder (decrease of DW). Similarly to what is observed for the strain, the width of the damaged region increases with increasing fluence. Interestingly, for the highest fluence, the DW is close to 0 over a wide range of depth ($\sim 1 \mu\text{m}$). This finding indicates that the YSZ crystal in these regions is so defective that its diffracted Bragg intensity is close to 0, *i.e.* almost no X-rays are emitted from these regions in the symmetrical $\theta - 2\theta$ configuration. As a consequence, no physical strain value related to these regions can be obtained by XRD in this configuration. This simple observation explains the occurrence of an unphysical behaviour of the strain in these regions. The observed oscillations are due to the fact that the strain profile is bounded by the B-spline model that prevents the strain to diverge or exhibit abrupt variations during the fitting procedure.

Now we continue by discussing the case of high temperatures. Figures (3.5.7), (3.5.9) and (3.5.11) show the $\theta - 2\theta$ scans and the corresponding simulated curves recorded in the vicinity of the (400) reflection for virgin and YSZ crystals irradiated at 573, 773 and 1073 K respectively. For all the cases, simulations are close to perfect. For the highest fluences, the agreement is less satisfactory, which mainly stems from the fact that the intensity emanating from the irradiated region is extremely weak and featureless, which significantly complicates the fitting. The strain and DW profiles obtained from the sim-

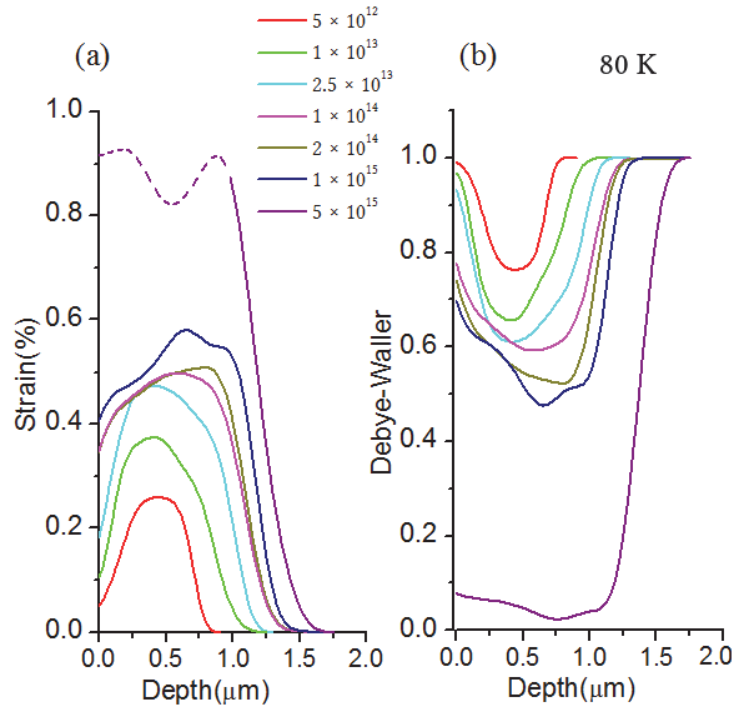


Figure 3.5.6: Strain (a) and Debye-Waller profiles (b) obtained after the simulation of the XRD curves displayed in (3.5.5) for 80 K.

ulations are shown in the figures (3.5.8), (3.5.10) and (3.5.12). Let us first discuss the strain profiles. Upon increasing fluence, for all temperatures, it can be observed that the maximum strain level in the irradiated region increases, in perfect agreement with the qualitative observation of the XRD data. In addition, it can also be observed that the width of the damaged region increases and globally the depth of the maximum strain is shifted towards higher values. For the two highest temperatures (i) between the depth range of 0.12 to 0.39 μm for the fluence 10^{15} and between 0.12 to 1.17 μm for the fluence 5×10^{15} for 773 K and (ii) between the depth range of 0.2 to 0.7 μm for the fluence 5×10^{14} and between 0.14 to 1.1 μm for the fluence 10^{15} for 1073 K, the strain profiles exhibit an unrealistic oscillating shape (shown as dotted lines), as already explained for the case of 80 K and 300 K irradiations. Upon increasing fluence, as expected from the qualitative observation of the curves, we clearly observe an increase in the level of disorder (decrease of DW). Similarly to what is observed for the strain, the width of the damaged region increases with increasing fluence, and simulated damaged thickness, are similar for all temperatures. For the highest fluence, the DW is close to 0 (say < 0.05) over a wide range of depth ($\sim 1 \mu\text{m}$). This finding indicates that the YSZ crystal in these regions is severely defective.



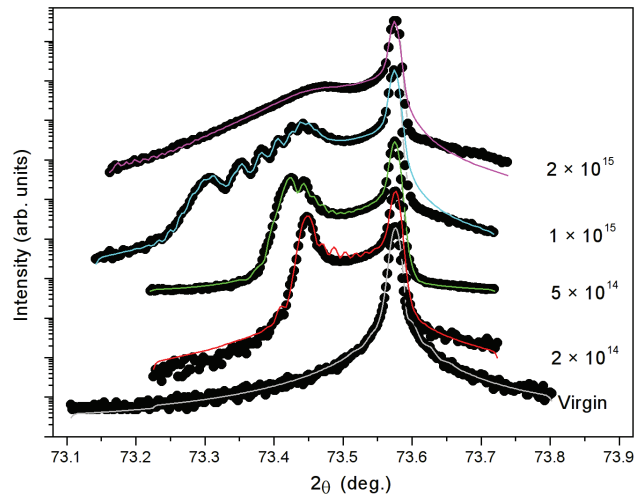


Figure 3.5.7: $\theta - 2\theta$ scans (black circles) and corresponding simulated curves (coloured lines) recorded in the vicinity of the (400) reflection for virgin and YSZ crystals irradiated at 573 K for increasing Au-ion fluences. The curves are shifted vertically for clarity.

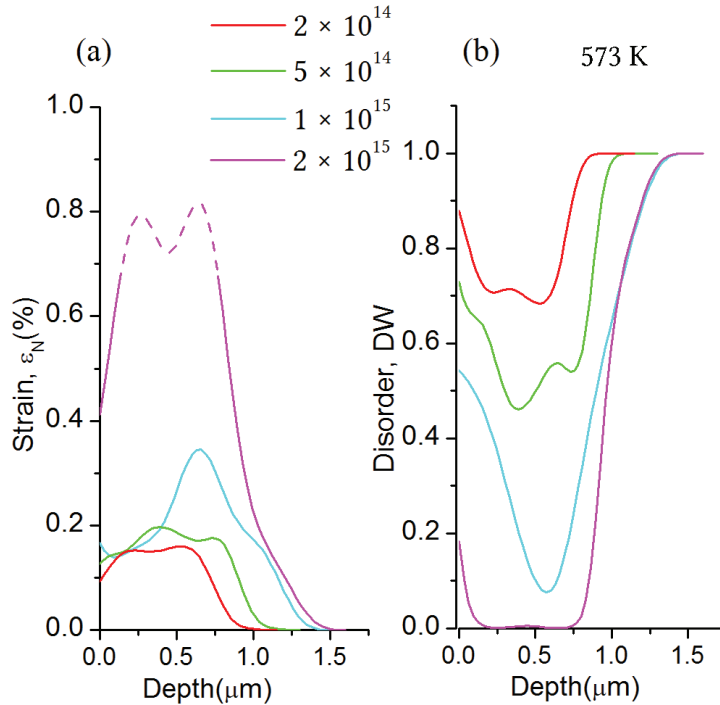


Figure 3.5.8: Strain (a) and Debye-Waller profiles (b) obtained after the simulation of the XRD curves displayed in (3.5.7) for 573 K.



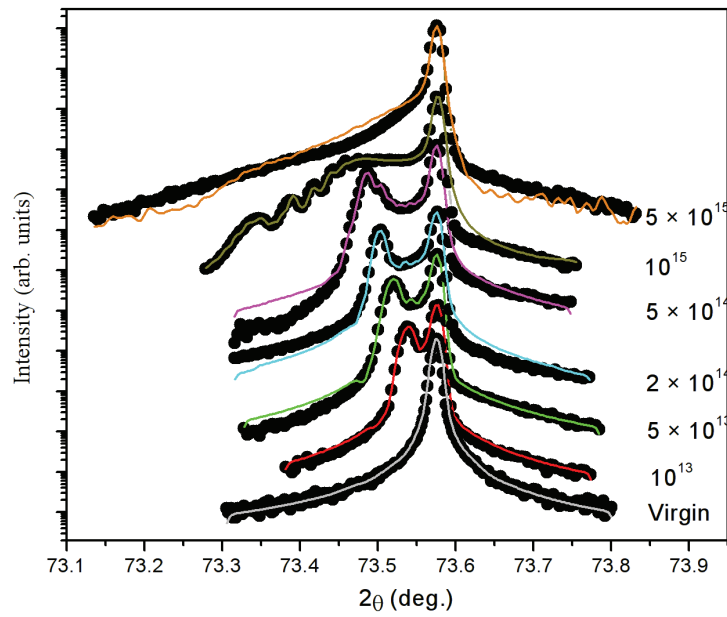


Figure 3.5.9: $\theta - 2\theta$ scans (black circles) and corresponding simulated curves (coloured lines) recorded in the vicinity of the (400) reflection for virgin and YSZ crystals irradiated at 773 K for increasing Au-ion fluences. The curves are shifted vertically for clarity.

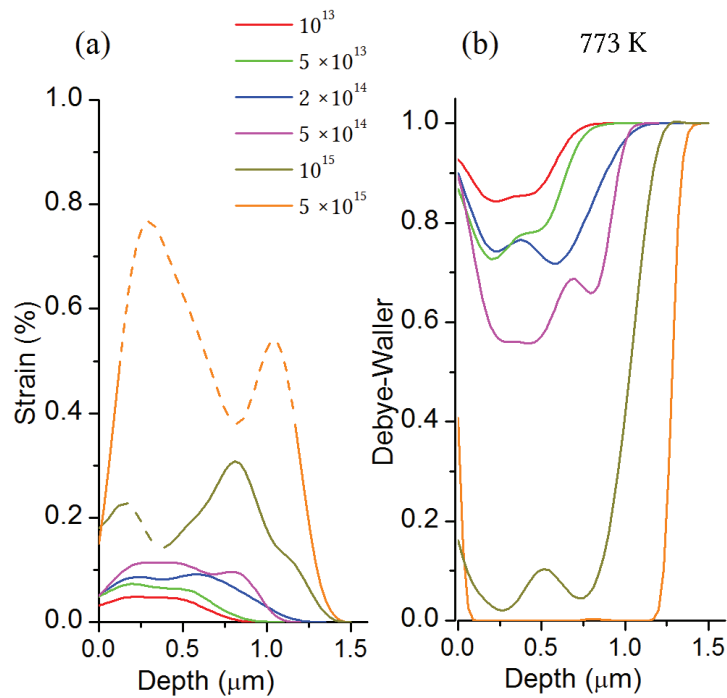


Figure 3.5.10: Strain (a) and Debye-Waller profiles (b) obtained after the simulation of the XRD curves displayed in (3.5.9) for 773 K



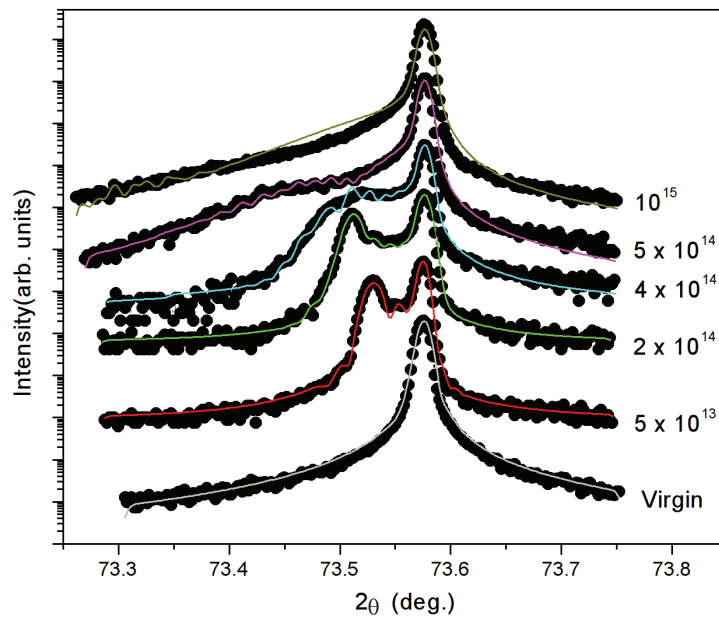


Figure 3.5.11: $\theta - 2\theta$ scans (black circles) and corresponding simulated curves (coloured lines) recorded in the vicinity of the (400) reflection for virgin and YSZ crystals irradiated at 1073 K for increasing Au-ion fluences. The curves are shifted vertically for clarity.

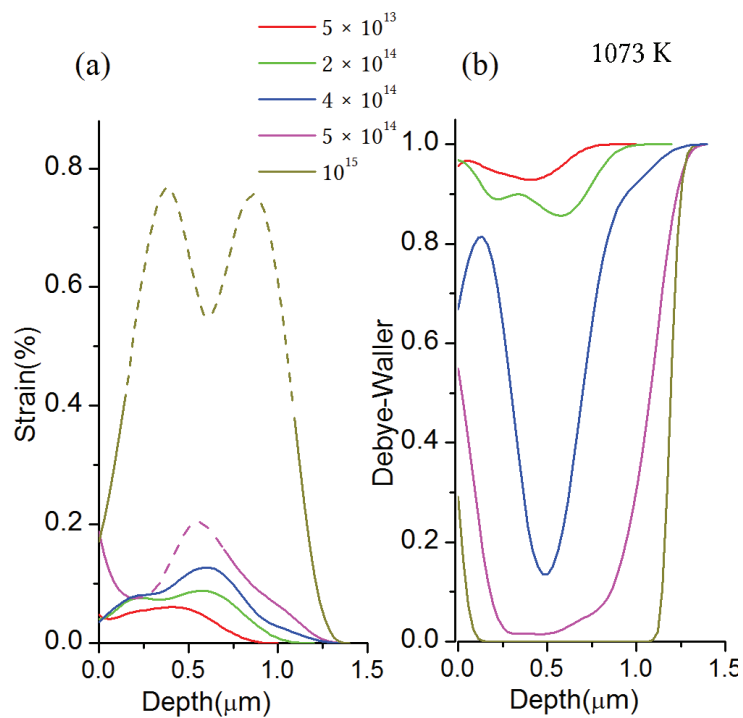


Figure 3.5.12: Strain (a) and the Debye-Waller profiles (b) obtained after the simulation of the XRD curves displayed in (3.5.11) for 1073 K



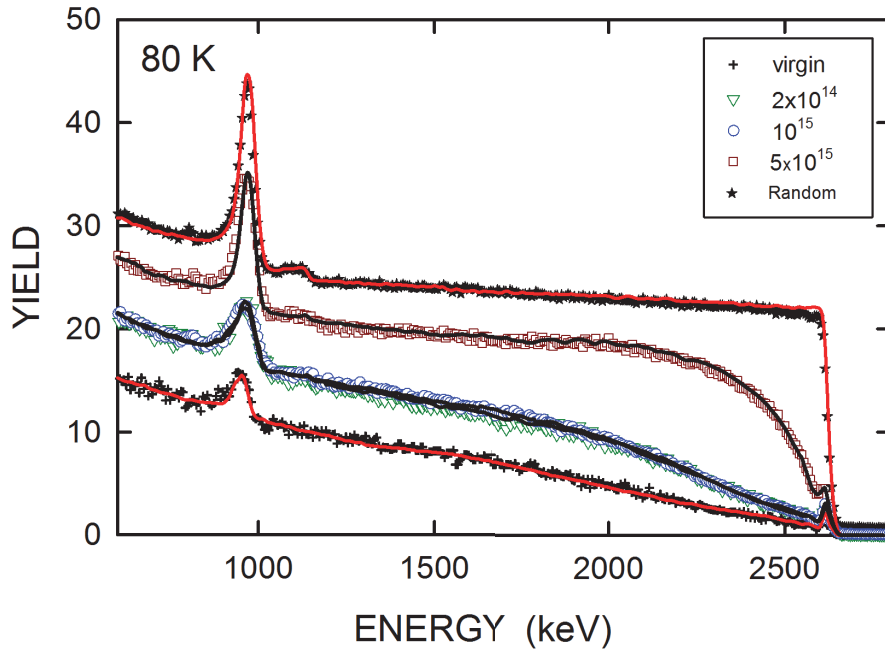


Figure 3.5.13: RBS spectra recorded in random (stars) and $\langle 100 \rangle$ -aligned (open symbols) directions on YSZ crystals irradiated with 4-MeV Au ions at the 80 K temperature and indicated fluences (in cm^{-2}). Energy of the analyzing He beam is 3.07 MeV. Solid lines are fits to experimental data with the McChasy code.

3.5.2 RBS/C

Cubic zirconia was further analyzed with the help of Rutherford backscattering spectroscopy in the channelling mode (RBS/C). Figure (3.5.13) displays RBS/C spectra recorded on a YSZ single crystal irradiated at the temperature of 80 K in aligned and random directions. Results from this temperature are representative of the whole results obtained for all temperatures. They will be discussed in detail in the following. These spectra present the number of backscattered particles as a function of their energy as detected with the incident beam oriented along the crystallographic direction $\langle 100 \rangle$ (*i.e.*, by rotating the crystal about the crystallographic axis $\langle 100 \rangle$) or in a random direction. In the different experimental conditions used for these experiments, energy resolution is on the order of 15 keV, which corresponds to a depth resolution in YSZ on the order of 10 nm. The spectra obtained in the random orientation on virgin crystals exhibit a much higher yield than the channelling orientation and spectra registered in the axial orientation exhibit low backscattering yields due to the channelling effect.

The spectra registered in random orientation exhibits a plateau below 2600 keV which corresponds to the backscattering of analysing particles from the Zr atoms of the sample, and a peak close to 1000 keV due to the backscattering of analysing particles from the O atoms. The appearance of this peak is the consequence of the elastic resonant reaction at 3.038 MeV of ${}^4\text{He}({}^{16}\text{O}, {}^{16}\text{O}){}^4\text{He}$ which enhances the backscattering on O sublattice target. The spectrum registered in the $\langle 100 \rangle$ -axial direction on a virgin crystal shows the same features with a much lower backscattering yield for both the Zr and O signals

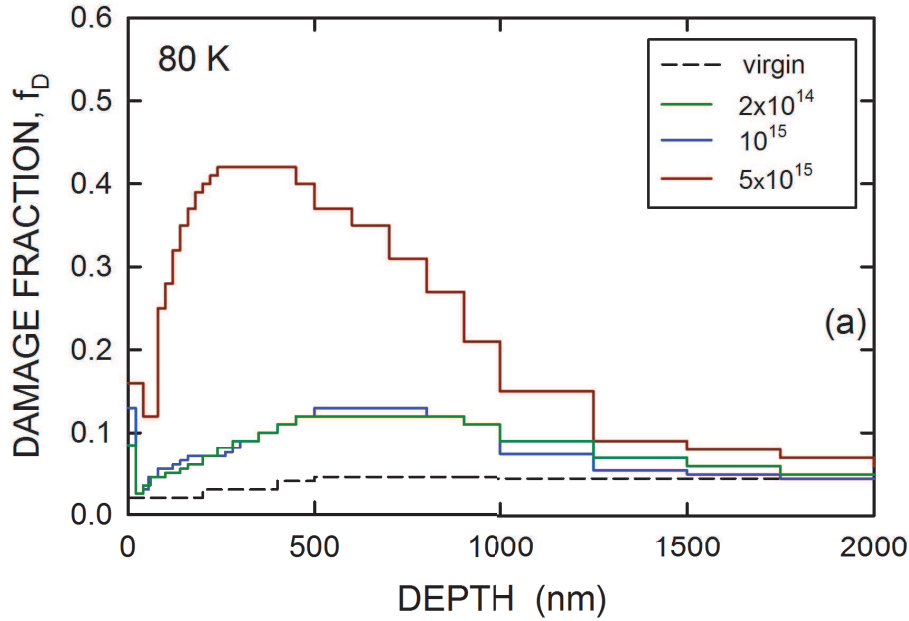


Figure 3.5.14: Damage fraction (f_D) as a function of depth extracted from the fits to experimental RBS/C data for YSZ crystals irradiated at 80 K temperature under the indicated fluences (in cm^{-2})

due to the channelling effect.

The spectrum registered in the $\langle 100 \rangle$ -axial direction on irradiated crystals exhibit an increase with increasing ion fluence of both the Zr and O yields due to the creation of radiation damage. A dechannelling bump is clearly observed around 2100 keV, indicating that the defects are predominantly located at the depth corresponding to this energy. This bump is gradually spread toward the high and low energies as the fluence increases. It should be borne in mind that the energy scale corresponds to a scale in reverse depth in the material. Thus, the energy of the backscattered ions corresponds to events occurring in the sample surface and the lowest energy represents the deeper regions of the sample.

RBS/C spectra in figure (3.5.13) were fitted (solid lines) by using McChasy computer code [39] [40] [41], which is based on Monte Carlo statistical approach [42] (section 2.1.2). Calculations rely on the basic assumption that Zr and O atoms are randomly displaced from original lattice sites during irradiation. Figure (3.5.14) shows the variation of the fraction of displaced atoms (f_D) as a function of the depth into the sample extracted from McChasy simulations. These data correspond to the Zr sublattice, since the amount of damage created in the O sublattice may only be measured at the depth where the resonance occurs [43] [44]. For various fluences, f_D exhibits a peak around 500 nm, with an increase in width and amplitude for increasing ion fluence up to $5 \times 10^{15} cm^{-2}$.

RBS/C experiments for YSZ sample were performed for other temperatures too *i.e.*, 300, 573, 773



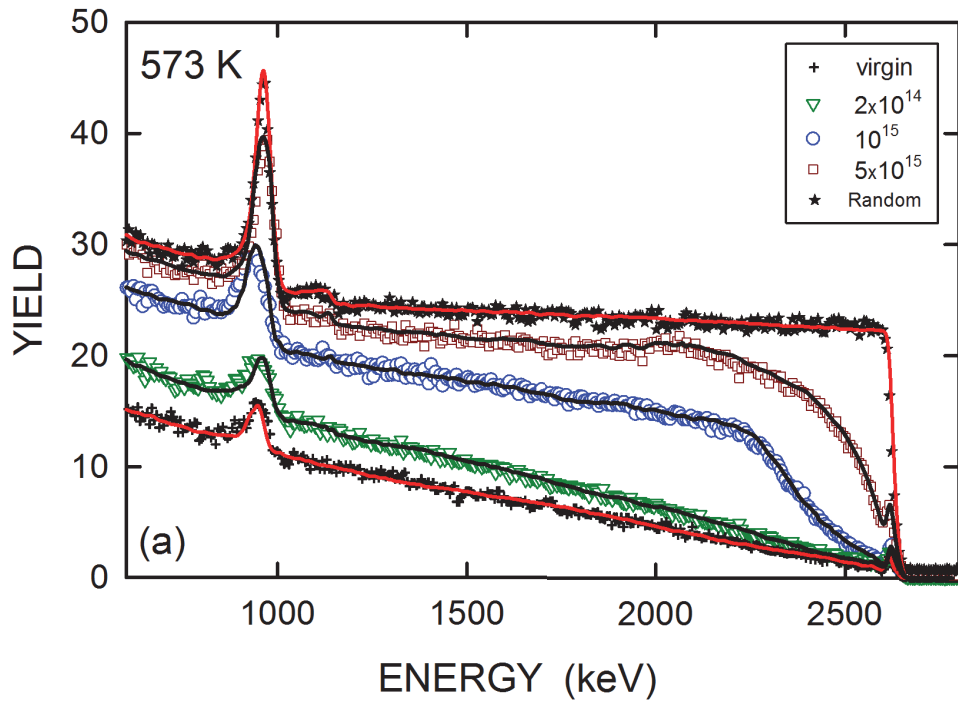


Figure 3.5.15: RBS spectra recorded in random (stars) and $\langle 100 \rangle$ -aligned (open symbols) directions on YSZ crystals irradiated with 4-MeV Au ions at the 573 K temperature and indicated fluences (in cm^{-2}). Energy of the analyzing He beam is 3.07 MeV. Solid lines are fits to experimental data with the McChasy code.

and 1073 K. The results from the other temperatures show a similar behaviour. The results from 573 K and 1073 K are displayed in the figures (3.5.15) and (3.5.17) as illustrations of the whole sets of data. RBS/C analysis of YSZ under room temperature and 773 K has been previously carried out by Moll *et. al.* [36] [37] [45]. Main conclusions drawn from all these results can be summed up as follows. Firstly, irrespective of the irradiation temperature, the damage profiles have a similar shape, with a thickness comprised between 1 and 1.2 μm and a peak located around 500 nm (consistent with XRD results). Secondly, f_D is very small (~ 0.1) at low ion fluence ($2 \times 10^{14} \text{cm}^{-2}$) and does not exceed 0.5 at high fluence ($3 - 5 \times 10^{15} \text{cm}^{-2}$). A comparable evolution of the spectra with increasing fluence is observed for the different temperatures, *i.e.*, the backscattering yield increases with fluence (up to $3 - 5 \times 10^{15} \text{cm}^{-2}$) without reaching the random level. However, this apparent similarity exhibits a major difference that is readily noticed when comparing the spectra corresponding to crystals irradiated at the same fluence : rising the temperature leads to a significant increase of the backscattering yield. For instance, at 10^{15}cm^{-2} , f_D equals 0.1 at 80 K, 0.3 at 573 K and 0.4 at 1073 K, which is a clear indication that the disordering build-up is accelerated with increasing temperature.

If we compare the results of the disordering build-up f_D with the damage profiles obtained by XRD, we notice a similar trend. For instance, the minimum DW for the fluence 10^{15}cm^{-2} is 0.5 for 80 K, 0.1 for 573 K and 0.05 for 1073 K.



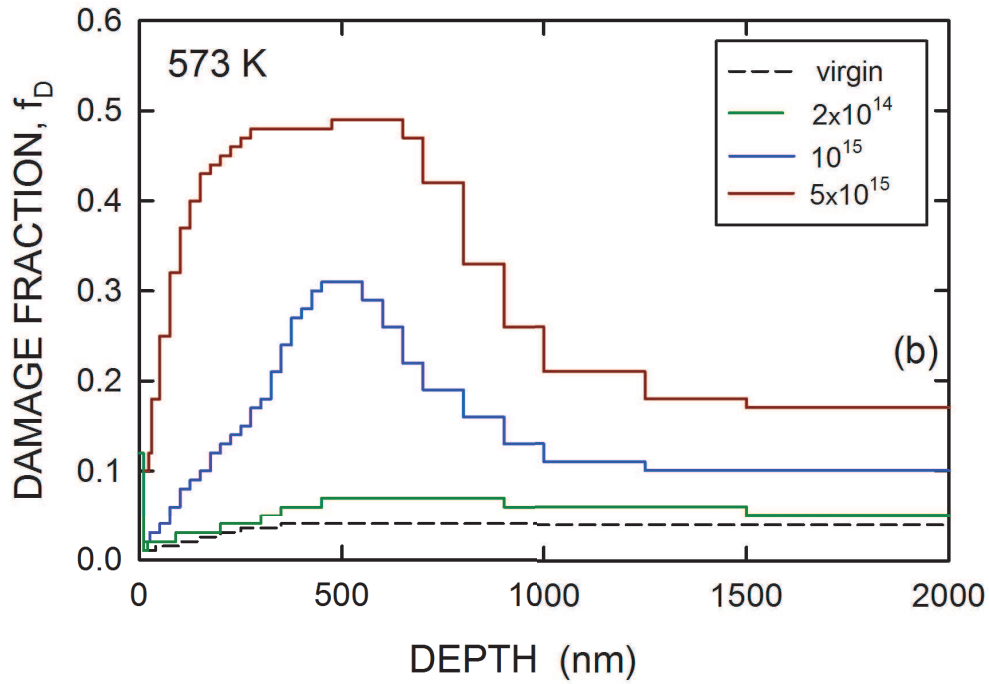


Figure 3.5.16: Damage fraction (f_D) as a function of depth extracted from the fits to experimental RBS/C data for YSZ crystals irradiated at 573 K temperature under the indicated fluences (in cm^{-2})

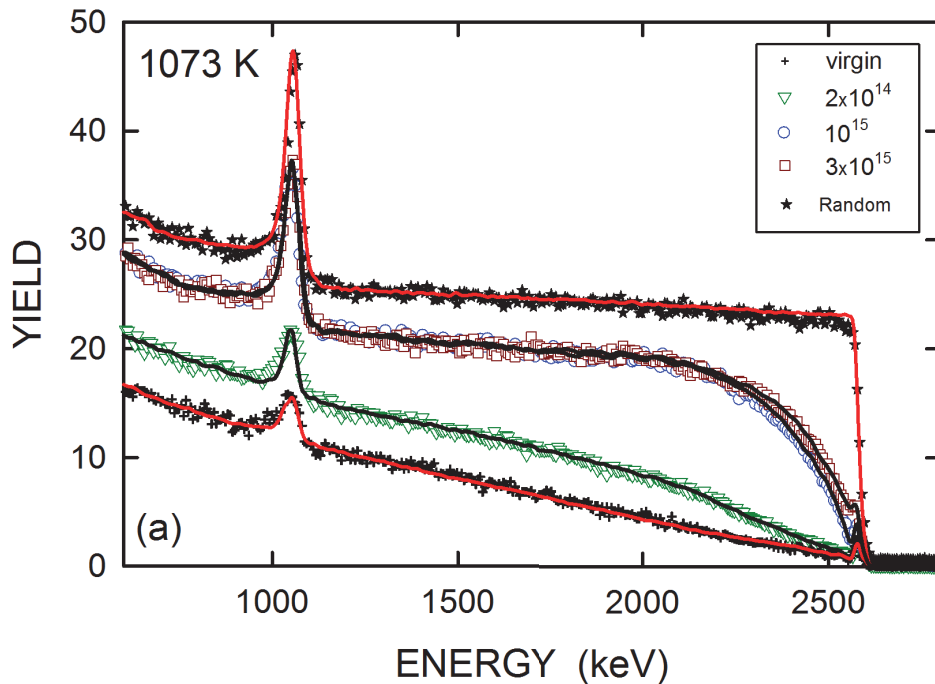


Figure 3.5.17: RBS spectra recorded in random (stars) and $\langle 100 \rangle$ -aligned (open symbols) directions on YSZ crystals irradiated with 4-MeV Au ions at the 1073 K temperature and indicated fluences (in cm^{-2}). Energy of the analyzing He beam is 3.07 MeV. Solid lines are fits to experimental data with the McChasy code.



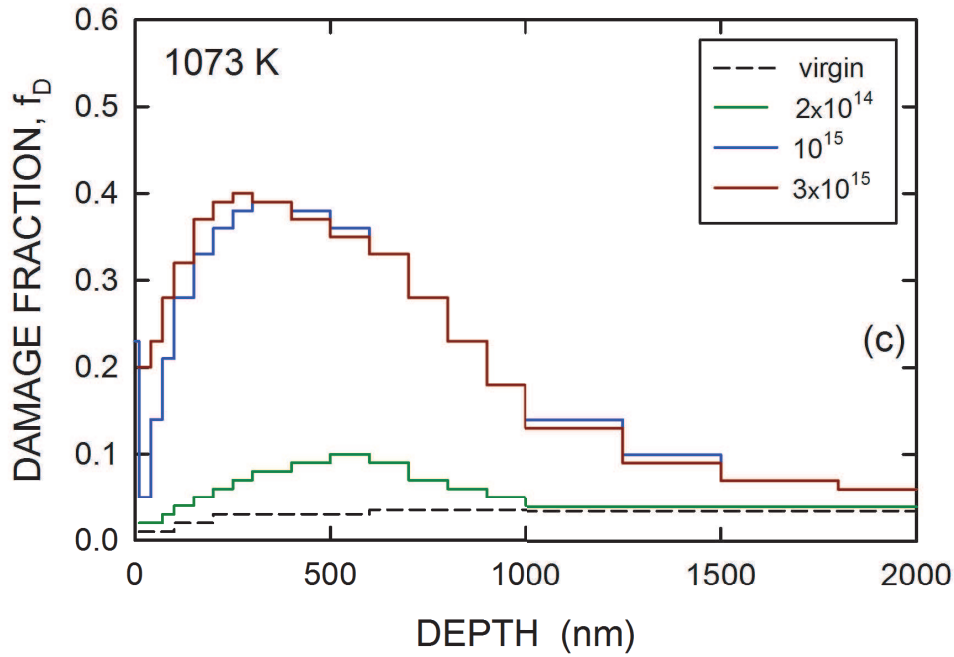


Figure 3.5.18: Damage fraction (f_D) as a function of depth extracted from the fits to experimental RBS/C data for YSZ crystals irradiated at 1073 K temperature under the indicated fluences (in cm^{-2})

3.6 DISCUSSION

3.6.1 RBS/C KINETICS

The evolution of the damage level at the damage peak obtained by RBS/C is presented in Figure (3.6.1). The experimental data are fitted using the multi-step damage accumulation model (MSDA). The fits of RBS/C data with this model are represented by solid lines in figure (3.6.1). The evolution of the damage fraction with the ion fluence is reproduced using the MSDA model with three steps [$n = 3$ in equation (1.2)]. For all the temperatures, the first step represents the slow increase of the damage fraction f_D up to a certain fluence. The first interesting behaviour is observed at the threshold fluence, where the transition occurs from damage step 1 to step 2. The transition occurs at lower fluences for higher temperatures. For the case of 80 K and 300 K, the transition occurs at the ion fluence of $\sim 1.2 \times 10^{15} cm^{-2}$ whereas for the 1073 K, the transition is at $\sim 0.5 \times 10^{14} cm^{-2}$. The values of fluences for the onset of step 2 are listed in table (3.6.1).

Secondly, the maximum damage at the end of second step is found to be lowered with increasing temperature. This behaviour is true for all temperatures except for 80 K where the maximum damage is found to be about the same as 300 K within the error limits. Overall, no temperature-enhanced dynamic annealing [46] is observed in YSZ and a same multi-step disordering process occurs in this material irrespective of the irradiation temperature. The damage fraction f_D remains low irrespective of the fluences



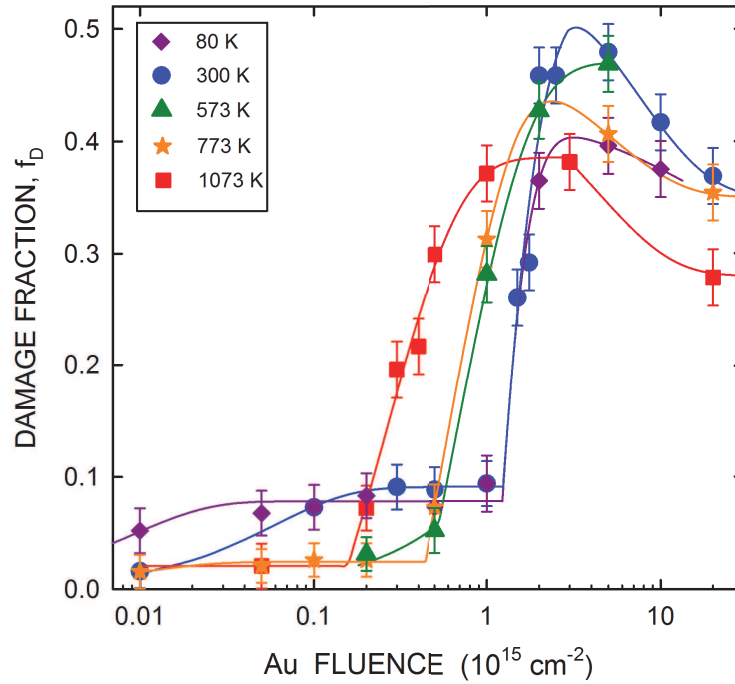


Figure 3.6.1: Disorder kinetics plotted from the data obtained by performing RBS/C for YSZ crystals irradiated with 4 MeV Au^{2+} ions at different temperatures indicated in the figure. Solid lines represent the data fits using the MSDA model

for all temperatures. This is not the case in other materials, for instance, SiC [47] or $SrTiO_3$ [48]. In the case of $SrTiO_3$, dynamic annealing is observed for irradiation at 773 K [48] and for Ag irradiated $4H-SiC$, it is around 600 K [47]. These materials readily undergo amorphization or sometimes exhibit a very low damage level under irradiation above a threshold temperature [49].

	80 K	300 K	573 K	773 K	1073 K
RBS/C	1.2×10^{15}	1.2×10^{15}	0.55×10^{15}	0.45×10^{15}	0.15×10^{15}
XRD	10^{15}	10^{15}	0.5×10^{15}	0.5×10^{15}	0.2×10^{15}

Table 3.6.1: Threshold fluences (in cm^{-2}) for the onset of the second step of the damage build-up in ion irradiated YSZ crystals. Values obtained from RBS/C measurements are derived from the fitting of experimental data with the MSDA model [40][41] and values from the XRD technique were graphically determined.



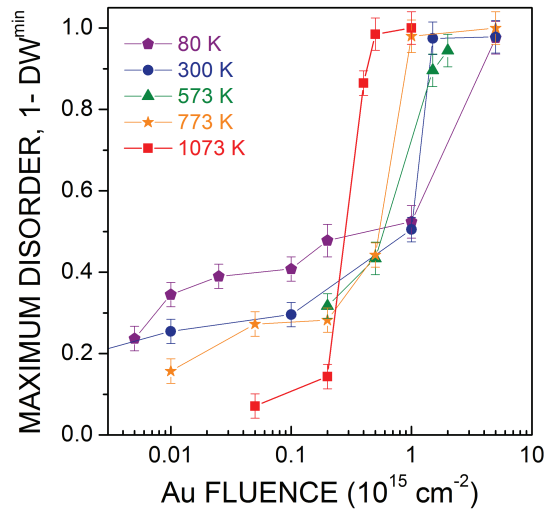


Figure 3.6.2: Variation of maximum damage as a function of ion fluence as determined by XRD

3.6.2 DEBYE-WALLER KINETICS

Figure (3.6.2) displays the evolution of the maximum disorder ($1 - DW^{\min}$) as a function of the ion fluence determined by XRD for all temperatures. This figure is obtained by selecting the minimum DW values extracted from the damage profiles [as in fig.(3.5.4)]. The minimum DW is plotted as $1 - DW^{\min}$ versus fluence instead of just DW^{\min} in order to compare it with the damage fraction determined by RBS/C. The kinetics exhibit a two-step behaviour irrespective of the temperature, as explained in section (3.5.1). Indeed, there is a slow increase in damage up to a critical fluence, followed by a dramatic increase beyond this fluence, similar to what has been observed using RBS/C (figure 3.6.1). However, the absolute values of the damage are markedly different: a full damage ($DW = 0$) is obtained by XRD, whereas the damage fraction obtained by RBS/C is always lower than 1. It indicates that the crystals appear to be severely defective in the XRD technique compared to the RBS/C. This difference can be ascribed to differences in the sensitivity of both techniques. XRD results from the constructive interferences between the waves scattered by all atoms and is hence very sensitive to minute atomic displacements. On the other hand, it is expected that much larger displacements are required to induce backscattering/dechanneling in RBS. It should also be borne in mind that XRD in the symmetric $\theta - 2\theta$ configuration probes out-of-plane displacements, whereas RBS/C performed normal to the surface probes in-plane lattice displacements. Therefore, anisotropic strain fields, such as that observed in irradiated single crystals, might induce different responses depending on the direction analysed.

In addition, two other interesting features should be noted. First, below the threshold fluence, increasing the temperature results in a partial but noticeable healing of the material (*i.e.* the damage is less pronounced) which can be ascribed to an enhanced annihilation rate of defects as a result of an enhanced mobility. Secondly, the transition fluence is shifted towards lower values at higher temperatures



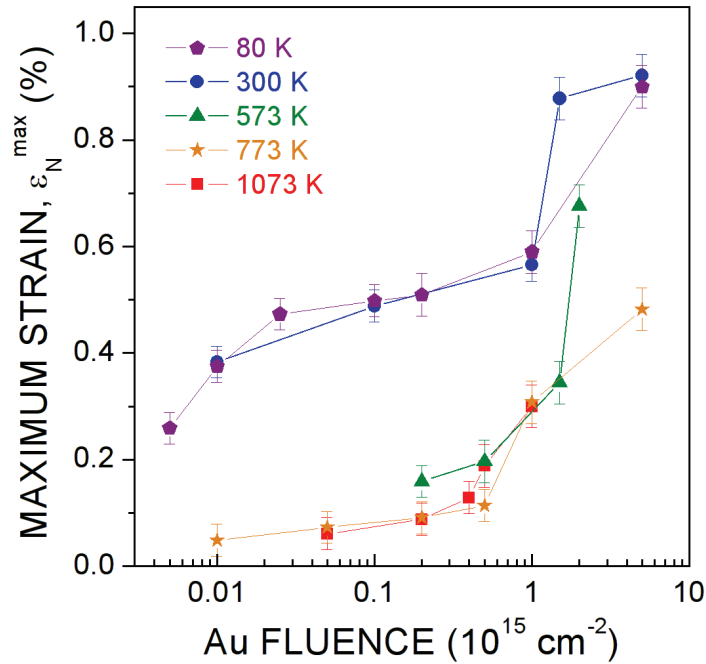


Figure 3.6.3: Variation of maximum strain as a function of ion fluence for different temperatures.

(from 10^{15} to $2 - 4 \times 10^{14} \text{ cm}^{-2}$), similar to the behaviour observed by RBS/C.

3.6.3 STRAIN KINETICS

Figure (3.6.3) displays the evolution of the maximum strain as a function of the ion fluence and of the irradiated temperature. These figures are obtained by selecting the maximum physical strain from the XRD curves presented in the previous section. It can be noted here that the maximum strain location progresses with fluence from damage peak to the interface.

The strain build-ups presented in figure (3.6.3) can be separated into two groups: 80 K and 300 K on one hand and 573 K, 773 K and 1073 K on the other hand. For the former group (at low temperature), strain levels are high with values $\sim 0.4\%$ in the first step and $\sim 0.9\%$ in the second step. For the latter group (high temperature), strain levels are much lower with values ranging from $\sim 0.1\%$ to $\sim 0.5\%$. This difference in the strain level as a function of the irradiation temperature appears very similar to that recently reported by Yang *et. al.* [50] who monitored the strain in YSZ irradiated with ions of different velocities. They found that the strain level in the first step decreased with increasing velocity, an effect which was tentatively attributed to an ionization-induced enhanced defect-mobility due to a larger electronic energy loss. This interpretation could hold for the present results, with thermal energy playing the role of electronic energy. At low temperature, transition from the first step to the second one takes



place at $\sim 10^{15} \text{cm}^{-2}$ while at high temperature it occurs at $\sim 5 \times 10^{14} \text{cm}^{-2}$. There is no progressive shift as observed for the damage (RBS/C) and disorder (XRD) kinetics probably because the strain is not monitored at the same depth as a function of the ion fluence. These results indicate that the strain relaxation is not the main driving force for the formation of the dislocation loops, *i.e.*, for the occurrence of the second step of the damage build-up.

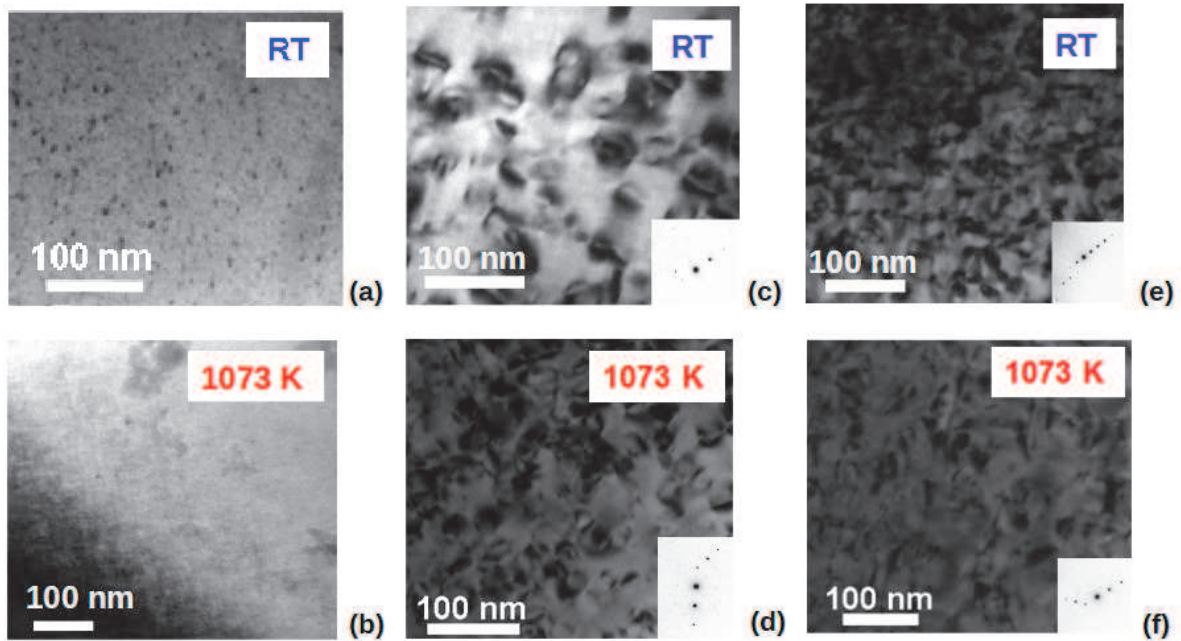


Figure 3.6.4: TEM bright-field micrographs recorded on YSZ crystals with 4 MeV Au^{2+} ions at 300 K (top) and 1073 K (bottom) and at different places (fluences) of the damage build-up plotted in figure (3.6.1) (a) 10^{15}cm^{-2} and (b) $5 \times 10^{13} \text{cm}^{-2}$ correspond to the first step; (c) $1.5 \times 10^{15} \text{cm}^{-2}$ and (d) $4 \times 10^{14} \text{cm}^{-2}$ are characteristic of the beginning of the second step; (e) $2 \times 10^{15} \text{cm}^{-2}$ and (f) $7 \times 10^{14} \text{cm}^{-2}$ illustrate microstructure observed at the end of the second step.

3.6.4 DAMAGE EVOLUTION

Figure (3.6.4) displays TEM images recorded on crystals irradiated at room temperature and 1073 K at different steps of the damage build-up: Figure (3.6.4a) and (3.6.4b) reflect the first step, figures (3.6.4c) and (3.6.4d) correspond to the beginning of second step and figures (3.6.4e) and (3.6.4f) are characteristic of the end of the second step. Images for room temperature irradiation show the formation of small defect clusters in the first step of the irradiation process (3.6.4a), followed by the creation of dislocation loops (3.6.4c) and finally a network of tangled dislocations is observed (3.6.4e). Identical defects and microstructures are observed for irradiation at 1073 K, as clearly evidenced in figures (3.6.4b), (3.6.4d) and (3.6.4f) that correspond to the first step, the beginning and end of the second step, respectively. It



can thus be reasonably assumed that these results also hold for the intermediate temperatures.

The first transition of the damage accumulation process is shown to be associated with the transformation of black dots into black/black lobes that eventually form dislocation lines. Yasuda *et. al.*[51] studied this microstructure change mechanism and concluded, based on earlier works from Baufeld *et. al.*[52], that defects created in the first stage of the irradiation process are seeds for dislocation loops. More precisely, the following mechanism was proposed: (i) interstitial point defect agglomerate and (ii) form Frank loops with Burgers vectors $b = \frac{a}{3}\langle 111 \rangle$ (*i.e.*, dislocations bounding a stacking fault); (iii) these loops grow and transform into perfect (unfaulted) dislocation loops via the spontaneous nucleation of a Shockley partial dislocation according to the following equation $\frac{a}{6}\langle 11\bar{2} \rangle + \frac{a}{3}\langle 111 \rangle \rightarrow \frac{a}{2}\langle 110 \rangle$; (iv) finally, growth of these perfect loops leads to the formation of a network of dislocation lines. It is worth mentioning that the mechanism for the transformation of partial into perfect dislocation loops has also been reported in irradiated ceria (See ref [53] and the references therein). Both Baufeld *et. al.* [52] and Yasuda *et. al.*[51] postulated the existence of a critical defect size above which the actual defect is not stable anymore and turn into a new, stable one. This assumption has been supported by a theoretical model developed by Ryazanov *et. al.* [54] taking into account the charge state of the dislocation loops to explain their instability (hence their transformation into dislocation lines) above a critical size. The critical size was found to be on the order of a micrometer when the defect density is low and smaller when the loop density increases (*i.e.*, when the mean distance between loops decreases). Such a hypothesis of a critical size could perfectly explain the difference in the threshold fluence for the onset of step 2 observed in YSZ in the present work. Indeed, the shift of the transition fluence to lower values with increasing temperature would mean that the critical size is reached more rapidly. This is possible by assuming that increasing the temperature induces a higher defect mobility leading to an enhanced defect-clustering process. In addition, such an increased defect-clustering rate could also account for the decrease of the defect density explaining why (XRD) disorder and strain levels decrease with temperature. It is worth noting that this effect is already operational at 573 K, a temperature which seems rather low but is consistent with experimental observations of Baufeld *et. al.* of an accelerated defect growth above 573 K [52]. This result confirms the high mobility of the irradiation point defects in YSZ.

3.7 CONCLUSION

This chapter was chiefly aimed at retrieving strain and damage profiles from Yttria-stabilized zirconia crystals irradiated with 4 MeV Au^{2+} ions. The samples were irradiated for five different temperatures, namely, 80, 300, 573, 773 and 1073 K and for a wide range of fluences *i.e.*, from 5×10^{12} to $2 \times 10^{16} cm^{-2}$. Furthermore, the samples were characterized by various techniques like RBS/C, TEM and XRD in order to get an all-inclusive understanding of the behaviour of this ceramic under ion irradiation.

Firstly, combining the advanced XRD techniques with our own simulation model, we were able to extract the strain and damage profiles. The diffracted intensity was computed using the dynamical theory of diffraction formalism. The simulation procedure relies on generalized simulated annealing algorithm



for finding the global minimum of the fitting problem. Additionally, the strain and damage profiles were modelled using cubic B-spline functions. The outcome results indicate upon increasing fluence, the level of both strain and damage increases. Moreover, the width of the damaged region increases. For higher fluences, very high damage level results in abstruse behaviour of strain in the most defective regions. However, the strain can still be retrieved at the damage/pristine interfaces where it keeps on increasing for high values; this is a new result as compared to previous studies. We were able to obtain these important results thanks to XRD simulations.

Secondly, the radiation behaviour of ion-irradiated solids is generally investigated by determining the damage accumulation build-up, which is the variation of a given disorder parameter with the ion fluence. The damage build-ups obtained in irradiated YSZ revealed a similar multistep mechanism irrespective of the temperature wherein each step is characterized by specific disorder and strain levels corresponding to a well-defined microstructure. In the case of strain profiles too, we observe a two-step mechanism. In the heavily damaged regions ($DW < 0.05$), a strain relaxation involving plastic deformation takes place. Thus whilst the damage level increases, the elastic strain is partially relieved. With the present simulations, it is possible to retrieve the elastic strain in regions of crystals where plastic relaxation did not yet occur, generally at the damaged/pristine interfaces. Apart from the Bragg peak due to the unperturbed crystal, the curves obtained on irradiated crystals at high fluences display broad pseudo-peaks originating from heavily damaged regions ($1 - DW \sim 1$) whose position is not related to the actual level of strain in the irradiated region. The simulations show that the strain keeps on increasing at high fluence in the regions surrounding the damage peak. For this reason, the strain actually continues to increase in the second step of the damage build-up. This result holds for the whole temperature range. Increasing the temperature induces an enhanced defect clustering, that both lowers the strain and damage in the first step of the damage build-up and shifts the threshold fluence towards lower values. The damage fraction f_D values are very low (~ 0.1) at low fluence and is ~ 0.5 for high fluence. The comparison of the evolution of damage fraction f_D with the maximum disorder ($1 - DW^{max}$) shows a similar trend wherein the transition fluence between the steps are shifted towards lower values at higher temperatures. However, a full damage ($DW = 0$) is obtained by XRD whereas the damage fraction by RBS/C is always less than 1.

Dynamic (*i.e.*, inside collision cascades) annealing is very efficient in YSZ but this self-healing process is definitely not enhanced with increasing irradiation temperature; in fact, only a slight decrease in the final disorder level is observed over the broad temperature range. On the other hand, an increase of the irradiation temperature provides a larger mobility to radiation defects which presumably leads to an enhanced defect clustering. This mechanism triggers the observed microstructural transformations through the existence of a critical size above which the defect nature changes. Consequently, transitions in the damage accumulation process occur earlier in fluence with increasing temperature. It is worth mentioning that temperature as low as 573 K is sufficient to accelerate the disordering process in irradiated YSZ.

Finally, XRD techniques prove to be extremely useful in the study of irradiated materials. We were able



to obtain all these important information by applying advanced XRD techniques into the simulation model. These results will be extremely useful in nuclear industries when considering YSZ as an inert matrix fuel since temperatures higher than 573 K will be reached in fast neutron reactors.



REFERENCES

- [1] J. R. Fienup, "Phase retrieval algorithms: a comparison," *Applied optics*, vol. 21, no. 15, pp. 2758–2769, 1982.
- [2] J. Miao, T. Ishikawa, E. H. Anderson, and K. O. Hodgson, "Phase retrieval of diffraction patterns from noncrystalline samples using the oversampling method," *Physical Review B*, vol. 67, no. 17, p. 174104, 2003.
- [3] A. Y. Nikulin, "Uniqueness of the complex diffraction amplitude in X-ray bragg diffraction," *Physical Review B*, vol. 57, no. 18, p. 11178, 1998.
- [4] R. W. Gerchberg, "A practical algorithm for the determination of phase from image and diffraction plane pictures," *Optik*, vol. 35, p. 237, 1972.
- [5] Z. Zalevsky, R. G. Dorsch, and D. Mendlovic, "Gerchberg–saxton algorithm applied in the fractional fourier or the fresnel domain," *Optics letters*, vol. 21, no. 12, pp. 842–844, 1996.
- [6] I. Vartanyants and I. Robinson, "Partial coherence effects on the imaging of small crystals using coherent x-ray diffraction," *Journal of Physics: Condensed Matter*, vol. 13, no. 47, p. 10593, 2001.
- [7] W. Saxton, *Computer techniques for image processing in electron microscopy*, vol. 10. Academic Press, 2013.
- [8] I. Vartanyants, C. Ern, W. Donner, H. Dosch, and W. Caliebe, "Strain profiles in epitaxial films from X-ray bragg diffraction phases," *Applied Physics Letters*, vol. 77, no. 24, pp. 3929–3931, 2000.
- [9] G. Ross, M. Fiddy, and M. Nieto-Vesperinas, "The inverse scattering problem in structural determinations," in *Inverse scattering problems in optics*, pp. 15–71, Springer, 1980.
- [10] H. Quiney, A. Peele, Z. Cai, D. Paterson, and K. Nugent, "Diffractive imaging of highly focused X-ray fields," *Nature Physics*, vol. 2, no. 2, pp. 101–104, 2006.
- [11] P. Thibault, M. Dierolf, O. Bunk, A. Menzel, and F. Pfeiffer, "Probe retrieval in ptychographic coherent diffractive imaging," *Ultramicroscopy*, vol. 109, no. 4, pp. 338–343, 2009.
- [12] A. Segmüller, I. Noyan, and V. Speriosu, "X-ray diffraction studies of thin films and multilayer structures," *Progress in Crystal Growth and Characterization*, vol. 18, pp. 21–66, 1989.
- [13] S. Milita and M. Servidori, "X-ray rocking-curve analysis of crystals with buried amorphous layers. case of ion-implanted silicon," *Journal of applied crystallography*, vol. 28, no. 6, pp. 666–672, 1995.
- [14] S. Takagi, "A dynamical theory of diffraction for a distorted crystal," *Journal of the Physical Society of Japan*, vol. 26, no. 5, pp. 1239–1253, 1969.



- [15] D. Taupin, “Théorie dynamique de la diffraction des rayons x par les cristaux déformés,” *Bulletin De La Societe Francaise Mineralogie Et De Cristallographie*, vol. 87, no. 4, p. 469, 1964.
- [16] W. Bartels, J. Hornstra, and D. Lobeek, “X-ray diffraction of multilayers and superlattices,” *Acta Crystallographica Section A: Foundations of Crystallography*, vol. 42, no. 6, pp. 539–545, 1986.
- [17] M. Halliwell, M. Lyons, and M. Hill, “The interpretation of X-ray rocking curves from III–V semiconductor device structures,” *Journal of crystal growth*, vol. 68, no. 2, pp. 523–531, 1984.
- [18] A. Boulle, O. Masson, R. Guinebretière, and A. Dager, “A new method for the determination of strain profiles in epitaxial thin films using X-ray diffraction,” *Journal of applied crystallography*, vol. 36, no. 6, pp. 1424–1431, 2003.
- [19] A. Boulle, F. Conchon, and R. Guinebretière, “Strain profiles in thin films: influence of a coherently diffracting substrate and thickness fluctuations,” *Journal of Applied Crystallography*, vol. 42, no. 1, pp. 85–92, 2009.
- [20] A. Boulle and A. Debelle, “Strain-profile determination in ion-implanted single crystals using generalized simulated annealing,” *Journal of Applied Crystallography*, vol. 43, no. 5, pp. 1046–1052, 2010.
- [21] P. Lévy, *Calcul des probabilités*, vol. 9. Gauthier-Villars Paris, 1925.
- [22] W. Feller, *An introduction to probability theory and its applications*, vol. 2. John Wiley & Sons, 2008.
- [23] J. P. Nolan, “Parameterizations and modes of stable distributions,” *Statistics & Probability Letters*, vol. 38, no. 2, pp. 187–195, 1998.
- [24] C. De Boor, “A practical guide to splines. number 27 in applied mathematical sciences,” 1978.
- [25] I. Schoenberg, “Cardinal interpolation and spline functions,” *Journal of Approximation theory*, vol. 2, no. 2, pp. 167–206, 1969.
- [26] M. Unser, A. Aldroubi, and M. Eden, “B-spline signal processing. I. theory,” *Signal Processing, IEEE Transactions on*, vol. 41, no. 2, pp. 821–833, 1993.
- [27] S. Kirkpatrick, C. D. Gelatt, M. P. Vecchi, *et al.*, “Optimization by simulated annealing,” *science*, vol. 220, no. 4598, pp. 671–680, 1983.
- [28] N. Metropolis, A. W. Rosenbluth, M. N. Rosenbluth, A. H. Teller, and E. Teller, “Equation of state calculations by fast computing machines,” *The journal of chemical physics*, vol. 21, no. 6, pp. 1087–1092, 1953.
- [29] C. Tsallis and D. A. Stariolo, “Generalized simulated annealing,” *Physica A: Statistical Mechanics and its Applications*, vol. 233, no. 1, pp. 395–406, 1996.



- [30] D. Geman and G. S., “Stochastic relaxation, gibbs distributions, and the bayesian restoration of images,” *IEEE Trans. Pattern Anal. Mach. Int.*, vol. 6, pp. 721–741, 1984.
- [31] Y. Xiang, D. Sun, W. Fan, and X. Gong, “Generalized simulated annealing algorithm and its application to the thomson model,” *Physics Letters A*, vol. 233, no. 3, pp. 216–220, 1997.
- [32] C. Tsallis, “Possible generalization of boltzmann-gibbs statistics,” *Journal of statistical physics*, vol. 52, no. 1-2, pp. 479–487, 1988.
- [33] T. Schanze, “An exact D-dimensional tsallis random number generator for generalized simulated annealing,” *Computer physics communications*, vol. 175, no. 11, pp. 708–712, 2006.
- [34] H. Szu and R. Hartley, “Fast simulated annealing,” *Physics letters A*, vol. 122, no. 3, pp. 157–162, 1987.
- [35] T. J. Penna, “Traveling salesman problem and tsallis statistics,” *Physical Review E*, vol. 51, no. 1, p. R1, 1995.
- [36] S. Moll, L. Thomé, G. Sattonnay, A. Debelle, F. Garrido, L. Vincent, and J. Jagielski, “Multistep damage evolution process in cubic zirconia irradiated with MeV ions,” *Journal of Applied Physics*, vol. 106, no. 7, p. 073509, 2009.
- [37] S. Moll, A. Debelle, L. Thomé, G. Sattonnay, J. Jagielski, and F. Garrido, “Effect of temperature on the behavior of ion-irradiated cubic zirconia,” *Nuclear Instruments and Methods in Physics Research Section B: Beam Interactions with Materials and Atoms*, vol. 286, pp. 169–172, 2012.
- [38] A. Debelle, L. Thomé, A. Bouille, S. Moll, F. Garrido, L. Qasim, and P. Rosza, “Response of cubic zirconia irradiated with 4-mev au ions at high temperature: An x-ray diffraction study,” *Nuclear Instruments and Methods in Physics Research Section B: Beam Interactions with Materials and Atoms*, vol. 277, pp. 14–17, 2012.
- [39] J. Jagielski and L. Thomé, “Damage accumulation in ion-irradiated ceramics,” *Vacuum*, vol. 81, no. 10, pp. 1352–1356, 2007.
- [40] J. Jagielski and L. Thomé, “Multi-step damage accumulation in irradiated crystals,” *Applied Physics A*, vol. 97, no. 1, pp. 147–155, 2009.
- [41] J. Jagielski and L. Thomé, “Discontinuous character of the damage build-up in the elastic collision regime,” *Radiation Effects & Defects in Solids*, vol. 166, no. 5, pp. 367–372, 2011.
- [42] L. Nowicki, A. Turos, R. Ratajczak, A. Stonert, and F. Garrido, “Modern analysis of ion channeling data by monte carlo simulations,” *Nuclear Instruments and Methods in Physics Research Section B: Beam Interactions with Materials and Atoms*, vol. 240, no. 1, pp. 277–282, 2005.



- [43] J. Tesmer, M. Nastasi, J. Barbour, C. Maggiore, and J. Mayer, "Handbook of modern ion beam materials analysis (pittsburgh, pa: Materials research society)," 1995.
- [44] L. Thomé, A. Gentils, J. Jagielski, S. Enescu, and F. Garrido, "On the use of the ^{16}O (4He , 4He) ^{16}O resonance for the evaluation of radiation damage in oxides," *Nuclear Instruments and Methods in Physics Research Section B: Beam Interactions with Materials and Atoms*, vol. 219, pp. 99–104, 2004.
- [45] S. Moll, L. Thomé, F. Garrido, L. Vincent, G. Sattonnay, J. Costantini, J. Jagielski, A. Benyagoub, and M. Behar, "Radiation effects in yttria-stabilized zirconia: Comparison between nuclear and electronic processes," *Nuclear Instruments and Methods in Physics Research Section B: Beam Interactions with Materials and Atoms*, vol. 266, no. 12, pp. 3048–3051, 2008.
- [46] J. Williams, "Subsurface processing of electronic materials assisted by atomic displacements," *Mrs Bulletin*, vol. 17, no. 06, pp. 47–51, 1992.
- [47] E. Wendler, T. Bierschenk, W. Wesch, E. Friedland, and J. Malherbe, "Temperature dependence of damage formation in Ag ion irradiated 4H-SiC," *Nuclear Instruments and Methods in Physics Research Section B: Beam Interactions with Materials and Atoms*, vol. 268, no. 19, pp. 2996–3000, 2010.
- [48] Y. Li, R. Liu, W.-K. Chu, and T. Tate, "Observation of dynamic annealing effects in oxide single crystals after high-dose $^{18}\text{O}^+$ implantation at 500°C ," *Physical Review B*, vol. 57, no. 10, p. 5668, 1998.
- [49] J. Williams, K. Short, R. Elliman, M. Ridgway, and R. Goldberg, "Ion-beam-induced amorphization and dynamic annealing processes in silicon," *Nuclear Instruments and Methods in Physics Research Section B: Beam Interactions with Materials and Atoms*, vol. 48, no. 1, pp. 431–434, 1990.
- [50] T. Yang, C. A. Taylor, S. Kong, C. Wang, Y. Zhang, X. Huang, J. Xue, S. Yan, and Y. Wang, "The discrepancies in multistep damage evolution of yttria-stabilized zirconia irradiated with different ions," *Journal of Nuclear Materials*, vol. 443, no. 1, pp. 40–48, 2013.
- [51] K. Yasuda, C. Kinoshita, S. Matsumura, and A. Ryazanov, "Radiation-induced defect clusters in fully stabilized zirconia irradiated with ions and/or electrons," *Journal of Nuclear Materials*, vol. 319, pp. 74–80, 2003.
- [52] B. Baufeld, D. Baither, U. Messerschmidt, M. Bartsch, and I. Merkel, "In situ study on the generation of radiation damage in cubic-zirconia in the high-voltage electron microscope," *Journal of the American Ceramic Society*, vol. 76, no. 12, pp. 3163–3166, 1993.
- [53] Y. Miao, D. Aidhy, W.-Y. Chen, K. Mo, A. Oaks, D. Wolf, and J. F. Stubbins, "The evolution mechanism of the dislocation loops in irradiated lanthanum doped cerium oxide," *Journal of Nuclear Materials*, vol. 445, no. 1, pp. 209–217, 2014.



- [54] A. Ryazanov, K. Yasuda, C. Kinoshita, and A. Klaptsov, "Growth and instability of charged dislocation loops under irradiation in ceramic materials," *Journal of nuclear materials*, vol. 307, pp. 918–923, 2002.



4

Modelling of Diffuse X-ray scattering

4.1 INTRODUCTION

USING X-RAY DIFFRACTION, we were able to obtain some valuable information such as the strain and the damage profiles in irradiated YSZ crystals. However, further information such as the actual defects created inside the crystal, the behaviour of defects with the increase of fluence *etc*, cannot be retrieved using solely the coherent X-ray diffraction data. Hence, in this chapter, we go a step further to analyse the diffuse X-ray scattering (DXS) of the irradiated materials and model the reciprocal space maps (RSMs) corresponding to different defect configurations. This simulation can be broadly divided into two steps (i) the calculation of the displacement field from the defects and (ii) the calculation of the diffracted intensity.

For homogeneous and isotropic systems containing simple defects (*eg.*, spherical defects), there exists efficient analytical solutions [1] [2] [3] [4] [5] [6]. Real irradiated crystals, however, are complex systems containing inhomogeneous defect distribution with defects of different size, shape and type *etc*. Numerical calculations are often required in order to evaluate such systems. Previous attempts were successful only for relatively small crystals using atomistic simulations [7] [8] [9]. Here we develop an approach able to describe the DXS from large crystals (containing up to 10^9 unit cells). The computation of RSM from such large crystals, retaining the unit-cell resolution, requires huge amount of time for each calculation. Important efforts were devoted to optimize and accelerate the calculations.

The chapter is organized as follows: In the first part of this chapter, a simulation procedure is presented

which allows the fast calculation of the RSMs. We have made use of several tools such as vector programming and heterogeneous parallel computing which includes CPU multi-processing and GPU parallel computing. In the second part, simulations and the comparison of experimental data with our model are presented.

4.2 THEORETICAL BACKGROUND

Let us consider that we have a defect inside a crystal [10]. The amplitude scattered from an ensemble of unit cells with structure factor $F(Q)$ (equation 1.24) is given by:

$$E(\mathbf{Q}) = \sum_j F_j(Q) \exp[i\mathbf{Q} \cdot (\mathbf{r}_j + \mathbf{u}_j)] \quad (4.1)$$

where \mathbf{r}_j is the position of the j th unit cell in the ideal structure and \mathbf{u}_j is its displacement from the ideal structure. In the small displacements approximation, $\mathbf{Q} \cdot \mathbf{u} \simeq \mathbf{H} \cdot \mathbf{u}$ (where \mathbf{H} is the reciprocal lattice vector of the reflection considered). Hence the amplitude can be written in terms of the Fourier transform as

$$E(\mathbf{Q}) = F_0(Q) FT[V(\mathbf{r}_j)G(\mathbf{r}_j)] \quad (4.2)$$

where $V(\mathbf{r})$ crystal shape function, which is previously defined in Section (1.10). $G(\mathbf{r})$ is the correlation function,

$$G(\mathbf{r}) = \bar{\rho}(\mathbf{r}) \exp[i\mathbf{H} \cdot \mathbf{u}(\mathbf{r})] \quad (4.3)$$

where the relative scattering density is written

$$\bar{\rho} = 1 + \Delta F(\mathbf{r})/F_0 \quad (4.4)$$

This relative scattering density allows us to take into account the fact that the structure factor of a unit cell containing a defect, F_{defect} , may differ from the ideal structure factor, *i.e.* $F_{defect} = F_0 + \Delta F$. For instance, in the case of porous regions (*i.e.* vacancy clusters), $\bar{\rho} = 0$. If the displacement field $\mathbf{u}(\mathbf{r})$ is known, then the intensity can be straightforwardly computed from equations (4.2)-(4.4) and $|E(\mathbf{Q})|^2$. In an actual experiment, the intensity recorded on the detector results from the incoherent superposition of the intensities diffracted by different regions of the crystal. The usual notation where the z -axis is chosen perpendicular to the crystal surface and x -axis is contained in the crystal plane is used in the following. Besides, in laboratory experiments the beam is often only poorly collimated in the direction normal to the scattering plane (the plane defined by the incident and diffracted beam), resulting in axial divergences of the order of a few degrees, so that the diffracted intensity can be (infinitely) integrated over Q_y

$$\langle I(Q_x, Q_z) \rangle = \int dQ_y I(\mathbf{Q}) \quad (4.5)$$



where Q_y is the component of the scattering vector normal to the scattering plane [Fig. 4.3.1a]. Using the above equations, the intensity, $I(\mathbf{Q}) = E(\mathbf{Q}) \cdot E^*(\mathbf{Q})$, can be written as :

$$I(\mathbf{Q}) = |F_0|^2 \sum_{p,p'} \sum_{q,q'} \sum_{r,r'} G(x_p, y_q, z_r) G^*(x_{p'}, y_{q'}, z_{r'}) \exp[iQ_x(x_p - x_{p'})] \times \exp[iQ_y(y_q - y_{q'})] \exp[iQ_z(z_r - z_{r'})] \quad (4.6)$$

Equation (4.5) can hence be rewritten

$$\langle I(\mathbf{Q}) \rangle = |F_0|^2 \sum_{p,p'} \sum_{q,q'} \sum_{r,r'} G(x_p, y_q, z_r) G^*(x_{p'}, y_{q'}, z_{r'}) \exp[iQ_x(x_p - x_{p'})] \times \exp[iQ_z(z_r - z_{r'})] \int dQ_y \exp[iQ_y(y_q - y_{q'})] \quad (4.7)$$

The integral term in equation (4.7) is the delta function $\delta(y_q, y_{q'})$ and is hence equal to one for $y_q = y_{q'}$ (and equal to zero elsewhere, Fig. 4.3.1) The averaged intensity finally becomes

$$\langle I(Q_x, Q_z) \rangle = \sum_q |F_0|^2 \sum_{p,p'} \sum_{r,r'} G(x_p, y_q, z_r) G^*(x_{p'}, y_{q'}, z_{r'}) \exp[iQ_x(x_p - x_{p'})] \times \exp[iQ_z(z_r - z_{r'})] \quad (4.8)$$

The previous equation can be written in condensed form as

$$\langle I(Q_x, Q_z) \rangle = \sum_q |F_0|^2 |FT[V_q(x, z)G_q(x, z)]|^2 \quad (4.9)$$

where the two-dimensional correlation function $G_q(x, z)$ is

$$G_q(x, z) = \bar{\rho}(x, z) \exp[i\mathbf{H} \cdot \mathbf{u}_q(x, z)] \quad (4.10)$$

\mathbf{u}_q being the displacement field within q th plane of the crystal. Equation (4.9) shows that in the diffraction experiment the crystal can be viewed as divided into unit-cell-thick (x, z) planes, parallel to the scattering plane, that diffract incoherently with each other. The intensity diffracted from each (x, z) plane is given by the squared modulus of the amplitude scattered from each plane, and the intensities are summed to form the total scattered intensity.

4.3 SIMULATION PROCEDURE

The simulation procedure for the numerical evaluation of DXS can be broadly divided into two steps. Firstly, a defective crystal structure is generated using a Monte Carlo simulation procedure. To achieve this, vector programming and multiprocessing are utilized to manage large arrays. For the second step,



reciprocal space maps are computed by making use of GPUs in order to achieve the fastest computations possible. Even though the main goal is to achieve the numerical evaluation of DXS, optimization of the performance plays a major role. The whole program is presented in the Appendix 4.5. Below, the methodology and the optimization of each step is detailed.

4.3.1 THE DISPLACEMENT FIELD

In the framework of linear elasticity, the displacement at a given point \mathbf{r} in the crystal results from the superposition of the displacement fields of all defects in the crystal (equation 1.32) [11]

$$\mathbf{u}(\mathbf{r}) = \sum_{a,j} c_{a,j} \mathbf{u}_{a,j}(\mathbf{r} - \mathbf{r}_j) \quad (4.11)$$

where $c_{a,j}$ is the probability of having a defect of type a at the j th lattice site, and $\mathbf{u}_a(\mathbf{r})$ is the corresponding displacement field. From the previous chapter, it is clear that irradiation gives rise to point defects which in the first stages, migrates to form mostly spherical point-defect clusters. Hence here the focus is on spherical defects, although this approach is by no means restricted to spherical defects and can be used for any type of defect of any shape, as long as the corresponding displacement field can be computed.

In the framework of the elasticity theory of an isotropic medium, the displacement field associated to a spherical defect with radius R_a can be written as [12] [13] [14]:

$$\mathbf{u}_a(\Delta\mathbf{r}) = \begin{cases} A\Delta\mathbf{r}/R_a^3 & \text{if } |\Delta\mathbf{r}| \leq R_a \\ A\Delta\mathbf{r}/\Delta r^3 & \text{if } |\Delta\mathbf{r}| > R_a \end{cases} \quad (4.12)$$

where $A = \varepsilon R_a^3(1 + \nu)/[3(1 - \nu)]$ (ε is the lattice mismatch between the defect and the ideal crystal and ν is the Poisson's ratio of the crystal).

The evaluation of equation (4.11) is performed numerically using a Monte Carlo summation procedure. For this purpose, a three-dimensional *NumPy* array containing N unit-cells is generated, and defect coordinates \mathbf{r}_j are randomly chosen within this array. The displacement field corresponding to each defect \mathbf{u}_a is computed with equation (4.12) and added to the total displacement field \mathbf{u} . This procedure is repeated until the maximum number of defects $N\langle c_a \rangle$ is reached. In this approach, provision is made to tune the defect locations in order to match the actual defect structure of the samples investigated. This means that the defect distribution is not restricted to a random distribution. The main advantage by doing so is that spatially correlated defects, defect interactions (with a variable attraction or repelling zone), concentration gradients, *etc.*, can be straightforwardly implemented in this approach.

The obvious drawback of the approach is the time and memory needed to compute equation (4.11). For instance, a crystal with $N = 10^9$ unit-cells and displacement values coded over 64 bits (double-precision floating-point numbers) requires ≈ 8 GB memory. Since two copies of the displacement field has to be stored in the memory during the computation (corresponding to the total \mathbf{u} and the current \mathbf{u}_a displace-



ment field) the total memory needed to compute equation (4.11) reaches 16 GB. There are two options to compute this on a desktop computer *i.e.*, computation using CPU or GPU. Computation using GPU is interesting, since the speedup is much higher compared to the CPU. But, our current GPU has a memory of 3GB and even the best and most recent GPU available to date are limited to 12 GB memory which unfortunately prohibits their use for this calculation. Additionally, it is worth emphasizing that, given the large amount of data to transfer to the GPU as compared the very small computational cost of equation (4.11) (one array addition per computed \mathbf{u}_α), the acceleration would certainly not be very favorable. Moreover, the computation pathway cannot be determined in advance since the selection of random coordinates inside the three-dimensional *NumPy* array heavily relies on conditional instructions (*if, then, else*), for instance to produce non-random defect distributions, which is not ideal for the implementation on the GPU [15]. Equation (4.11) has hence been computed using the CPU.

In order to keep the memory footprint as low as possible and to maximize the computing speed the eval-

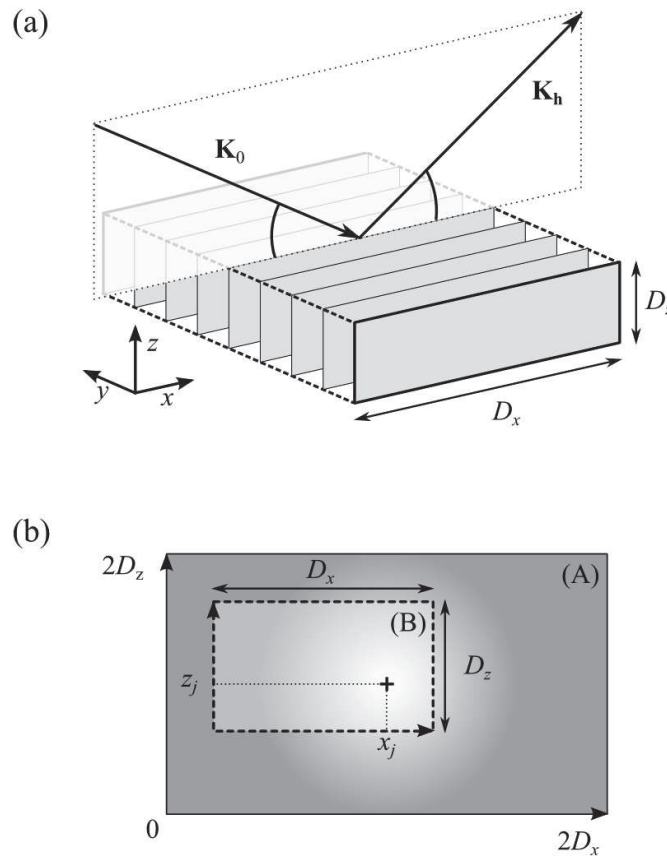


Figure 4.3.1: (a) Schematic view of the diffraction geometry. \mathbf{K}_0 and \mathbf{K}_h are the incident and diffracted wavevectors, respectively. D_x and D_z are the dimensions of the crystal along the x and z directions, respectively. (b) Schematic representation of the template-slicing approach. The template is indicated by rectangle (A) and the extracted view by rectangle (B).

uation of equation (4.12) has been implemented in C language and integrated in the *python* code using the *weave* module of the *SciPy* library. The `scipy.weave` package provides tools to include C/C++

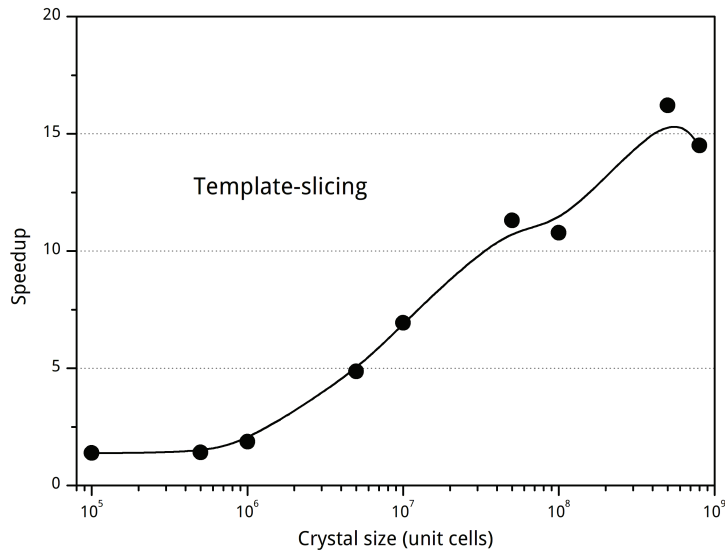


Figure 4.3.2: Speedup gain using the template-slicing approach versus the direct evaluation of equation (4.12) in the computation of the displacement field

code within the Python code. This offers another level of optimization in our program. Despite this, for $N = 10^9$ unit-cells, the computation still requires a few seconds, which is prohibitive, especially if several thousands of defects have to be generated. To circumvent this issue, we make use of a specific feature of the *NumPy* arrays known as “slicing” [16]: once an array is created it is possible to extract any sub-part (a “view”) of the array with no need to copy to the memory and at no computational cost (generating a view is performed in a few tens of microseconds). We hence generate a template displacement field for a crystal with twice the dimensions of the actual crystal in all directions, containing a defect in its center. A two-dimensional schematic is given in Fig. 4.3.1(b). From this template, any displacement field corresponding to the actual crystal, can be extracted using $\mathbf{u}_a(\Delta\mathbf{r}) = \mathbf{u}_{\text{template}}(\mathbf{D} - \mathbf{r}_j + \Delta\mathbf{r})$, where $\mathbf{D} = (D_x, D_y, D_z)^T$ is the size of the array. Equation (4.11) is then computed using the vectorized addition of the *NumPy* arrays. It should be noted, that this approach assumes that the displacement field around the defect is identical for all defects, independent of their location within the crystal. In particular this excludes the influence of free surfaces. In the case of sufficiently large crystals this effect is probably not dominant, but this approach could clearly not be used in the case of nanostructures.

The speedup obtained for the computation of the displacement field with this approach [as compared to the direct computation of equation (4.12)] is displayed in Fig. (4.3.2) for increasing crystal size, with a fixed defect density $\langle c_a \rangle = 10^{-5}$ defects/unit-cell. For arrays with less than 10^6 unit-cells there is no real gain in using the template-slicing approach; this finding likely stems from the fact that the time needed to create the template compensates the gain obtained by generating a view of it. For

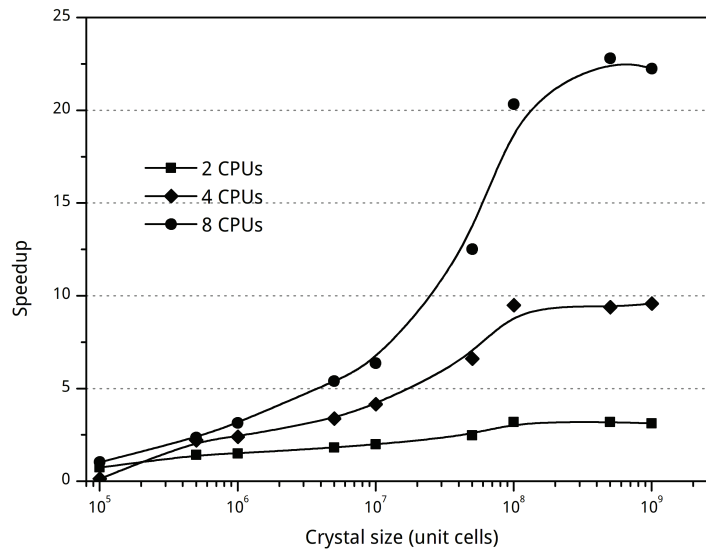


Figure 4.3.3: Speedup obtained with the use of an increased number of CPUs in parallel, in the computation of equation (4.11).

larger arrays, the speedup steadily increases, reaching a value of ~ 15 for $N = 10^9$ unit-cells.

As explained in detail in section (2.2.4), data transfers from the memory to the CPU requires considerable amount of time and it can be solved by computing using GPU, provided that the amount of GPU memory is sufficient [17]. In the present case, we propose to side-step this problem using multiprocessing, *i.e.* the calculation of the displacement field is distributed over the different cores of the processor. The parallelization can be performed in several ways; here we have chosen to parallelize over the dimensions of the crystal, so that each process computes the displacement field in a sub-region of the crystal. At the end of the calculation the different sub-regions are combined to form the entire displacement field. The main advantage of this approach, besides the obvious increased computing power, is that each process deals with a smaller array, hence resulting in increased transfer speed from memory to CPU. The corresponding speedup for increasing crystal size is displayed in Fig. (4.3.3).

For crystal sizes smaller than $N = 10^7$ unit-cells, the speed-up increases steadily and, as expected, the computing speed obtained with 8 processors is, respectively, 2 and 4 times faster than the speed obtained with 4 and 2 processors. Above 10^7 unit-cells, whereas the slope of the curve corresponding to 2 processors remains unchanged, the speedup obtained with 8 processors considerably increases (eventually saturating at a value of 22.5 for $N > 5 \times 10^8$ unit-cells, vs. 3.1 for 2 processors). This behaviour can probably be attributed to the fact that for those larger arrays, the speedup is limited by the time needed to transfer the data, an effect which is less pronounced when dealing with smaller arrays, hence the increased speedup when using multiple processors. It should be noted that, for this last benchmark, the time measurements (including the reference time with only one processor) include the template-slicing



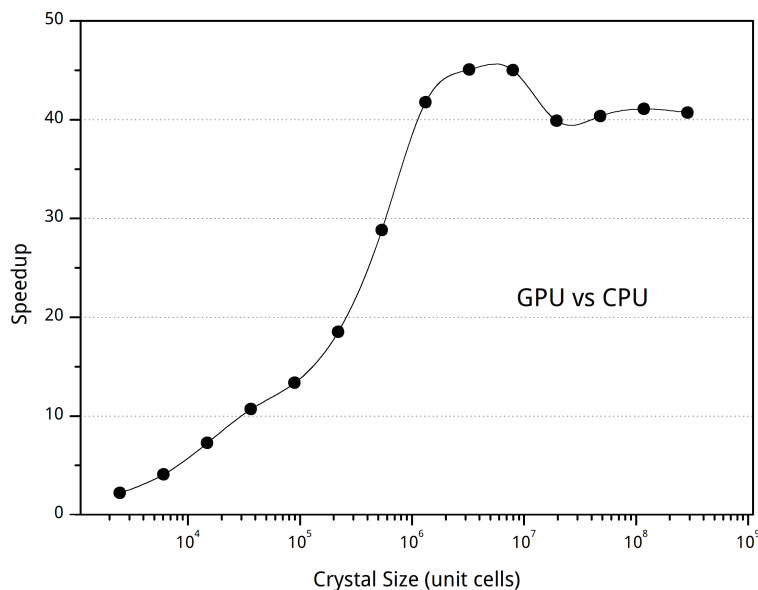


Figure 4.3.4: Speedup obtained with the GPU-based computing *versus* the conventional CPU approach.

modification detailed above. The total speedup therefore correspond to the product of both curves; in the best case we reach a total speedup of $22.5 \times 15 = 337.5$.

4.3.2 THE SCATTERED INTENSITY

We now focus on the evaluation of the scattered intensity. Equation (4.9) shows that it is actually the sum of (the squared modulus of) two-dimensional Fourier transforms, that can be evaluated independently. We here propose to compute the Fourier transform on the GPU using a fast Fourier transform (FFT) algorithm. The computational cost of FFT algorithms scales as $N \log(N)$ (N points in real space, N points in reciprocal space spanning a complete reciprocal unit-cell), versus N^2 for a direct evaluation of the sum, which make FFTs particularly relevant for the large crystal sizes considered in this work. Therefore, even if only a small fraction of the computed RSM is required, it is still considerably interesting to use an FFT algorithm. With an input array of size D'_i in a given direction, the FFT returns an array with spacing $1/D'_i$ in the associated direction. The size of the input array has therefore to be adjusted according to the desired reciprocal space resolution. A rule of thumb is that if the crystal size is D_i in a given direction, then the tiniest (finite size) interference feature will exhibit a period of $1/D_i$. Basic oversampling considerations requires an oversampling factor of two (the Nyquist rate). Here, in order to correctly describe an interference fringe without impairing the computation time, we chose an oversampling rate of 4, so that we obtain the condition $D'_i = 4 \times D_i$ (with $i = x, z$). In the y -direction the summation is incoherent so that we can take $D'_y = D_y$. In equation (4.9) the shape and size of the crystal are described by the term $V_q(x, z)$. In the present work we restricted the study to parallelepipedic



shapes such that $V_q(x, z) = V(x)V(z)$ and we wrote

$$V(i) = \frac{1}{2} \left[1 - \operatorname{erf} \left(\frac{i - D_i}{\sqrt{2}\sigma_i} \right) \right] \quad (4.13)$$

where $i = x, z$. Equation (4.13) allows, if needed, to account for fluctuations of the crystal size. For simplicity, the size distribution is assumed to be Gaussian, with standard deviation σ_i . When $\sigma_i \rightarrow 0$, equation (4.13) is a top-hat function ($= 1$ if $0 \leq x \leq D_i$, 0 otherwise) and its FFT is equal to a sinc function with well defined interference fringes with period $1/D_i$.

Equations (4.9) and (4.10) are directly evaluated on the GPU after the two-dimensional view $\mathbf{u}_q(x, z)$ has been extracted from the three-dimensional displacement field $\mathbf{u}(\mathbf{r})$ computed in the previous section, and this operation is repeated for all values of q , *i.e.* all (x, z) planes in the crystal. The speedup

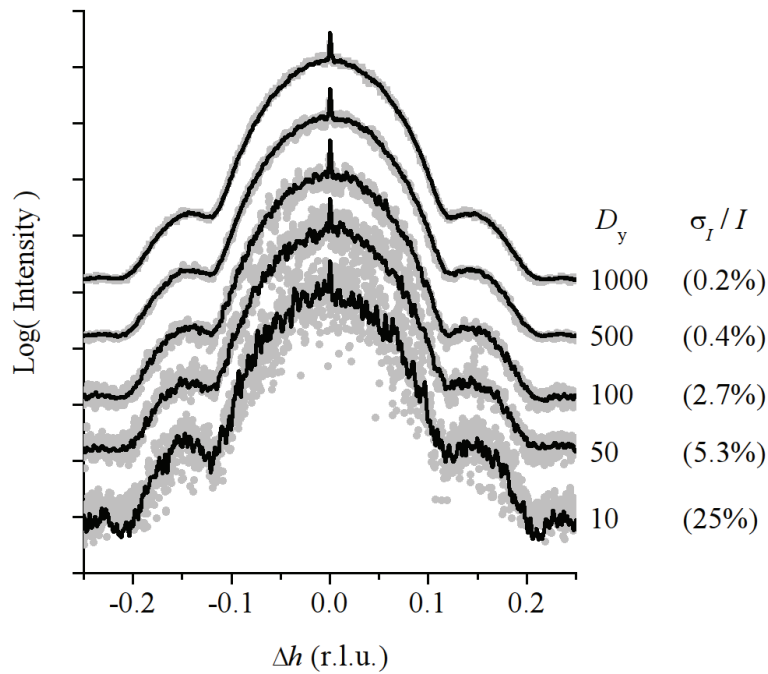


Figure 4.3.5: Computed h scans with increasing number of lattice planes in the y direction, indicated on the right (the numbers in brackets indicate the relative r.m.s deviation of the intensity, σ_I/I). Gray dots: without convolution; black lines: with convolution. The following defect characteristics were assumed: random distribution of spherical $R_1 = 5$ nm) defects with concentration $\langle c_1 \rangle = 10^{-5}$ defects per unit cell and lattice mismatch $\varepsilon = 5\%$. The curves are shifted vertically for clarity

obtained using the GPU instead of a classical CPU evaluation is displayed in Fig. (4.3.4). As expected, the speedup is mainly relevant for large array sizes, with a maximum efficiency (speedup = 45) around $N = 10^6$ unit-cells.

As mentioned earlier, the integration along the y direction leads to an incoherent addition of the inten-



sities scattered from the different (x, z) planes. The choice of the crystal dimension in this direction hence does not affect the shape the scattered intensity and can be used to adjust the computing times. It must, however, be borne in mind that higher values of D_y will improve the signal/noise ratio of the computed RSMs. Indeed, the FFT of a single (x, z) plane exhibits a complex fringes pattern (a speckle pattern) corresponding to the scattering from a given defect configuration. The summation over different planes along y smears out these patterns and produces the configuration-averaged signal, as measured experimentally. This situation is illustrated in Fig. (4.3.5) where h -scans [We here make use of the continuous Miller indices defined by $Q_x = \pi h$, $Q_y = 2\pi k/b$ and $Q_z = 2\pi l/c$ for an orthogonal unit-cell] computed at $\Delta l = -0.12$ corresponding to figure (4.4.1) are plotted. It can be readily observed that increasing the number of lattice planes in the y direction allows to reduce the level of noise in the computed curves, while the overall shape of the curves remain unchanged. This can be quantified by computing the root-mean-squared (rms) deviation of the scattered intensity σ_I . In this example, the maximum rms deviation (relative to the diffracted intensity, σ_I/I) ranges from 25% when only 10 lattice planes are used, to 0.2% for 1000 lattice planes. A smooth curve (with rms deviation of 0.4%) is obtained for 500 lattice planes.

The quality of the computed curves can be dramatically increased, while reducing the computing times, by convolving the computed curves with a blurring function. Experimentally, this corresponds to the resolution function of the diffractometer (which reflects the coherence properties of the beam), and which can be obtained either by the measurement of a perfect reference crystal, or calculated by taking into account the different elements in the beam path [18]. Eventually, this procedure should allow to quantitatively compare (fit) the computed curves with experimental data. For the moment, quantitative fitting of data is not considered and the resolution function is simply assumed to be a two-dimensional Gaussian with a full-width at half-maximum of 2×10^{-4} Å in both directions of reciprocal space (which correspond to an isotropic spatial coherence length of ≈ 3 μm). Fig. (4.3.5) shows that this procedure allows to obtain relatively smooth data from ~ 100 lattice planes (*i.e.* 5 times less than without convolution). Additionally, this procedure allows to clearly resolve tiny features in the curves, such as the narrow coherent Bragg peak located at $\Delta h = 0$, in situations where they are completely masked by the noise when no convolution is used.

4.4 APPLICATIONS TO IRRADIATED SINGLE CRYSTALS

4.4.1 RANDOMLY DISTRIBUTED SPHERICAL DEFECTS

As a first example, randomly distributed spherical defects in a large crystal is examined. We considered a crystal with $1000 \times 1000 \times 1000$ unit-cells with a 5 Å lattice parameter and $\nu = 0.3$. The defect radius is $R_1 = 5$ nm with a 5% lattice mismatch with the crystal and the defect concentration is $\langle c \rangle = 10^{-5}$ (*i.e.*, 10^4 defects). The result for the 004 reflection is displayed in Fig. (4.4.1). We obtain the well-known result,



corresponding to the DXS from isolated defects, where the RSM exhibits two asymmetrical lobes and fringes on each side of a nodal plane located at $\Delta l = 0$ [12]. An increase in the defect concentration only modifies to diffuse / coherent intensity ratio and not the shape of the DXS which solely depends on the defect radius and lattice mismatch. The secondary maximum located at $\Delta l \approx -0.12$ in figure (4.4.1) corresponds to the diffraction from the core of the defect. The RSM also exhibits two narrow streaks running along the h and l directions. These streaks correspond to the coherent scattering peak (visible in the center of the map) and are due to the finite crystal size. Such streaks are in general not observed in the scattering from single crystals as the dimensions of actual coherent domains are larger than the dimensions considered here (500 nm in each direction). The calculation lasted 26 minutes using our optimized approach (11 minutes to generate the displacement field, 15 minutes to compute the RSM), versus 83 hours using a non-parallel approach, *i.e.* a speedup of ~ 191 .

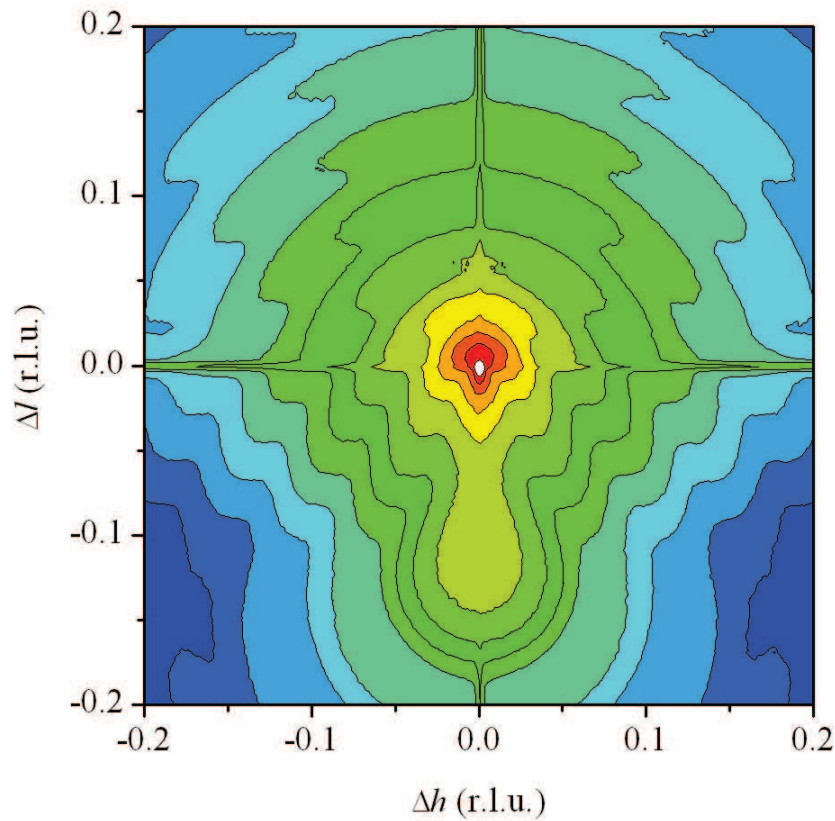


Figure 4.4.1: RSM of the 004 reflection of a crystal with $1000 \times 1000 \times 1000$ unit-cells containing randomly distributed spherical defects with radius $R_1 = 5nm$ and a lattice mismatch of $\epsilon = 5\%$. The logarithm of the intensity is plotted and each contour line corresponds to a $10^{0.5}$ variation. The intensity is truncated at $I_{max}/10$ (white region in the center) to highlight the DXS.



4.4.2 INHOMOGENEOUS DEFECT DISTRIBUTION : VARYING DEFECT SIZE

In this section, a slightly more complex system is taken into account. We consider a crystal of size $500 \times 500 \times 500$ unit cells with inhomogeneous defect distribution and with varying defect sizes. These defects were created with the concentration $\langle c \rangle = 0.01$ defects/unit-cell, $\nu = 0.3$ and the lattice mismatch $\varepsilon = 5\%$. Defects are randomly created in the crystal according to an arbitrary density function corresponding to the probability to observe a defect at given depth below the surface [Fig.4.4.2(a)]. The shape of the density function has been chosen so as to be similar to disorder profiles determined by ion channeling and X-ray diffraction [19] in actual irradiated crystal. A section of the computed two-dimensional strain field is shown in fig. [4.4.2(b)]. It can be seen that the defects produce tensile strain (white regions) in the 0-200 unit-cells range below the surface. For depth larger than 200 unit-cells, no tensile strain can be detected.

The computation was performed by multiprocessing using 8 processors for the displacement field calculation and GPU for intensity distribution. The calculations lasted approximately 4 hours to create

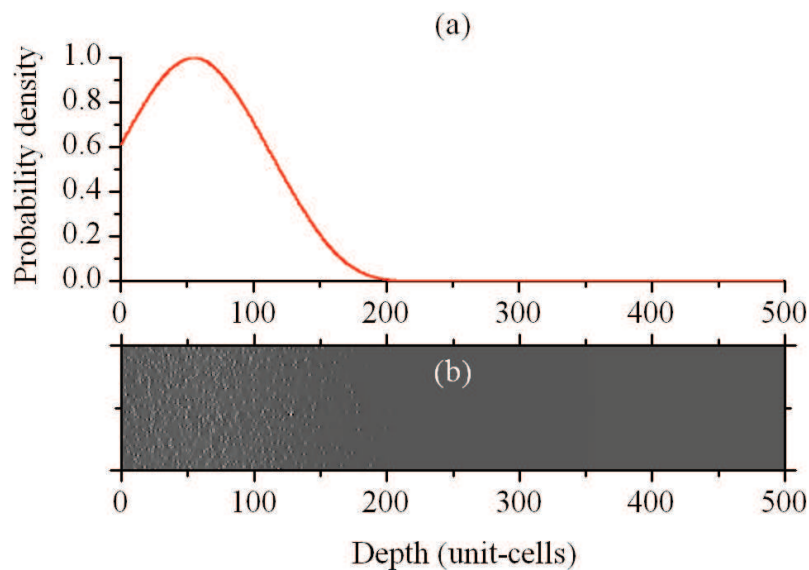


Figure 4.4.2: (a) Density function corresponding to the probability of finding a defect at a given depth below the surface (b) 100×500 unit cell section of a computed two-dimensional strain field. The defects are distributed according to the above density function and have radius $R_1 = 5\text{\AA}$ and mismatch $\varepsilon = 5\%$. White : tensile strain; black : compressive strain

1.25×10^6 defects. The 004 reciprocal space maps for defects of radius (a) $R_1 = 5\text{\AA}$ (Fig. 4.4.3a); (b) $R_1 = 15\text{\AA}$ (Fig. 4.4.3b); (c) $R_1 = 25\text{\AA}$ (Fig. 4.4.3c) are illustrated. From the RSM for the first case, we can mainly observe two interesting features. Firstly, it exhibits an elongated streak parallel to the l direction, with the Bragg peak at $\Delta l = 0$. This originates from the virgin part of the crystal. A secondary maximum at $\Delta l = -0.04$ is a result of the strained part of the crystal. This signal is typical in irradiated

materials exhibiting dilatation gradient in the direction perpendicular to the surface and has been studied in the previous chapter (Figure 4.4.3 d). The simulation result shows that a dilatation gradient can be produced in irradiated crystals with heterogeneous distribution of unit-cell-sized defects.

In the second case, with the increase of defect size, the intensity decreases and surprisingly, the strain

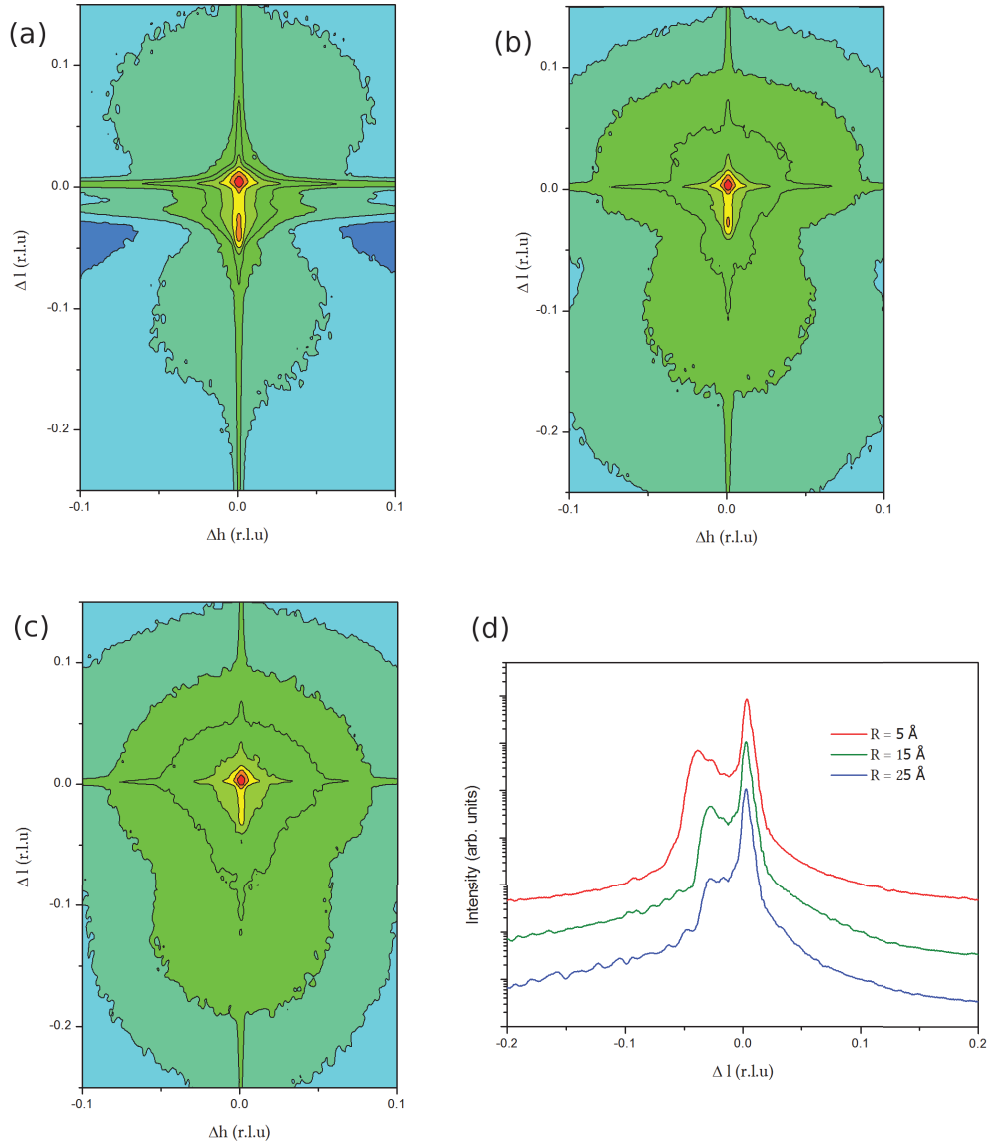


Figure 4.4.3: Calculated diffuse intensities for a 004 reflection of a crystal with $500 \times 500 \times 500$ unit-cells containing randomly distributed spherical defects with defects of radius (a) $R_1 = 5\text{\AA}$; (b) $R_1 = 15\text{\AA}$; (c) $R_1 = 25\text{\AA}$. In all maps, the logarithm of the intensity is plotted and each contour line corresponds to a $10^{0.5}$ variation. (d) I -scans extracted at $\Delta h = 0$ which shows the damage-induced streak. The red, green and blue lines correspond to scans extracted from (a), (b) and (c), respectively. The curves are shifted by $\times 10$ variation for clarity.

is lowered. This implies that small defects are very effective in producing homogeneous strain and contrarily to bigger defects. On the other hand, bigger defects are effective in distorting the crystal lattice

heterogeneously. This gives rise to the Debye-Waller factor which is responsible for the lowering of the intensity and the appearance of diffuse scattering. This can be clearly observed in the final case for the defect size of $R_1 = 25\text{\AA}$. The result shows an intense diffuse X-ray scattering and the damage-induced streak reduces to a very weak peak on the lower l side of the Bragg peak. It is striking to observe the similarity with the results obtained from the actual experiments. In the previous chapter, a relationship between the strain and the DW factor was presented and here it is effectively demonstrated in terms of defects.

4.4.3 INHOMOGENEOUS DEFECT DISTRIBUTION : VARYING MISFIT

Similar to the above example, the behaviour of a crystal with inhomogeneous defect distribution was investigated for different lattice mismatches. Figure (4.4.4) shows the RSMs for a crystal with $500 \times 500 \times 500$ unit-cells with lattice mismatches of (a) $\varepsilon = 2.5\%$, (b) $\varepsilon = 5\%$ and (c) $\varepsilon = 7.5\%$. Small defects of radius $R_2 = 5\text{\AA}$ were created with the concentration $\langle c \rangle = 0.01$ defects/unit-cell, $\nu = 0.3$. The computation was performed by multiprocessing using 8 processors for the displacement field calculation and GPU for intensity distribution.

In the first case, we observe an elongated streak parallel to the l direction, with the Bragg peak emanating from the virgin part of the crystal at $\Delta l = 0$ and a secondary maximum located at $\Delta l = -0.07$. Vertical l scans extracted at $\Delta h = 0$ is displayed in fig. (4.4.4). Note that for higher lattice mismatch, the intensity is shifted towards lower l values as a consequence of the increased lattice mismatch, but the position of the secondary peak is not directly related to defect misfit.

4.4.4 INHOMOGENEOUS DEFECT DISTRIBUTION : VARYING DEFECT CONCENTRATION

Figure (4.4.5) displays the results of the RSMs for a 004 reflection of a crystal containing $500 \times 500 \times 500$ unit-cells with varying defect concentrations (a) $\langle c \rangle = 0.01$, (b) $\langle c \rangle = 0.075$ and (c) $\langle c \rangle = 0.005$. The results follow a similar trend as in the previous two cases. It exhibits an elongated streak parallel to the l direction, with the Bragg peak at $\Delta l = 0$. A secondary maximum at $\Delta l = -0.08$ is a result of the strained part of the crystal. With these simulations, it is evident that the observed strain is proportional to the concentration of defects. With the increase in concentration, the amount of strain increases, which can be clearly noted in figure (4.4.5 d).

In summary, inhomogeneous defect distribution was investigated in detail with the variation of defect size, defect concentration and the misfit. The relationship between the strain and the DW factor was explained in terms of defects. It is possible to create a dilatation gradient as observed in irradiated crystal with an inhomogeneous distribution of unit-cell-sized defects. Furthermore, it was observed that small defects are very effective in producing homogeneous strain and bigger defects are effective in distorting



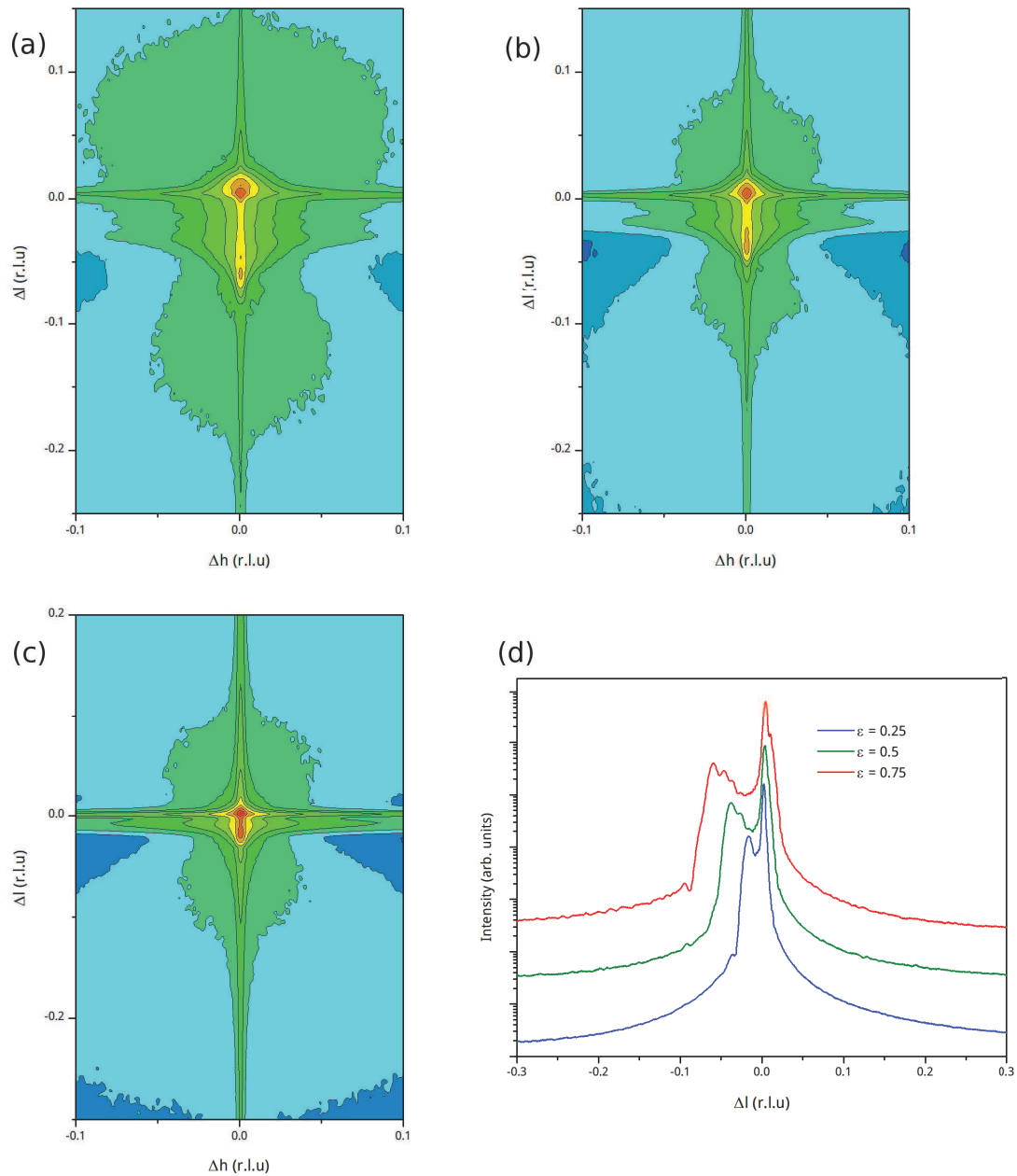


Figure 4.4.4: Calculated diffuse intensities for a 004 reflection of a $500 \times 500 \times 500$ crystal containing randomly distributed spherical defects with a lattice mismatch of (a) $\varepsilon = 2.5\%$, (b) $\varepsilon = 5\%$ and (c) $\varepsilon = 7.5\%$. The logarithm of the intensity is plotted; each contour line corresponds to a $10^{0.5}$ variation. (d) I - scans extracted at $\Delta h = 0$ which shows the damage-induced streak. The red, green and blue lines correspond to scans extracted from (a), (b) and (c), respectively. The curves are shifted by $\times 10$ variation for clarity.



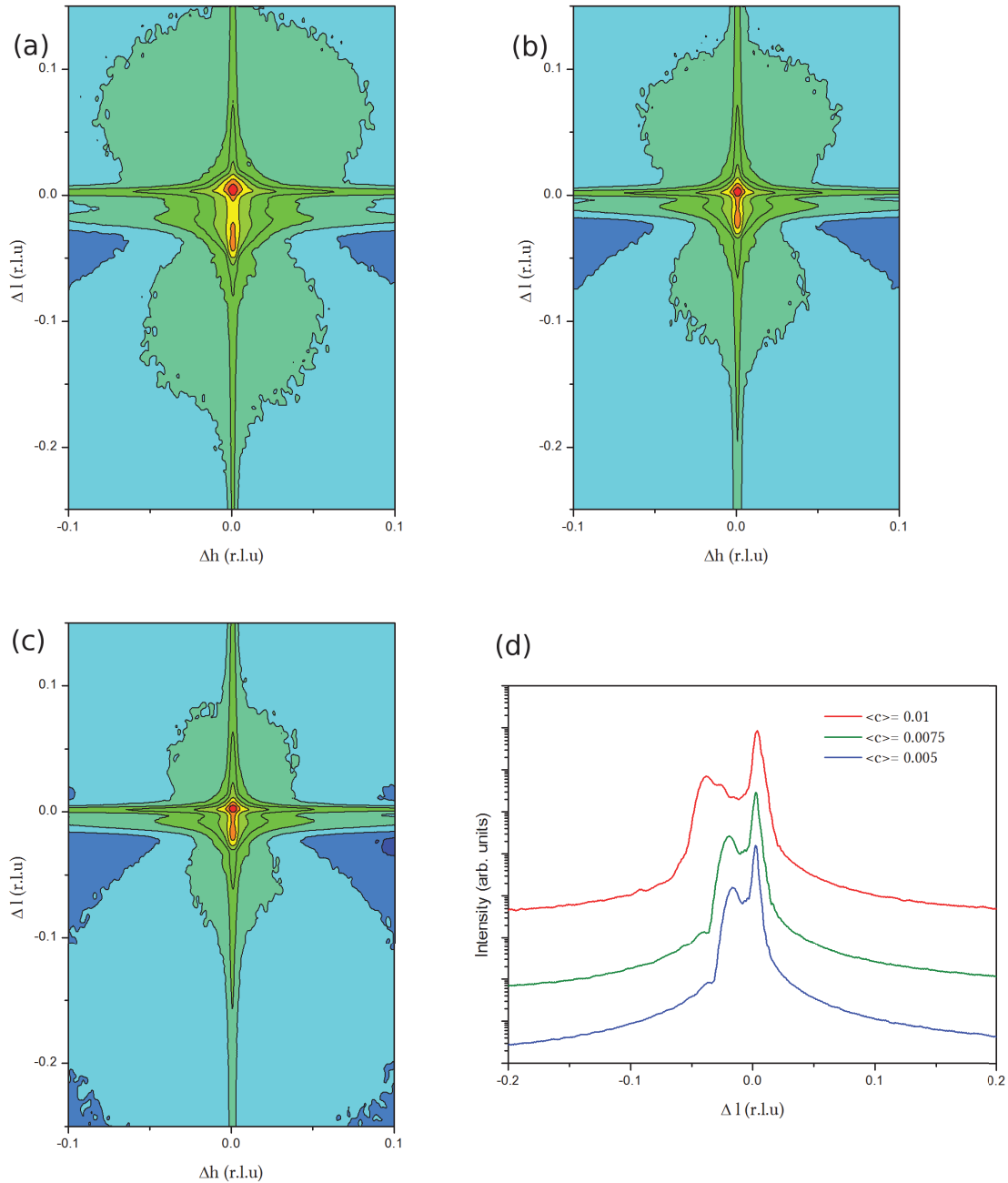


Figure 4.4.5: Calculated diffuse intensities for a 004 reflection of a crystal containing $500 \times 500 \times 500$ unit-cells with varying defect concentrations such as (a) $\langle c \rangle = 0.01$, (b) $\langle c \rangle = 0.075$ and (c) $\langle c \rangle = 0.005$. The logarithm of the intensity is plotted; each contour line corresponds to a $10^{0.5}$ variation. (d) I -scans extracted at $\Delta h = 0$ which shows the damage-induced streak. The red, green and blue lines correspond to scans extracted from (a), (b) and (c), respectively. The curves are shifted by $\times 10$ variation for clarity.

heterogeneously the crystal lattice which gives rise to the Debye-Waller factor. It was also shown that the observed strain from peak position is not related directly to the misfit. It is a complex mixture between the defect size, concentration and the lattice mismatch. Equipped by these results, we take a step ahead

to simulate the RSMs of Yttria-stabilized zirconia.

4.4.5 SIMULATION OF RSMs OF YSZ

In this section, simulation of the behaviour of real crystals under irradiation is tentatively performed. We consider the example of yttria-stabilized zirconia (YSZ) single crystals, whose behaviour under different irradiation conditions was discussed in the previous chapter. To summarize, the damage build-up upon increasing ion fluence takes place by a multi-step process, with each step occurring in order to lower the system's free energy. In the first step, point-defects, mainly Frenkel pairs, are formed in a sub-surface region whose extension varies from 100 nm to a few hundreds of nanometers, depending on the nature and energy of the incident ions (the defect distribution in the damaged region being non-uniform). In the next steps, these point defects coalesce to form larger (a few nanometers) point-defect clusters. The defect mobility can be increased by performing irradiation at high temperature which results in a shift of the different steps towards lower fluences, *i.e.* the increased defect mobility favors defect clustering at lower fluences.

The microstructure of the irradiated of YSZ single crystals is modelled using the simulation procedure detailed in the section (4.3). The computation was performed for a crystal of size $500 \times 500 \times 500$ unit cells containing non uniform and bimodal distribution of defects. These defects were created with the defect concentration $\langle c \rangle = 0.01$ defects/unit-cell, $\nu = 0.3$ and the lattice mismatch $\varepsilon = 5\%$. The computation required about 4 hours for the first case but significantly reduced for big defects. The corresponding 004 RSM is shown in Fig. (4.4.6) and selected scans in Fig. [4.4.6 (d, e)]. The RSM displays an elongated streak parallel to the l direction, with the Bragg peak (emanating from the virgin part of the crystal) located at $\Delta l = 0$ and a secondary maximum located at $\Delta l = -0.04$. This signal is typical of irradiated materials exhibiting a dilatation gradient in the direction perpendicular to the surface [20] as shown previously. In addition, it can be seen that the DXS is extremely weak and drops rapidly down to values 10^5 times lower than the coherent signal, *i.e.* the intensity is mainly concentrated within the damage-induced streak. It can also be noticed that, in addition to the vertical streak, a horizontal streak (at $\Delta l = 0$) is also observed. This corresponds to the crystal truncation rods and is due to the finite dimensions of the crystal used in the calculation. This latter streak is in general not observed in the scattering from single crystals as the dimensions of actual coherent domains are larger than the dimensions considered here (500 unit-cells).

In a second step, a structure where 25% of the initial defects were allowed to coalesce to form larger defects with $R_2 = 5$ nm is generated. The corresponding RSM is given in Fig.4.4.6 (b). The intensity of the damage-induced streak is lowered and, concomitantly the DXS intensity considerably increases (as revealed by the spreading of the intensity in the h direction). This feature shows that, whereas smaller defects are efficient in producing homogeneous strain within the damaged region of the crystal, the larger defects mostly give rise to heterogeneous strain as shown in the previous section. Finally, in the last step, only large defects remain, and the trend observed previously is continued, Fig. 4.4.6 (c). The



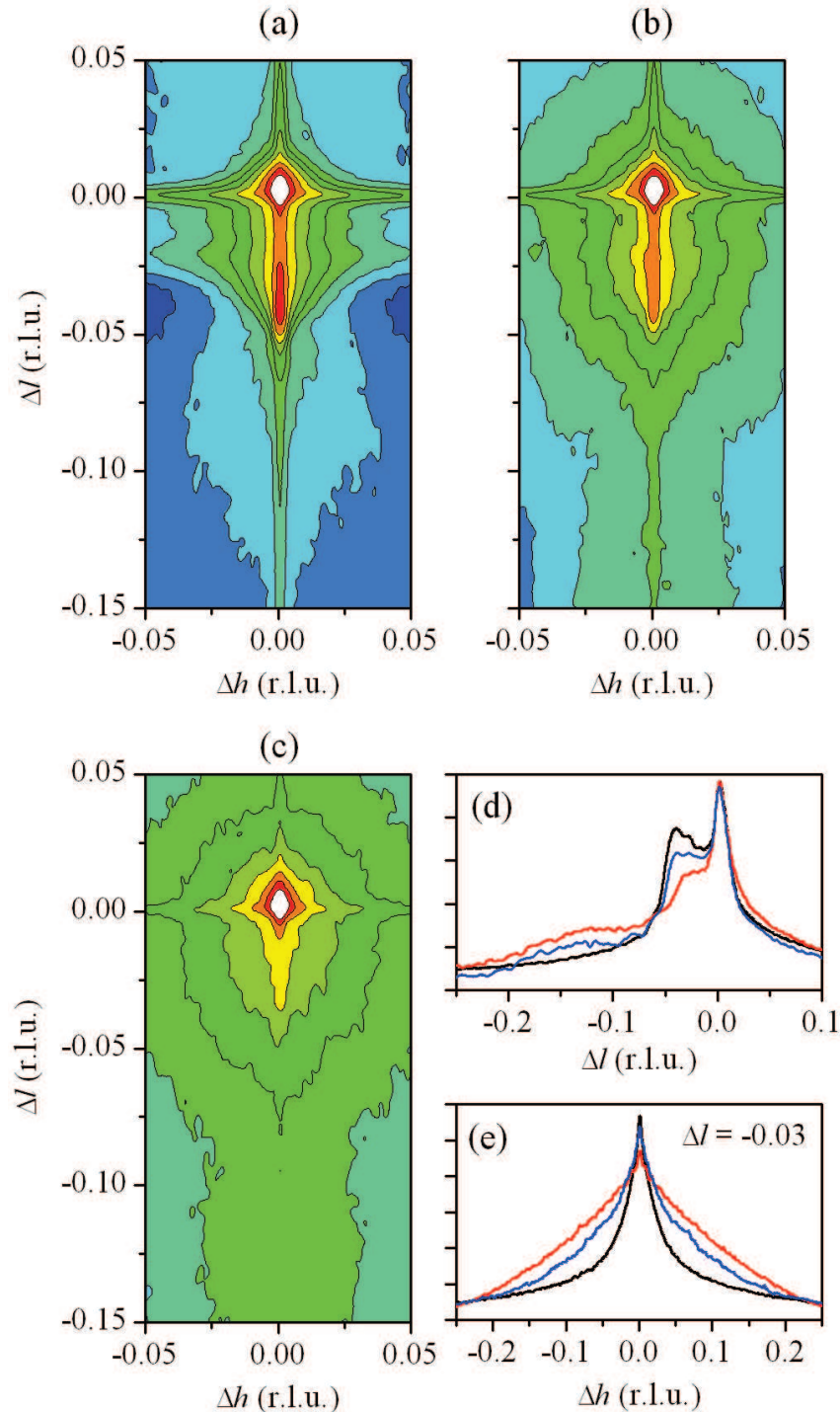


Figure 4.4.6: Computed 004 RSMs with a non-uniform and bimodal distribution of defects: (a) only small defects ($R_1 = 5 \text{ \AA}$); (b) small and large defects ($R_1 = 5 \text{ \AA}$ and $R_2 = 5 \text{ nm}$); (c) only large defects ($R_2 = 5 \text{ nm}$). In all maps, the logarithm of the intensity is plotted; each contour line corresponds to a $10^{0.5}$ variation. The intensity is truncated at $I_{max}/10$ (white region in the center) to highlight the diffuse X-ray scattering. (d) l -scans extracted at $\Delta h = 0$ evidencing the damage-induced streak. (e) h -scans extracted at $\Delta l = -0.03$ evidencing the DXS intensity. The black, blue and red lines correspond to scans extracted from (a), (b) and (c), respectively. Each graduation corresponds to a $\times 10$ variation.

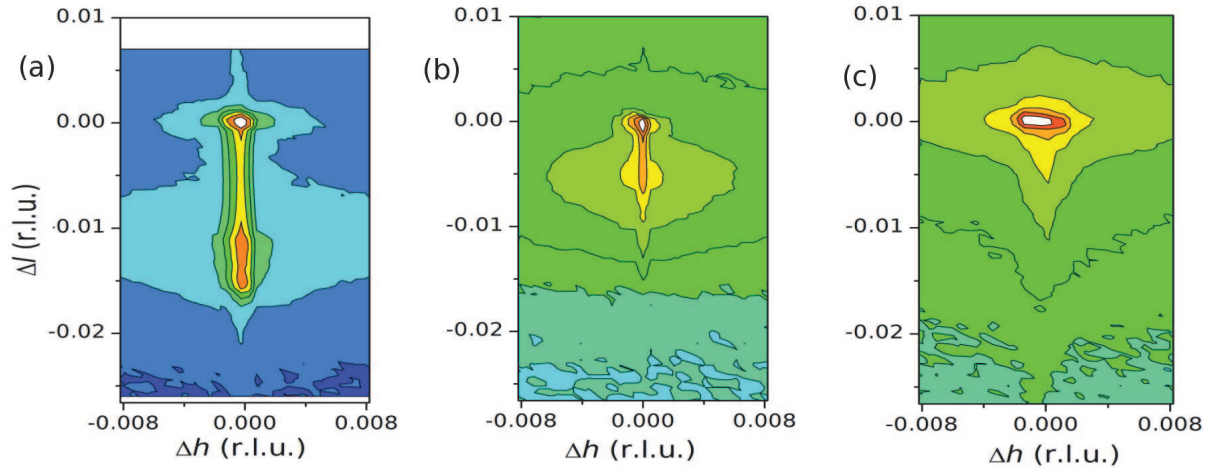


Figure 4.4.7: Reciprocal space maps recorded in the vicinity of the (400) Bragg reflection for YSZ crystals irradiated with 4 MeV Au^{2+} ions at the fluence of $10^{15} cm^{-2}$ and at temperatures (a) 80 K (b) 573 K and (c) 1073 K.

damage-induced streak is now reduced to a weak peak on the lower l side of the main Bragg peak, and the DXS forms an intense, elliptically shaped halo around the Bragg peak. These features are in remarkable qualitative agreement with the tendency observed in YSZ. Reciprocal space maps recorded in the vicinity of the (400) Bragg reflection for YSZ crystals irradiated with 4 MeV Au^{2+} ions at the fluence of $10^{15} cm^{-2}$ with increasing temperatures is given in figure (4.4.7). RSM for the sample irradiated at 80 K is characteristic of the first step of the damage build-up, 573 K corresponds to the beginning of the second step and the last map for the crystal irradiated at 1073 K. This corresponds to the damage accumulation process in which the point defects are created in the first stage which later coalesce to form defect clusters. It should be noted that the extensions of the RSMs are quantitatively different since the conditions considered in our model might not be exactly as in the real case. For example, the information regarding the defect size is only approximately known in the real crystals. Additionally, very little is known about the inner structure of the defect clusters, so that the defect mismatch and the scattering density are unknown. More studies are required to refine these aspects.

4.4.6 SPATIALLY CORRELATED DEFECTS

An interesting feature in the irradiation of materials is the spontaneous formation of ordered nanostructures, which is mainly observed in face-centered cubic and body-centered cubic metals. These nanostructures include, among others, self-organized three-dimensional superstructure of voids (vacancy clusters), gas bubbles or dislocation loops with varying degree of disorder [21]. In this section we investigate the effects of spatially correlated defects, in the case of long-range order (LRO) and short-range order (SRO) spatial correlations and with a varying degree of disorder. For simplicity we assumed a cubic ordering, but any type of array can be straightforwardly implemented. Additionally in order not to overly complicate the RSMs we only consider the effect of ordering of defects of the same size and

don't take into account the previous depth gradient. It must be emphasized, however, that any constraint

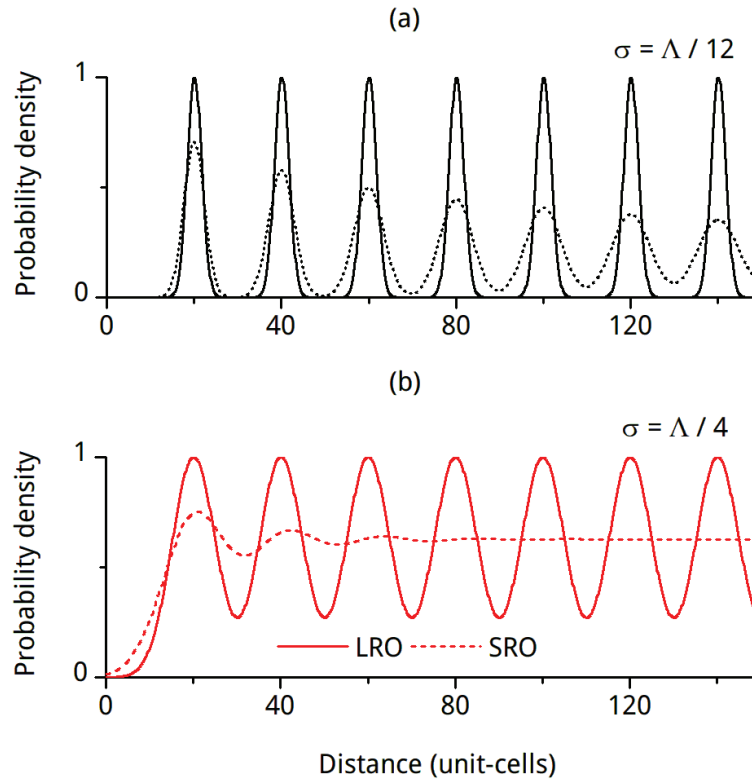


Figure 4.4.8: Probability density function in the case of low (a) and high (b) positional disorder, for LRO (continuous lines) and SRO (dotted lines).

on the defects positions or defect sizes can be easily implemented without any additional computational cost. For the sake of modeling spatial correlation we use the following probability density function

$$p(x) = \sum_n g(x) \times \delta(x - n\Lambda) \quad (4.14)$$

which corresponds to the probability of finding a defect at a distance x from another defect, Λ being the period of the array. The function $g(x)$ describes the positional probability density function at each node of the superstructure. In the case of LRO it was assumed to be a Gaussian with a fixed standard deviation, σ_0 , whereas in the case of SRO, the standard deviation was assumed to vary in a random-walk type fashion, $\sigma_n = n^{1/2}$ [22]. The corresponding density functions, with $\Lambda = 20$ unit-cells, are plotted in fig. (4.4.8) in the case of a low ($\sigma_0 = \Lambda / 12$) and a high ($\sigma_0 = \Lambda / 4$) positional disorder. Increasing the standard deviation widens the peaks of the probability density function resulting in an increased disordering (*i.e.* the probability of finding a defects never drops down to 0). In the case of SRO, this eventually leads to correlations restricted to the first neighbour.

The computed RSMs (with defect radius $R_1 = 2.5$ nm, *i.e.*, 5 unit-cells, and $\varepsilon = 5\%$) corresponding to



each case are displayed in Fig.(4.4.9) and (4.4.10). We first discuss the case of LRO (Fig. 4.4.9). In the

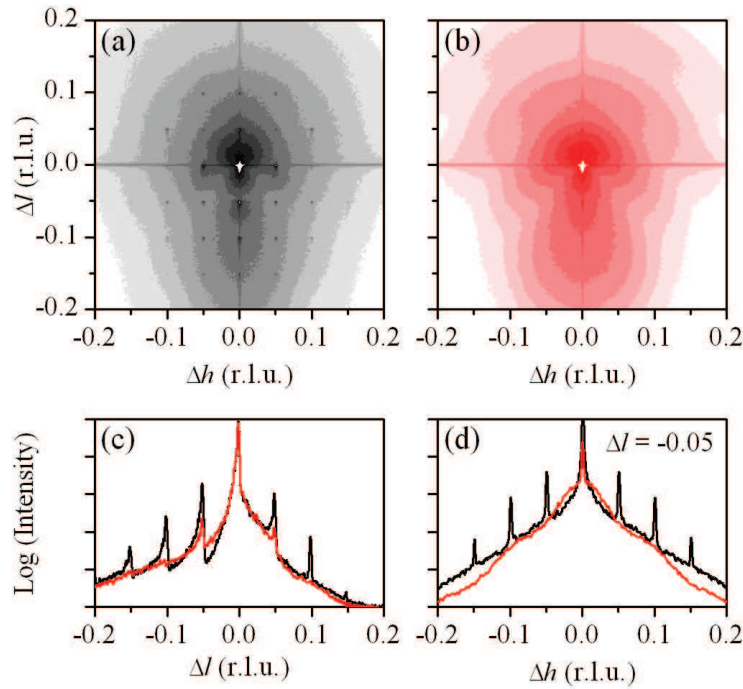


Figure 4.4.9: Computed 004 RSMs in the case of spherical defects with LRO spatial correlations: (a) low positional disorder ($\sigma_0 = \Lambda / 12$); (b) high positional disorder ($\sigma_0 = \Lambda / 4$). In all maps the logarithm of the intensity is plotted; each contour line corresponds to a $10^{0.5}$ variation. The intensity is truncated at $I_{max} / 10$ (white region in the center) to highlight the DXS. (d) l -scans extracted at $\Delta h = 0$ evidencing the superstructure peaks. (e) h -scans extracted at $\Delta l = -0.05$ evidencing the DXS intensity and the superstructure peaks. The black and red lines correspond to scans extracted from (a) and (b), respectively. Each graduation corresponds to a $\times 10$ variation.

case of low positional disorder (Fig. 4.4.9 a), the DXS is elliptically shaped with clearly visible superstructure peaks occurring for $\Delta h, \Delta l = n / \Lambda = n \times 0.05$ (n being an integer). The superstructure peaks occur along the coherent CTR (Fig. 4.4.9 c) but also in the DXS (Fig. 4.4.9 d). The intensity of the superstructure peaks is modulated by Debye-Waller – like factor, $\exp(-2\pi^2 n^2 \sigma_0^2)$, so that for low disorder superstructure peaks are visible up to high orders n . On the contrary, as shown in Fig. (4.4.9 b) and in the scans Fig (4.4.9 c) and (4.4.9 d), for increased disorder only the first order peaks are visible, and the diffuse scattering has a structured shape corresponding to the DXS from isolated defects, where the RSM exhibits two asymmetrical lobes and fringes on each side of a nodal plane located at $\Delta l = 0$ [12]. The broad secondary maximum located at $\Delta l \approx -0.12$ corresponds to the diffraction from the core of the defects. The peak shift is due to the strain inside the defect which gives rise to the observed shift of $-l \times \varepsilon \times (1 + \nu) / [3(1 - \nu)] = -0.124$ (with $\nu = 0.3$).

The case of SRO is displayed in Fig. (4.4.10). It can be readily observed that SRO leads to much less

pronounced superstructure features. This can be explained by the fact that, in the case of a random walk model, the width of the superstructure peaks scale as $n^2\sigma_0^2$ [22], so that high order peaks are smeared out, even for relatively small values of σ_0 . Therefore, for SRO, the low disorder case is similar to the high disorder case of LRO, in particular regarding the overall shape of the DXS. A closer inspection, however, reveals that the width of the first order peak is higher in the case of SRO than in LRO, in agreement with the previous statement. For higher disorder, although first neighbor correlations are present, no particular features can be detected in the RSM which correspond to the RSM from isolated point defects.

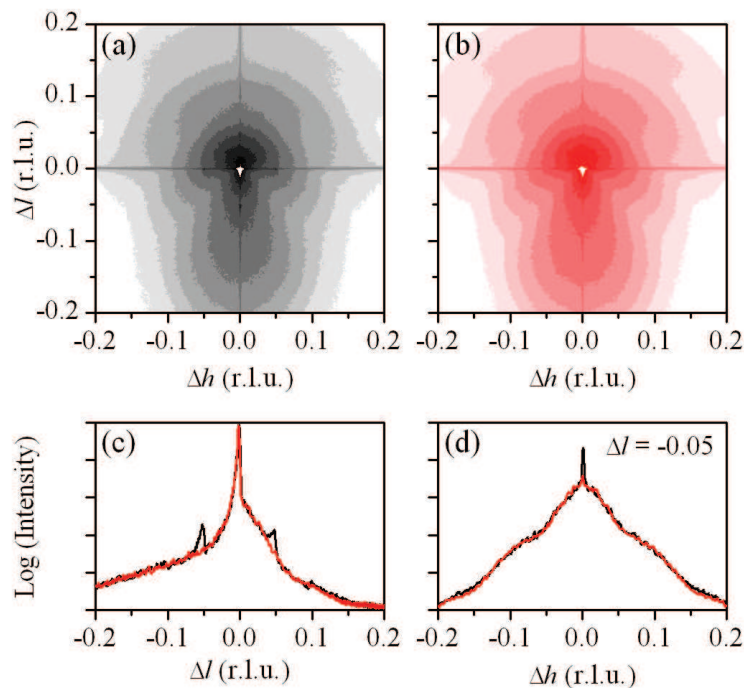


Figure 4.4.10: Computed 004 RSMs in the case of spherical defects with SRO spatial correlations: (a) low positional disorder ($\sigma_0 = \Lambda / 12$); (b) high positional disorder ($\sigma_0 = \Lambda / 4$). In all maps the logarithm of the intensity is plotted; each contour line corresponds to a $10^{0.5}$ variation. The intensity is truncated at $I_{max} / 10$ (white region in the center) to highlight the DXS. (d) l -scans extracted at $\Delta h = 0$ evidencing the superstructure peaks. (e) h -scans extracted at $\Delta l = -0.05$ evidencing the DXS intensity and the superstructure peaks. The black and red lines correspond to scans extracted from (a) and (b), respectively. Each graduation corresponds to a $\times 10$ variation.

4.5 CONCLUSION

In this chapter, a computational method for the evaluation of the displacement field induced by defects in irradiated materials and the corresponding XRD reciprocal space maps are presented. The total

displacement field of the damaged crystals is calculated using a Monte Carlo method where the displacement fields of individual defects are summed up. This step combines vector programming and multiprocessing to speedup the calculation. The RSMs are obtained from the incoherent sum of Fourier transforms of two-dimensional slices of the correlation function. This part is computed on the GPU making use of optimized FFT algorithms. The model was tested by simulating different defect distributions. Inhomogeneous defect distributions with the variation of defect size, misfit and the defect concentration was presented. It was noted that small defects are very effective in producing homogeneous strain and on the other hand, bigger defects are effective in distorting the crystal lattice heterogeneously which gives rise to the DW factor. In the last part, we showed the success of this approach by modelling the DXS of irradiated zirconia single crystals containing a non-uniform defect depth-distribution and undergoing defect clustering. The proposed approach allows to qualitatively reproduce the main features observed in actual RSMs recorded from such crystals.

This approach is clearly not limited to the study of irradiated crystals and can be used for a broad range of systems, as long as the displacement field of the defects can be computed. Indeed, for very high defect concentrations, the relevance of the use of the displacement field from individual defects to compute the total displacement field can probably be questioned. Additionally, for high defect concentrations the computation times of the displacement field become prohibitively long, even with the improvements presented in this work, so that an alternate method is preferable.

On the contrary, the GPU-accelerated approach to compute the RSMs from the displacement field is solely dependent on the crystal size, and its efficiency is independent of the complexity of the displacement field. It can hence be straightforwardly combined with any computational method that allows to compute the displacement field. Moreover, the fast-growing computing power of the GPUs will certainly allow to study crystals with increased dimensions in the very near future.



REFERENCES

- [1] P. Dederichs, "The theory of diffuse x-ray scattering and its application to the study of point defects and their clusters," *Journal of Physics F: Metal Physics*, vol. 3, no. 2, p. 471, 1973.
- [2] V. Holy, T. Baumbach, and U. Pietsch, *High-resolution X-ray scattering from thin films and multilayers*. Springer, 1999.
- [3] P. Dederichs, "Diffuse scattering from defect clusters near bragg reflections," *Physical Review B*, vol. 4, no. 4, p. 1041, 1971.
- [4] B. C. Larson and W. Schmatz, "Huang diffuse scattering from dislocation loops and cobalt precipitates in copper," *Physical Review B*, vol. 10, no. 6, p. 2307, 1974.
- [5] P. Ehrhart, H. Trinkaus, and B. Larson, "Diffuse scattering from dislocation loops," *Physical Review B*, vol. 25, no. 2, p. 834, 1982.
- [6] U. Beck, T. Metzger, J. Peisl, and J. Patel, "Diffuse x-ray rods and scattering from point defect clusters in ion implanted silicon," *Applied Physics Letters*, vol. 76, no. 19, pp. 2698–2700, 2000.
- [7] K. Nordlund, U. Beck, T. Metzger, and J. Patel, "Diffuse x-ray streaks from stacking faults in Si analyzed by atomistic simulations," *Applied Physics Letters*, vol. 76, no. 7, pp. 846–848, 2000.
- [8] K. Nordlund, P. Partyka, R. Averback, I. Robinson, and P. Ehrhart, "Atomistic simulation of diffuse x-ray scattering from defects in solids," *Journal of Applied Physics*, vol. 88, no. 5, pp. 2278–2288, 2000.
- [9] W. Xu and J. A. Moriarty, "Atomistic simulation of ideal shear strength, point defects, and screw dislocations in bcc transition metals: Mo as a prototype," *Physical Review B*, vol. 54, no. 10, p. 6941, 1996.
- [10] J. Channagiri, A. Boulle, and A. Debelle, "Diffuse x-ray scattering from ion-irradiated materials: a parallel-computing approach," *Journal of Applied Crystallography*, vol. 48, no. 1, pp. 252–261, 2015.
- [11] M. A. Krivoglaz, *X-ray and neutron diffraction in nonideal crystals*. Springer, 1996.
- [12] U. Pietsch, V. Holy, and T. Baumbach, *High Resolution X-ray Scattering: From thin films to lateral nanostructures*. 2004. New York, NY: Springer-Verlag.
- [13] Y. I. Nesterets and V. I. Punegov, "The statistical kinematical theory of X-ray diffraction as applied to reciprocal-space mapping," *Acta Crystallographica Section A: Foundations of Crystallography*, vol. 56, no. 6, pp. 540–548, 2000.



- [14] C. Teodosiu, *The Elastic Field of Point Defects*. Springer, 1982.
- [15] V. Favre-Nicolin, J. Coraux, M.-I. Richard, and H. Renevier, “Fast computation of scattering maps of nanostructures using graphical processing units,” *Journal of Applied Crystallography*, vol. 44, no. 3, pp. 635–640, 2011.
- [16] S. Van Der Walt, S. C. Colbert, and G. Varoquaux, “The NumPy array: a structure for efficient numerical computation,” *Computing in Science & Engineering*, vol. 13, no. 2, pp. 22–30, 2011.
- [17] M. Schmeisser, B. C. Heisen, M. Luettich, B. Busche, F. Hauer, T. Koske, K.-H. Knauber, and H. Stark, “Parallel, distributed and GPU computing technologies in single-particle electron microscopy,” *Acta Crystallographica Section D: Biological Crystallography*, vol. 65, no. 7, pp. 659–671, 2009.
- [18] A. Boulle, O. Masson, R. Guinebretière, A. Lecomte, and A. Dauter, “A high-resolution x-ray diffractometer for the study of imperfect materials,” *Journal of applied crystallography*, vol. 35, no. 5, pp. 606–614, 2002.
- [19] A. Debelle, J. Channagiri, L. Thomé, B. Décamps, A. Boulle, S. Moll, F. Garrido, M. Behar, and J. Jagielski, “Comprehensive study of the effect of the irradiation temperature on the behavior of cubic zirconia,” *Journal of Applied Physics*, vol. 115, no. 18, p. 183504, 2014.
- [20] A. Boulle and A. Debelle, “Strain-profile determination in ion-implanted single crystals using generalized simulated annealing,” *Journal of Applied Crystallography*, vol. 43, no. 5, pp. 1046–1052, 2010.
- [21] N. Ghoniem, D. Walgraef, and S. Zinkle, “Theory and experiment of nanostructure self-organization in irradiated materials,” *Journal of computer-aided materials design*, vol. 8, no. 1, pp. 1–38, 2001.
- [22] M. Schmidbauer, *X-ray diffuse scattering from self-organized mesoscopic semiconductor structures*, vol. 199. Springer Science & Business Media, 2004.



Appendix I

In this Appendix, the whole program written using the Python multiprocessing and GPU parallel programming is presented.

```
#!/usr/bin/env python
# -*- coding: utf-8 -*-
# Python program for the study of Diffuse X-ray scattering in irradiated
# materials.
# Program_DXS.py
# (c) 2015 Jayanth Channagiri, Alexandre Boulle, Aurélien Debelle
# Copyright SPCTS - UMR CNRS 7315
# Université de Limoges

#*****Importing required Python packages*****
import sys
import matplotlib.pyplot as plt
from numpy import *
from scipy import special
from scipy.signal import fftconvolve
import random
import multiprocessing as mp
#*****Importing required Python packages for GPU*****
import pycuda.gpuarray as gpuarray
import pycuda.cumath
from pyfft.cuda import Plan
import pycuda.driver as cuda
from pycuda.tools import make_default_context
import pycuda.gpuarray as gpuarray

#*****Initiating the NVIDIA GPU*****
cuda.init()
context = make_default_context()
```



```

stream = cuda.Stream()

##### Defect relative structure factor #####
def rel_SF(u):
    out = ones(shape(u))
    uder = (u[:,1:] - u[:, :-1])/d0
    e_max = misfit * (1+nu) / ((1-nu)*3.)
    F_vacancy = 1
    out[uder>= e_max-0.0001] = F_vacancy
    return out

##### Defects displacement functions using Weave#####
# Spherical cluster with coulombian displacement
def u_coulomb_weave(xt, zt, yt, x0, z0, y0, misfit, R0):
    q = shape(xt)[0]
    r = shape(zt)[1]
    s = shape(yt)[2]
    u = zeros((q, r, s), dtype = 'float')
    A = misfit * (R0**3) * (1+nu) / ((1-nu)*3.)
    code = """
        float R;
        int i, j,k,d0;
        d0 = 5;
        for (i= 0; i<q;i++)
        {
            for (j=0;j<r;j++)
            {
                for (k=0;k<s;k++)
                {
                    R = sqrt(((i*d0)-x0)*((i*d0)-x0) + ((k*d0)-y0)*((k*d0)-y0)+
                        ((j*d0)-z0)*((j*d0)-z0));
                    if(R>=R0)
                    {
                        U3(i, j, k) = (A* ((j*d0) - z0)) / (R*R*R + 1e-9);
                    }
                    else
                    {
                        U3(i, j, k) = (A* ((j*d0) - z0)) / (R0*R0*R0 + 1e-9);
                    }
                }
            }
        }
    """

```



```

    }
}
"""
weave.inline(code, ['u', 'q', 'r', 's', 'x0', 'y0', 'z0', 'A', 'R0'])
return u

#*****Disordered crystal generation function performed using GPU*****
# correlation function
def generate_G_gpu(u_cal, a , order):
    return pycuda.cumath.exp(2*pi*1j*(order/a)*u_cal)

#***** strain gradient functions *****
def f_strain_spline3_smooth(alt, sp, th):
    w_strain_free = sp[:]
    w_strain = array([0.0,0.0,0.0])
    w_strain = append(w_strain,w_strain_free)
    N_abscisses = len(w_strain) - 3.
    zz = alt * N_abscisses / th
    index = 0
    strain = ones(len(zz))
    for i in zz:
        strain[index] = cubicSpline(i,w_strain) / 100.
        index = index + 1
    return strain

def create_u_straingradient(x, z, y, sp, sizex, sigx1, sigx2, sizez, sigz1,
    sigz2, sizey, sigy1, sigy2):
    maxsizez = (sizez + 3 * (sigz1 + sigz2))/d0
    uz = f_strain_spline3_smooth(z[0,:maxsizez:], sp,sizez)*d0
    return uz[:maxsizez:].cumsum().reshape(1, maxsizez, 1)

#*****Template displacement field generation*****
# Template displacement field is generated for a crystal of twice the size
the dimensions of the actual crystal in all directions containing a
defect in its center. From this template, any displacement field
corresponding to the actual crystal is extracted.

def create_u_template(c_def, misfit, R0, R0c, sizex, sigx1, sigx2, sizez,
    sigz1, sigz2, sizey, sigy1, sigy2):
    maxsizex = int((sizex + 3 * (sigx1 + sigx2))/d0)

```



```

maxsizez = int((sizez + 3 * (sigz1 + sigz2))/d0)
maxsizey = int((sizey + 3 * (sigy1 + sigy2))/d0)
maxsizey = maxsizey/Nprocs
xt, zt, yt = arange(0, (maxsizex*2)*d0, x_step), arange(0, (maxsizez*2)*d0,
    z_step), arange(0, (maxsizey*2)*d0, y_step)
xt = xt.reshape(len(xt),1, 1)
zt = zt.reshape(1,len(zt), 1)
yt = yt.reshape(1, 1, len(yt))
uc = u_coulomb(xt, zt, yt, maxsizex*d0, maxsizez*d0, maxsizey*d0, misfit,
    R0, R0c)
return uc

#*****Displacement field calculation for non-uniform bimodal
distribution of defects using multiprocessing*****
def create_u_defects_2_defects_grad(x, z, y, c_def, f_size2, sp, misfit, R0,
    R02, R0c, sizex, sigx1, sigx2, sizez, sigz1, sigz2, sizey, sigy1, sigy2):
maxsizex = int((sizex + 3 * (sigx1 + sigx2))/d0)
maxsizez = int((sizez + 3 * (sigz1 + sigz2))/d0)
maxsizey = int((sizey + 3 * (sigy1 + sigy2))/d0)
print maxsizex
maxsizey = maxsizey/Nprocs
c_profile = f_strain_spline3_smooth(z[0,:,0], sp, sizez)
c_profile = c_profile / c_profile.max()
u_template1 = create_u_template(c_def, misfit, R0, R0c, sizex, sigx1,
    sigx2, sizez, sigz1, sigz2, sizey, sigy1, sigy2)
print shape(u_template1)
u_template2 = create_u_template(c_def, misfit, R02, R0c, sizex, sigx1,
    sigx2, sizez, sigz1, sigz2, sizey, sigy1, sigy2)
Ndef = int(c_def*(maxsizex*maxsizez*maxsizey))
print Ndef, "defects before coalescence"

N2 = int((Ndef*f_size2)*(R0/R02)**3)
Ndef = N2 + Ndef*(1. - f_size2)
def_ratio = 1. - N2/Ndef
print Ndef*(1. - f_size2), "small defects", N2, "large defects"
print def_ratio

def defect_loop_random(Ndef, out):
    u_total = zeros((int(maxsizex), int(maxsizez), int(maxsizey)), dtype =
        'float')

```



```

#listx, listz, listy = array([0.]), array([0.]), array([0.])

n = 1
while n <= Ndef:
    x0, z0, y0 = array([d0 * int(random.uniform(0, maxsize_x))]),
        array([d0*int(random.uniform(maxsize_x*0.5, maxsize_x))]),
        array([d0*int(random.uniform(0, maxsize_y))])
    if random.uniform(0,1) < c_profile[int(z0[:]/d0)]:
        sys.stdout.write('%i ' %(Ndef-n))
        sys.stdout.flush()
        if random.uniform(0,1) <= def_ratio:
            u_total += u_template1[maxsize_x-x0[0]/d0:2*maxsize_x-x0[0]/d0:,
                maxsize_x-z0[0]/d0:2*maxsize_x-z0[0]/d0:,maxsize_y-y0[0]/d0:2*maxsize_y-y0[0]/d0:]
            n +=1
        else:
            u_total += u_template2[maxsize_x-x0[0]/d0:2*maxsize_x-x0[0]/d0:,
                maxsize_x-z0[0]/d0:2*maxsize_x-z0[0]/d0:,maxsize_y-y0[0]/d0:2*maxsize_y-y0[0]/d0:]
            n +=1
    print (str(int(Ndef)) + "cycles / processor")
    out.put(u_total)
out = mp.Queue()
jobs = []

out = mp.Queue()
jobs = []
for i in range(Nprocs):
    p = mp.Process(target = defect_loop_random, args=(Ndef, out))
    jobs.append(p)
    p.start()

res = zeros((int(maxsize_x), int(maxsize_x), int(maxsize_y), int(Nprocs)),
    dtype = 'float')
for i in range(Nprocs):
    res[:, :, :, i] = out.get()
p.join()

for i in range(Nprocs):
    if i == 0:

```



```

    final_result = res[:, :, :, i]
else:
    final_result = concatenate((final_result, res[:, :, :, i]), axis = 2)

print ""
print "Size of template (in MB)", (u_template1.nbytes +
    u_template2.nbytes)/(1000.**2)
print shape(final_result)
return final_result

#*****Displacement field calculation for spatially
    correlated defects using multiprocessing (Only long range order is
    presented here)*****

def lro_corr(alt, period, sigma, size):
    n = 0.
    corr_f = 0
    while n <= int(size/period):
        corr_f = corr_f + exp(-0.5 * ((alt - n*period)/sigma)**2)
        n += 1.
    return corr_f

def create_u_defects_lro(x, z, y, c_def, misfit, R0, R0c, sizex, sigx1, sigx2,
    sizez, sigz1, sigz2, sizey, sigy1, sigy2):
    maxsizex = int((sizex + 3 * (sigx1 + sigx2))/d0)
    maxsizez = int((sizez + 3 * (sigz1 + sigz2))/d0)
    maxsizey = int((sizey + 3 * (sigy1 + sigy2))/d0)
    maxsizey = maxsizey/Nprocs
    u_template = create_u_template(c_def, misfit, R0, R0c, sizex, sigx1, sigx2,
        sizez, sigz1, sigz2, sizey, sigy1, sigy2)
    Ndef = int(c_def*(maxsizex*maxsizez*maxsizey))
    def defect_loop_random(Ndef, out):
        u_total = zeros((int(maxsizex), int(maxsizez), int(maxsizey)), dtype =
            'float')
        listx, listz, listy = array([0.]), array([0.]), array([0.])

        n = 1
        while n <= Ndef:

```



```

x0, z0, y0 = array([d0 * int(random.uniform(0, maxsize_x))]),
              array([d0*int(random.uniform(0, maxsize_x))]),
              array([d0*int(random.uniform(0, maxsize_y))])
prob = 0.#1.-int_type

distance = sqrt((x0 - listx)**2 + (z0 - listz)**2 + (y0 - listy)**2)
listx, listz, listy = concatenate((listx, x0)), concatenate([listz,
                    z0]), concatenate([listy, y0])
prob = lro_corr(x0, int_R, sigma_corr, maxsize_x*d0) * lro_corr(z0,
                    int_R, sigma_corr, maxsize_x*d0) * lro_corr(y0, int_R, sigma_corr,
                    maxsize_y*d0)
if random.uniform(0,1) <= prob:
    sys.stdout.write('.')
    sys.stdout.flush()
    u_total += u_template[maxsize_x-x0[0]/d0:2*maxsize_x-x0[0]/d0:,
                        maxsize_z-z0[0]/d0:2*maxsize_z-z0[0]/d0:,maxsize_y-y0[0]/d0:2*maxsize_y-y0[0]/d0:
                        ]
    n +=1
    out.put(u_total)
out = mp.Queue()
jobs = []

out = mp.Queue()
jobs = []
for i in range(Nprocs):
    p = mp.Process(target = defect_loop_random, args=(Ndef, out))
    jobs.append(p)
    p.start()

res = zeros((int(maxsize_x), int(maxsize_x), int(maxsize_y), int(Nprocs)),
            dtype = 'float')
for i in range(Nprocs):
    res[:, :, :, i] = out.get()
p.join()

for i in range(Nprocs):
    if i == 0:
        final_result = res[:, :, :, i]
    else:

```



```

final_result = concatenate((final_result, res[:, :, :, i]), axis = 2)

print ""
print "Size of template (in MB)", u_template.nbytes/(1000.**2)
print shape(final_result)
return final_result

#***** substrate functions *****
def substrateE(qx, qz, x,z, sizex, sizez):
    qx = 2*pi*qx
    qz = 2*pi*qz
    sub_sizex = sizex
    sub_sizez = 60000.
    sx = sub_sizex / 3.
    sz = sub_sizez / 3.
    Ez = (-1j/(qz))*(exp(1j*qz*sub_sizez)*exp(-0.5*(qz*sz)**2) - 1.) *
        exp(1j*qz*sizez)
    Ex = (-1j/(qx))*(exp(1j*qx*sub_sizex)*exp(-0.5*(qx*sx)**2) - 1.)
    return Ez*Ex

#***** Morphological functions *****
# right side (smooth) step function
def support_2(x, thickness, sig1, sig2):
    t = x / (sqrt(2)*sig2)
    tt = (thickness + 3*sig1) / (sqrt(2)*sig2)
    z = (1 - special.erf((t-tt)))/2
    return z

# left side (smooth) step function
def support_1(x, sig1):
    t = x / (sqrt(2)*sig1)
    z = (1+special.erf((t-(3/sqrt(2)))))/2
    return z

# smooth top-hat function
def generate_1dsupport(x, thickness, sig1, sig2):
    return support_2(x, thickness, sig1, sig2)* support_1(x, sig1)

#2D top-hat function

```



```

def generate_2dsupport(x, sizex, sigx1, sigx2, z, sizez, sigz1, sigz2):
    return generate_1dsupport(x, sizex, sigx1, sigx2) *
        generate_1dsupport(z, sizez, sigz1, sigz2)

#3D top-hat function
def generate_3dsupport(x, sizex, sigx1, sigx2, z, sizez, sigz1, sigz2, y,
    sizey, sigy1, sigy2):
    ysupport = ones(sizey)
    return generate_1dsupport(x, sizex, sigx1, sigx2) * generate_1dsupport(z,
        sizez, sigz1, sigz2) * ysupport

#*****Monte Carlo evaluation of the diffracted intensity *****
def intensity_MC_gpu(u_cal, support_2d, substrate):
    intensity = zeros((shape(qx)[0], shape(qz)[1]), dtype='float')
    n = 1
    while n<= int(sizey/d0):
        print "MC step #", n
        box0[:maxsizex:, :maxsizez:] = u_cal[:, :, n-1]
        box0_gpu = gpuarray.to_gpu(box0)
        sys.stdout.write('Computing correlation function... ')
        corr_fct = generate_G_gpu(box0_gpu, d0, order)
        sys.stdout.write('Computing intensity... ')
        support_2d_gpu = zeros((int(x_range/d0), int(z_range/d0)), dtype='float')
        support_2d_gpu[:] = support_2d[:, :, 0]
        support_2d_gpu = gpuarray.to_gpu(support_2d_gpu)
        data_gpu = support_2d_gpu*corr_fct
        data_gpu = data_gpu.astype(complex64)
        plan = Plan((int(x_range/d0), int(z_range/d0)), stream = stream)
        t0 = time()
        plan.execute(data_gpu)
        ampl_temp = data_gpu.get()
        time_fft += time() - t0
        ampl_temp = abs(fft.fftshift(ampl_temp)) * normalisation +
            substrate[:, :, 0]
        int_temp = abs(ampl_temp)**2
        intensity += int_temp
        n += 1
    intensity /= int(sizey/d0)
    return intensity

```




```
*****Parameters considered*****

Nprocs = 4#mp.cpu_count()
choice_GPU = 1
scale_substrate = 0.
choice_convolution = 1 # yes = 1 ; no = 0

# Crystal size
d0 = 5.
size_x, size_z, size_y = 500.*d0, 500.*d0, 125.*d0*Nprocs #Crystal size (in
    Angstroms)

# Box size (for FFT)
sig_x1, sig_x2, sig_z1, sig_z2, sig_y1, sig_y2 = 0.001, 0.001 , 0.001 , 0.001 , 0.,
    0. #Smoothing parameters
x_range, z_range, y_range = 2048.*d0, 2048.*d0, size_y #Box size (in Angstroms)

# Material's and defect parameters
nu = 0.3 # Poisson's ratio
strain_p = array([ 0,0,0,0, 0, 0.5, 1, 0.5, 0.])
conc_p = array([ 0,0,0,0 , 0, 0.5, 1, 0.5, 0.])

misfit = 0.05 # cluster-matrix misfit
R0 = 5. # Defect size
R02 = 15. # Defect size (defect #2)
R0c = 50*R0

c_def = 0.01 # Defect concentration
f_size2 = 1. #number fraction of defects which coalesced

int_type = 1. # defect interaction type (0: repelling, 1: attraction)
int_R = 2*R0 # defect interaction range

# Experiment's parameters
order = 4. # Reflection order
wl = 1.5406
fwhm_x = 0.0003
fwhm_z = 0.0003
phi = -arcsin(wl/(2*(d0/order)))
```



```

# Computation of the array sizes and step sizes
maxsizex = (sizex + 3 * (sigx1 + sigx2))/d0
maxsizez = (sizez + 3 * (sigz1 + sigz2))/d0
maxsizey = (sizey + 3 * (sigy1 + sigy2))/d0
Ndef = int(c_def*(maxsizex*maxsizez*maxsizey))

x_step, z_step, y_step = d0, d0, d0
normalisation = (x_step*z_step)

qx_step, qz_step, qy_step = 1. / x_range, 1. / z_range, 1./y_range
qx_range, qz_range, qy_range = 1. / x_step, 1. / z_step, 1./y_step

# Generate xyz and qxyz arrays
x, z, y = arange(0, x_range, x_step), arange(0, z_range, z_step), arange(0,
    y_range, y_step)
qx, qz, qy = arange(-qx_range/2, qx_range/2, qx_step), arange(-qz_range/2,
    qz_range/2, qz_step), arange(-qy_range/2, qy_range/2, qy_step)

x, z, y = x.reshape(len(x),1, 1), z.reshape(1,len(z), 1), y.reshape(1, 1,
    len(y))
qx, qz, qy = qx.reshape(len(qx),1, 1), qz.reshape(1,len(qz), 1), qy.reshape(1,
    1, len(qy))

#*****Calling out all the functions*****
# Strain gradient (1D)
u_calg = create_u_straingradient(x, z, y, strain_p, sizex, sigx1, sigx2,
    sizez, sigz1, sigz2, sizey, sigy1, sigy2)

# Crystal generation (3D)
u_cal = create_u_defects_2_defects_grad(x, z, y, c_def, f_size2, conc_p,
    misfit, R0, R02, R0c, sizex, sigx1, sigx2, sizez, sigz1, sigz2, sizey,
    sigy1, sigy2)

# Support function (2D)
support_2d = generate_2dsupport(x, sizex, sigx1, sigx2, z, sizez, sigz1, sigz2)

#Substrate amplitude (2D)
substrate = substrateE(qx, qz, x, z, sizex, sizez)*scale_substrate

# Create array with zeros for padding

```



```

box0 = zeros((shape(x)[0], shape(z)[1]), dtype = 'float')

# Intensity computation : Main MC Loop / integration over qy
intensity = intensity_MC_gpu(u_cal, support_2d, substrate)

# Convolution with 2D resolution function
resol2D = f_2dgaussian(qx, qz, fwhmx, fwhmz, phi)
if choice_convolution == 1:
    intensity = fftconvolve(intensity, resol2D[:, :, 0], mode = 'same')

#*****All PLOTS*****
plt.figure(1)
plt.imshow(rel_SF(u_cal[:, :, (sizey/(2*d0))]).T,
            extent=(0, maxsize_x*d0, 0, maxsize_z*d0), origin='lower').set_cmap('jet')

plt.figure(2)
plt.imshow(log10(intensity).T,
            extent=(qx.min()*d0, qx.max()*d0, qz.min()*d0, qz.max()*d0), origin='lower')

plt.figure(3)
plt.subplot(3,1,1)
plt.xlim(0, size_z)
average_strain = (100*(u_cal[:, 1::, :] -
                    u_cal[:, :-1::, :]).sum(axis=0)).sum(axis=1)/(d0*(size_x/d0)*(size_y/d0))
spline_strain = 100*(u_calg[0, 1::, 0] - u_calg[0, :-1::, 0])/d0
plt.plot(z[0, :maxsize_z-1, 0], average_strain)
plt.plot(z[0, :maxsize_z-1, 0], spline_strain)

plt.subplot(3,1,2)
plt.xlim((qz[0, :]*d0).min(), (qz[0, :]*d0).max())
cut = 0.02
plt.semilogy(qz[0, :]*d0, intensity[shape(qx)[0]/2, :], qz[0, :]*d0,
             intensity[shape(qx)[0]/2 + (cut/(d0*qx_step)), :])

plt.subplot(3,1,3)
plt.xlim((qx[:, 0]*d0).min(), (qx[:, 0]*d0).max())
cut = -0.04
plt.semilogy(qx[:, 0]*d0, intensity[:, shape(qz)[1]/2], qx[:, 0]*d0,

```



```
intensity[:,shape(qz)[1]/2 + (cut/(d0*qz_step))])

plt.figure(4)
plt.imshow((u_cal[:,1::, (sizey/(2*d0))].T - u_cal[:, :-1:,
            (sizey/(2*d0))].T)/d0, extent=(0,maxsizex*d0,0,maxsizey*d0),
            origin='lower').set_cmap('jet')

plt.show()
```



General Conclusion

This investigation was conducted as part of a collaborative work of Science des Procédés Céramiques et de Traitements de Surface (SPCTS) laboratory, Limoges with the Centre de Sciences Nucléaires et de Sciences de la Matière (CSNSM), Orsay and financially supported by région Limousin. This thesis was initiated with the aim of better understanding of the behaviour of materials (mainly YSZ) under ion irradiation. The material YSZ, known for its high radiation resistance, is considered as a potential candidate to be used as an inert matrix fuel in the nuclear industry. Moreover, zirconia shares the same structure as urania, thoria and plutonia, without being radioactive, which makes the material particularly interesting and easier to handle.

YSZ was irradiated under various temperatures and in a broad ion fluence range. The interaction of ions with solids, and in this case with the YSZ target, leads to the creation of crystalline defects that induces a displacement of the Bragg peaks, a lowering of their intensity and hence the concomitant appearance of diffuse scattering in the vicinity of the peaks. In the first part of this work, the focus was put on extracting the strain and the damage depth profiles from the XRD data. The determination of these profiles is hindered by the well-known phase problem and we were able to overcome this issue by using a specific simulation based on the dynamical theory of diffraction combined with cubic B-spline functions to model the shape of the strain/disorder profiles; a generalized simulated annealing algorithm was implemented to find the best possible solution in the parameters space. The results gave an insight into the variation of strain and damage levels with the increase in temperature and fluence. Information extracted from XRD was compared with results obtained from complementary RBS/C experiments, and fully interpreted in the light of TEM analyses. Main results can be summerized as follows: increasing irradiation temperature only leads to a slight decrease of the final disorder, but significantly enhance defect clustering due to a higher mobility of the defects.

The second part of the work was focused on computing realistic two-dimensional diffuse scattering intensity distributions so as to be able to analyze the diffuse scattering from large (*e.g.* up to 10^9 unit cells) irradiated materials. A crude approach of this task would encounters serious issues related to the memory and the computing time required to handle such large crystals. Important efforts were therefore put in optimizing the algorithms and the computing tasks. We made use of heterogeneous parallel

computing wherein which the total displacement field is generated by the superposition of the displacement fields of randomly generated individual defects by using CPU multi-processing. Subsequently, the associated configuration-averaged reciprocal space maps are calculated using massively parallel computing on graphical processing units. This implementation allowed us to compute RSMs from large crystals with a speedup of up to 190 times as compared to the conventional single-processed computation on a desktop workstation. The efficiency of the method was illustrated with selected examples, particularly, ion irradiated YSZ which exhibits a complex defect structure. We were able to demonstrate that small defects (*i.e.* unit-cell sized) are very efficient in producing homogeneous elastic strain, therefore leading to the elongated streak towards the low- Q direction observed in the RSMs and $\theta - 2\theta$ scans. We further proved that defect coalescence was responsible for (i) a decrease of the apparent elastic strain, (ii) a lowering of the coherent intensity and (iii) an appearance of diffuse scattering.

It is worth mentioning that the GPU-accelerated approach to compute the RSMs is solely dependent on the crystal size, and its efficiency is independent of the complexity of the displacement field. It can hence be straightforwardly combined with any computational method that allows to compute the displacement field.

The work presented here have some very exciting future perspectives:

- Extremely fast growing GPU technology would help us analyze crystals of bigger dimensions in the near future, and may also allow us to compute three dimensional RSMs.
- Instead of computing the displacement field using our Monte Carlo algorithm, it could be obtained from atomistic simulations. This would allow to analyze even more complex situation, although the size limitation in atomistic method still is an important issue.
- Another alternative way to compute the displacement fields would be to use finite element modelling (FEM). This approach is broadly used in the case of nanostructure for instance. In our case, it would be an interesting challenge to compute the displacement field from unit-cell sized defects in large scale FEM simulations.
- The approach presented here is by no means restricted to the analysis of the irradiated materials and can be used for a broad range of systems, as long as the displacement field of the defects can be computed. For example, diffuse X-ray scattering studies of dislocations in thin films. The improvements of this method would allow quantifying the size (from point defects to large defect clusters) and density of the defects in irradiated materials, with a non-destructive, easily accessible experimental technique.



Strain and defects in irradiated materials – A study using X-ray diffraction and diffuse scattering

Ion beams are commonly used in the framework of nuclear materials in order to reproduce, in a controlled way, the different sources of irradiation that these materials are submitted to. The interaction of ions with the material induces the formation of crystalline defects along the path of these ions, associated with high strains in the irradiated region. One of the main issues of the electro-nuclear industry is the encapsulation of the long-term nuclear waste. Yttria stabilized zirconia (YSZ) is one of the materials that can be used as an inert matrix for the transmutation of actinides and therefore, understanding its behaviour under different conditions of irradiation is of utmost importance.

This thesis is divided into two distinct parts. In the first part of this work, we have used advanced X-ray diffraction (XRD) techniques in order to characterize the strain and the damage levels within the irradiated region of the crystals. The strain and the damage profiles were modelled using B-splines functions and the XRD data were simulated using the dynamical theory of diffraction combined with a generalized simulated annealing algorithm. This approach was used to study YSZ single crystals irradiated with Au^{2+} ions in a wide range of temperatures and fluences. The results were compared with the RBS/C results obtained for same samples.

The second part of the thesis is devoted to the development of a specific model for calculating the two-dimensional XRD intensity from irradiated single crystals with realistic dimensions and defect distributions. In order to achieve this goal, we have implemented high-performance parallel computing (both multi-processing and GPU-based) to accelerate the calculations. The approach was used to successfully model the reciprocal space maps of the YSZ single crystals which exhibit a complex defect structure.

Keywords : X-ray diffraction, ion irradiation, modelling, zirconia, simulations, diffuse X-ray scattering, strain, defects, parallel computing

Défauts et déformations au sein de matériaux irradiés – Étude par diffraction et diffusion des rayons X

Les faisceaux d'ions, sont communément utilisés dans le cadre de l'étude des matériaux du nucléaire dans le but de reproduire, dans une certaine mesure, les différentes sources d'irradiations auxquelles sont soumis ces matériaux. L'interaction des ions avec la matière induit la formation de défauts cristallins le long du trajet de ces ions, associée à d'importantes déformations au sein de la zone irradiée. L'un des principaux enjeux de l'industrie électro-nucléaire consiste en l'encapsulation, à long terme, des déchets nucléaires. La zircone yttrée (YSZ) est un des matériaux qui pourrait être utilisé comme matrice inerte pour la transmutation des actinides. Par conséquent, la compréhension du comportement d'YSZ sous différentes conditions d'irradiations est d'une importance capitale.

Cette thèse est décomposée en deux parties distinctes. Dans la première partie de ce travail, nous avons utilisé plusieurs techniques avancées de diffraction des rayons X (DRX) dans le but de caractériser les défauts et déformations au sein de la zone irradiée des cristaux étudiés. Les profils de déformations et de défauts ont été modélisés par des fonctions B-splines cubiques et les données DRX ont été simulées en utilisant la théorie dynamique de la diffraction couplée à un algorithme de recuit simulé généralisé. Cette démarche a été appliquée au cas des monocristaux d'YSZ irradiés par des ions Au^{2+} dans une large gamme de températures et de fluences. Les résultats ont été comparés avec ceux de la spectroscopie de rétrodiffusion de Rutherford en mode canalisé (RBS/C) obtenus pour les mêmes échantillons.

La deuxième partie est consacrée au développement d'un modèle spécifique pour calculer la distribution bidimensionnelle d'intensité diffractée par des monocristaux irradiés de grandes dimensions et présentant des distributions de défauts réalistes. Pour atteindre cet objectif, nous avons mis en œuvre une approche de calcul parallèle haute performance (basée à la fois sur l'utilisation de processeurs multi-cœurs et de processeurs graphiques) afin de réduire les durées de calcul. Cette approche a été utilisée pour modéliser les cartographies X de l'espace réciproque de monocristaux d'YSZ présentant des défauts de structure complexe.

Mots-clés : Diffraction des rayons X, irradiation aux ions, modélisation, zircone, simulation, diffusion diffuse des rayons X, déformation, défaut, calcul parallèle

